Title
Early Mars Geodynamics: Giant Impacts, Super-plumes, and Vast Oceans

Author
Citron, Robert I

Publication Date
2019

Peer reviewed|Thesis/dissertation

Early Mars Geodynamics: Giant Impacts, Super-plumes, and Vast Oceans

by

Robert I. Citron

A dissertation submitted in partial satisfaction of the

requirements for the degree of

Doctor of Philosophy

in

Earth and Planetary Science

in the

Graduate Division

of the

University of California, Berkeley

Committee in charge:

Professor Michael Manga, Chair
Professor Imke de Pater
Professor Eliot Quataert

Summer 2019

Early Mars Geodynamics: Giant Impacts, Super-plumes, and Vast Oceans

Abstract

Early Mars Geodynamics: Giant Impacts, Super-plumes, and Vast Oceans

by

Robert I. Citron

Doctor of Philosophy in Earth and Planetary Science

University of California, Berkeley

Professor Michael Manga, Chair

The ancient crust of Mars contains a remarkable record of the planet's early history. With 45% of the martian crust dated to the Noachian (>3.7 Ga) and another 30% of the crust dated to the Hesperian (>3 Ga), Mars provides a unique opportunity to examine processes that can influence the early evolution of terrestrial planets. Observations of Mars' surface motivate hypotheses as to what processes controlled the planet's early evolution and how the surface developed into its present form. Key features to explain for early Mars are the formation of the crustal dichotomy, the massive Tharsis volcanic province, and the prevalence of features indicating widespread early water. Hypotheses for the formation of these features can be tested using geodynamic models. For the origin of the crustal dichotomy, both endogenic (mantle convection) and exogenic (giant impact) mechanisms have been proposed. We examine if a hybrid model in which a giant impact can influence the global pattern of mantle convection. We find that a superplume can form on Mars following an early giant impact, and examine the subsequent superplume dynamics and migration in relation to the formation of Tharsis and remanent crustal magnetism. For a purely giant impact origin of the crustal dichotomy, we find that the crustal structure of the dichotomy is difficult to reproduce with high-resolution impact models. We also examine evidence for early oceans on Mars, finding that deviations in proposed paleoshoreline elevations from present-day equipotential surfaces can be explained by deformation due to the emplacement of Tharsis and other surface loads. Our results suggest that Mars paleoshorelines follow paleo-equipotentials, supporting the ocean hypothesis. Overall, our results provide insight into the early processes that may have occurred on Mars, and their effect on the subsequent evolution of the planet.

For my family

Contents

List of Figures

List of Tables

Acknowledgments

My path to completing a PhD has been a meandering one, and I would like to thank the many people that have supported and influenced me on my academic journey.

First and foremost, I would like to thank my thesis advisor Michael Manga for his mentorship and support during my time at Berkeley. His office door has always been open and he has provided a great deal of feedback, advice, insight, and understanding. In particular, Michael has given invaluable guidance on how to approach scientific problems and succeed in science. Michael has allowed me the space to pursue my own research interests, and my productivity has only ever been limited by my own willpower. I am very grateful that Michael allowed me a second chance at graduate school at UC Berkeley.

I also would like to thank the rest of my thesis committee, Imke de Pater and Eliot Quataert, for their patience and feeback.

I have benefited from many research advisors and mentors over the years. In particular, I would like to thank Amy Barr and Shijie Zhong, who advised me during my early graduate studies at CU Boulder, and Oded Aharonson, who gave me the opportunity to again pursue planetary science research after some time off. I would also like to thank Chris McKay and Jennifer Heldmann, who shaped my interest in planetary science as an intern at NASA Ames, and Thanasis Economou, my undergraduate research advisor. I would also like to thank Peter Jenniskens for his continued mentorship in meteorite hunting. I would also like to thank Hidenori Gendai, Shigeru Ida, Hagai Perets, and Eh Tan, who welcomed me into their labs abroad.

I would also like to thank several other collaborators: Doug Hemingway, Raluca Rufu, Ben Black, James Keane, Stuart Robbins, Raymond Jeanloz, and Avi Ravid. I would also like to thank Rob Lillis and Mark Richards, who were on my qualifying exam committee. I would also like to thank Edwin Kite for helpful discussions.

I benefited greatly from participating in the CIDER program, and would like to thank the fellow members of the SHEEP group project for their friendship and collaboration: Diogo Lourenço, Fred Wilson, Antoniette Grima, and Scott Wipperfurth. I would also like to thank Max Rudolph and Sanne Cottaar for providing generous time and advice on that project.

I would also like to thank my fellow EPS students for being a great resource and source of support. In particular I would like to thank Stephen Breen and Tushar Mittal for their companionship and generosity of ideas. I would also like to thank Tom Smart, Noah Randolph-Flagg, Kristen Fauria, Alex Bryk, Hannah Bourne, Matt Diamond, Nate Lindsey, Mike Antonelli, and Nick Knezek, among many others.

Finally, I would like to thank my family for their endless support.

Chapter 1

Overview

The ancient surface of Mars reveals a remarkable history of a dynamic planet influenced by widespread volcanism, large impacts, widespread fluvial activity, and other processes (Figure 1.1). The geologic history of Mars is typically divided into three epochs: the Noachian (>3.6 Ga), Hesperian (3−3.6 Ga), and Amazonian (3 Ga − present). With 45% of Mars' surface dated to the Noachian and 30% dated to the Hesperian, the martian crust is ancient compared to that of Earth and Venus, where plate tectonics and global resurfacing, respectively, have erased the early geologic record. Mars thus provides a unique opportunity to examine a diverse set of processes that influence the early evolution of terrestrial planets. Additionally, as our most accessible neighbor, Mars is simply a place to explore. Observations of its geology motivate hypothesis that can be tested with further studies (*e.g.*, theory, numerical models, experiments), unraveling the secrets of Mars' past and how the planet has evolved over time.

Mars' geologic record displays a range of processes that influenced the early evolution of the planet (Figure 1.2). In the pre-Noachian, the earliest martian crust formed relatively soon after accretion. The earliest crust is not readily observable at the surface, where the oldest model surface ages are ∼4.1 Ga, the early Noachian (Frey, 2006b). Perhaps the oldest feature observable on Mars is the stark difference in crustal thickness and topography between the northern and southern hemispheres, known as the martian crustal dichotomy. The origin of the crustal dichotomy is subject of ongoing debate, but could been generated by an internal process such as mantle convection (over 100s of Myr) or an early giant impact ∼4.5 Ga. Early Mars also generated a magnetic field, as evidenced by remanent crustal magnetization. Lack of magnetization in giant impact basins and more recent volcanic centers indicates the martian dynamo died about 4−4.1 Ga, around the time of the formation of the Utopia and Hellas impact basins in the early Noachian (Lillis et al., 2013a).

Noachian Mars contains the large impact basins of Utopia, Hellas, Argyre, and Isidis. Widespread volcanism which likely occurred in the pre-Noachian, continued into the Noachian. The large volcanic province Tharsis began forming in the early-mid Noachian, likely the result of a large mantle plume. Emplacement of the Tharsis load likely induced ∼ 20° of true polar wander (TPW), the solid-body rotation of the planet with respect to its spin

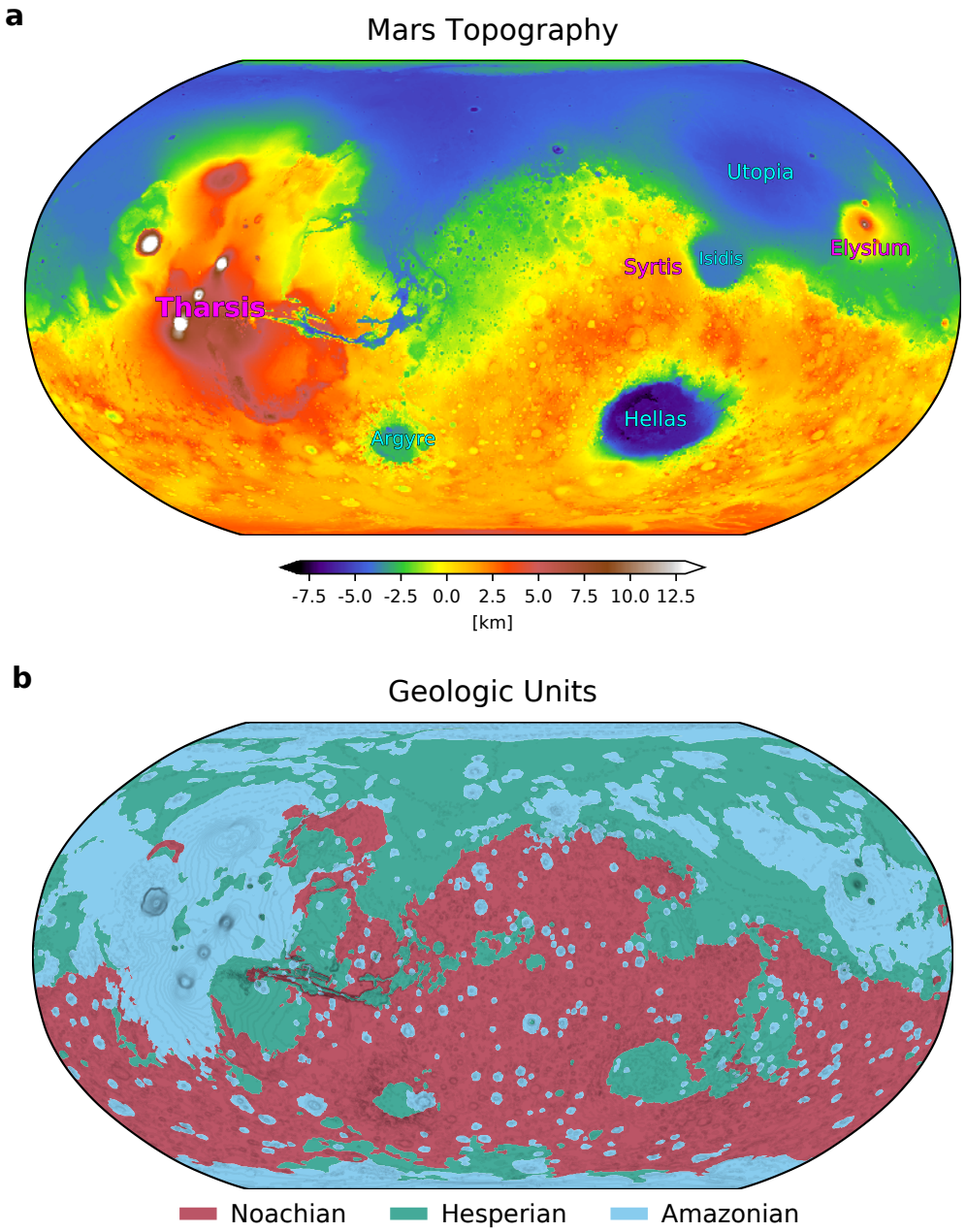

Figure 1.1: Mars topography and geologic surface units. (a) Mars topography (Smith et al., 2003) with large volcanic centers and impact basins labeled in magenta and cyan, respectively. The northern lowlands are in blue and the southern highlands are in orange/red. (b) Distribution of geologic epoch units from Tanaka et al. (2014). Noachian terrain is >3.6 Ga, Hesperian is 3−3.6 Ga, and Amazonian is 3 Ga − present.

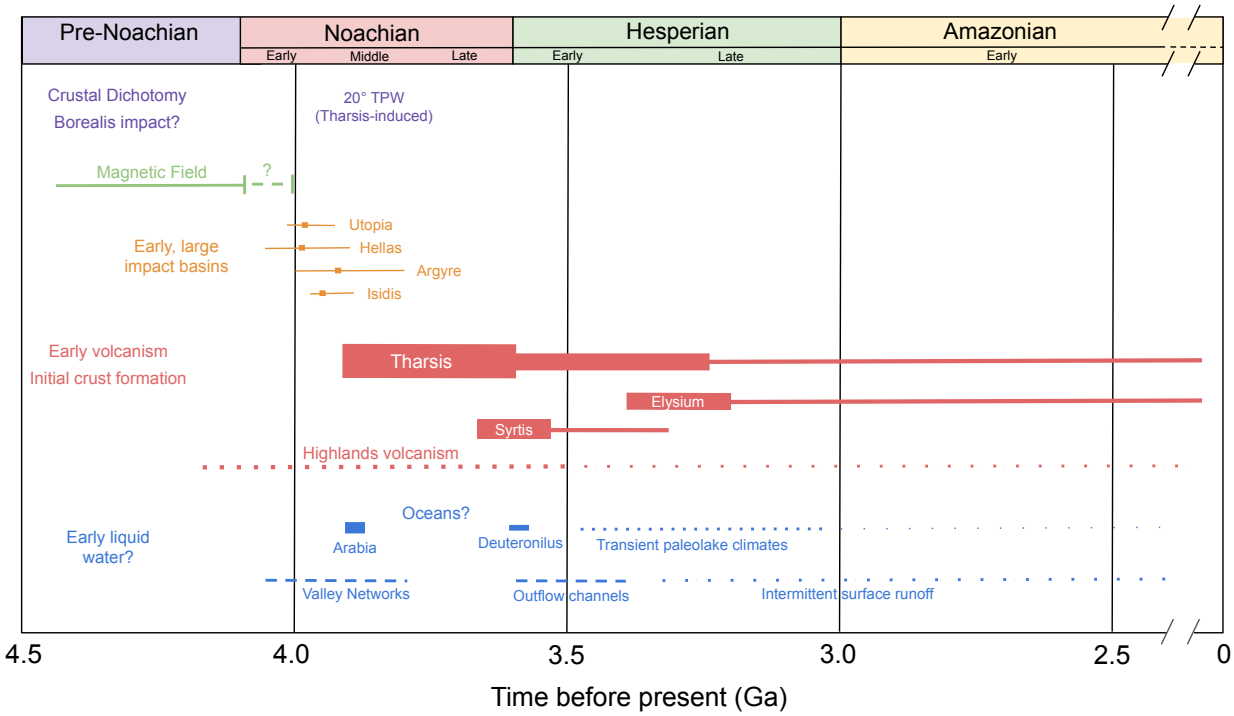

Figure 1.2: Proposed chronology of early Mars. Epochs are based on chronology of Hartmann and Neukum (2001) and Hartmann (2005), with estimates of surface ages from crater counting statistics (boundaries between the Noachian, Hesperian and Amazonian epochs are estimates and vary in the literature). Timing of Tharsis volcanism is based on Bouley et al. (2018), and timing of Elysium, Syrtis and other volcanism is based on Platz and Michael (2011) and Werner (2009). Impact basin ages from Robbins et al. (2013). Timing of magnetic field from Lillis et al. (2013a). Timing of fluvial activity is from various studies of Mars hydrology (Fairén et al., 2003; Ivanov et al., 2017; Kite et al., 2017, 2019; Kite, 2019).

axis (Matsuyama and Manga, 2010). The initiation of Tharsis volcanism may have occurred concurrently or shortly following the formation of the Valley Networks (an extensive network of ancient rivers) and hypothetical early martian oceans.

Widespread volcanism and fluvial activity continued into the Hesperian. Lack of plate tectonics allowed mantle plumes to remain relatively stationary relative to the surface, resulting in the construction of the extensive Tharsis volcanic province, in addition to other major long-lived volcanic centers such as Elysium and Syrtis. Periods of intense volcanic activity and surface heat flux may have breached the cryosphere, resulting in large outflow channels that could have inundated the northern plains with water, potentially coincident with the hypothetical Deuteronilus ocean at the Noachian/Hesperian boundary. Fluvial activity continued into the late Hesperian and Amazonian with periods of intermittent paleolakes, surface runoff, and groundwater upwelling.

The relatively quiet and dry Amazonian period began ∼3 Ga and continues to present. Although large scale geodynamic processes mostly tapered off before and during the Amazonian, dynamic processes such as shifting polar caps, glaciation, recurring slope linea, and fresh impact craters record a recently and still evolving martian environment.

Our understanding of Mars comes from an array of planetary missions (orbiters, rovers, and landers) that provide a wealth of data on the planet's surface and interior. Spacecraft observations motivate hypotheses regarding what processes produced (and what are) the various geologic features we observe across the planet. These hypotheses can be tested with a range of methods including theory, numerical modeling, laboratory experiments, and further observations. In this dissertation, we focus on geodynamic modeling, which allows us to explore a range of planetary scale geophysical processes that might explain geological observations. Planetary geophysical processes often operate at scales not readily explored in the laboratory. Numerical simulations of processes such as mantle convection or a giant impact allows for a more feasible examination of a wide range of scales and geometries.

While there are many processes to explore with respect to early Mars evolution, here we focus on the origin of the martian crustal dichotomy, the origin of the Tharsis superplume, and geodynamic constraints on evidence for early oceans. The crustal dichotomy and Tharsis dominate the surface, gravity, and crustal structure of Mars. Their formation greatly influenced subsequent Mars geodynamic and geologic evolution, and their origin is a fundamental problem in early Mars geodynamics. The crustal dichotomy in particular is the oldest observable feature on the planet, and while many theories have been proposed regarding its formation, none explain all of the observations related to its formation and its influence on the subsequent evolution of the planet. Additionally, we examine the geodynamic evidence for early martian oceans. While the existence of early martian oceans is hypothetical and a matter of much debate, the presence of oceans is of great importance to our understanding of Mars' early geology, hydrologic cycle, and climate. The existence of Mars oceans is also has potential implications regarding the prospect of early Mars habitability. Overall, the fundamental reason for focusing on the dichotomy, Tharsis, and oceans is that there are many unanswered questions regarding their formation and evolution that have widespread implications for early Mars geology, geophysics, and climate, and hypotheses regarding these features can be readily examined with geodynamic models.

The Mars crustal dichotomy and Tharsis formation are the focus of Chapters 2, 3, and 4, and Mars oceans are studied in Chapter 5. In Chapter 2, we examine a hybrid model of dichotomy formation in which there is a causal relation between an early giant impact and subsequent superplume formation, which both contribute to the formation of the crustal dichotomy. In Chapter 3 we expand on this model and examine the evolution of a superplume on Mars, its relation to remanent crustal magnetism and the formation of Tharsis on the dichotomy boundary. In Chapter 4 we examine a giant impact origin of the crustal dichotomy, and if more advanced numerical models can better reproduce the crustal dichotomy. In Chapter 5 we examine how planetary-scale deformation due to Tharsis and other surface loads could have modified past equipotential surfaces. Deformation of paleo-equipotentials is used to constrain the evidence of paleoshorelines and test the Mars ocean hypothesis.

Chapter 2

The Mars Crustal Dichotomy: A Hybrid Origin

This chapter is adapted with minor changes from:

> Citron, R. I., Manga, M., and Tan, E. (2018), "A hybrid origin of the Martian crustal dichotomy: Degree-1 convection antipodal to a giant impact." *Earth and Planetary Science Letters*, 491, 58-66.

2.1 Summary

The Martian crustal dichotomy is the stark ∼5 km difference in surface elevation and ∼26 km difference in crustal thickness between the northern lowlands and southern highlands that originated within 100s of Myr of Mars' formation. The origin of the dichotomy has broad implications for the geodynamic history of Mars, but purely exogenic or endogenic theories so far cannot explain all of the large scale geophysical observations associated with dichotomy formation. A giant impact can produce the shape and slope of the dichotomy boundary, but struggles to explain Mars' remnant crustal magnetic signatures and the ultimate formation of Tharsis. Degree-1 mantle convection can relate the crustal dichotomy to the formation of Tharsis, but does not explain the elliptical dichotomy shape and must be initiated by a large pre-existing viscosity jump in the mantle. We propose a hybrid model of dichotomy formation in which a giant impact induces degree-1 convection with an upwelling antipodal to the impact site. In this scenario, a giant impact in the northern hemisphere excavates crust, creating an initial difference in crustal thickness and possibly composition between the two hemispheres. Over 10s to 100s of Myr, the dominant upwelling(s) would migrate to be under the thicker, insulating crust in the southern hemisphere, generating melt that further thickens the southern crust. We examine this process using 3-D mantle convection simulations, and find that a hemispherical difference in crustal thickness and composition caused by a giant impact can induce degree-1 convection with the upwelling(s) antipodal to the impact site in <100 Myr.

2.2 Introduction

2.2.1 Constraints on dichotomy formation

One of the oldest observable features on Mars is the crustal dichotomy, an approximately hemispheric difference of ∼5 km in surface elevation and ∼26 km in crustal thickness between the northern lowlands (Borealis basin) and southern highlands (Figure 2.1) (*e.g.,* Smith et al., 1999; Zuber, 2001; Neumann et al., 2004; Watters et al., 2007). The formation of the dichotomy is generally attributed to either an exogenic event such as a giant impact (*e.g.,* Wilhelms and Squyres, 1984; Marinova et al., 2008; Nimmo et al., 2008), or an endogenic process such as mantle convection (*e.g.,* Zhong and Zuber, 2001; Ke and Solomatov, 2006; Keller and Tackley, 2009; Roberts and Zhong, 2006; Šrámek and Zhong, 2010). There are several important constraints or potential constraints on the formation mechanism, including the timing of dichotomy formation, boundary shape, magnitude of variation in crustal thickness, distribution/strength of remnant crustal magnetism, and formation of Tharsis on the dichotomy boundary.

Crater retention ages for buried and visible craters suggest that the dichotomy likely originated within 100s of Myrs of Mars' formation (*e.g.,* Watters et al., 2007; Frey, 2006a,b; Nimmo, 2005), and geochemical arguments also suggest an early formation time ∼4.5 Ga (Bottke and Andrews-Hanna, 2017; Brasser and Mojzsis, 2017). Relatively early formation of the dichotomy is consistent with a giant impact during the late stages of planetary accretion (Brasser and Mojzsis, 2017), but limits endogenic theories because it constrains the timescale for mantle convection to evolve to a degree-1 pattern. Solid-solid phase changes in the mantle have been successful at producing degree-1 convection, but only on Gyr timescales

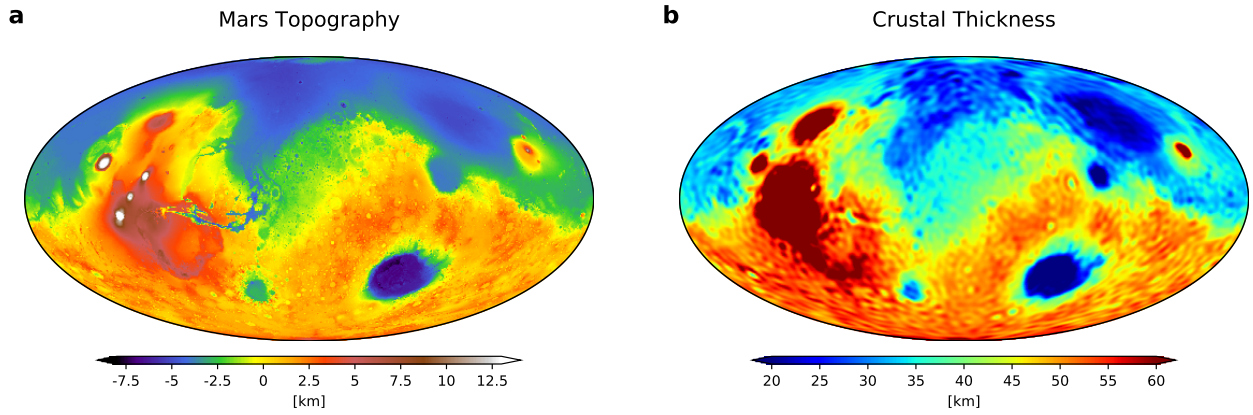

Figure 2.1: Mars topography and crustal thickness. (a) Topography is from gridded MOLA data (Smith et al., 2003) and (b) inferred crustal thickness is from Genova et al. (2016). The crustal dichotomy is the difference in elevation and crustal thickness between the northern lowlands and southern highlands. The Tharsis rise is the red region of higher elevation and thicker crust in the western hemisphere.

and require a constant or weakly temperature dependent viscosity (Harder, 2000; Roberts and Zhong, 2006). Degree-1 convection can arise on shorter timescales (100s of Myr) if Mars had a temperature dependent, layered viscosity with a factor of 25 increase in the mid-mantle (Roberts and Zhong, 2006). It is unclear what process would cause such a large viscosity jump in the mantle, but it could be the result of a solid-solid phase transition, compositional variation from an early magma ocean, or a transition from diffusion to dislocation creep (*e.g.,* Roberts and Zhong, 2006; Zhong and Zuber, 2001). Compositional layering due to magma ocean solidification has been proposed as a mechanism to generate asymmetrical overturn on timescales <10 Myr (*e.g.,* Elkins-Tanton et al., 2005, 2003), however, more recent work has shown that degree-1 structures are unlikely to result from mantle overturn on Mars (Scheinberg et al., 2014).

The elliptical shape of the dichotomy boundary has been used as evidence for a giant impact because Borealis-scale impacts produce elliptical basins due to the effects of planet curvature (Andrews-Hanna et al., 2008) and the scale of the impact (Collins et al., 2011). An elliptical basin could also be the result of an impact megadome, which occurs when an impact is large enough to cause widespread crust production and magmatism in the impacted hemisphere, a scenario that could potentially result in a Borealis-like depression in the hemisphere opposite the megadome (*e.g.,* Reese et al., 2011, 2010; Golabek et al., 2011, 2018). An elliptical boundary shape would not be an expected result of degree-1 convection, but migration of a single upwelling and the resulting crust production could result in asymmetries in the dichotomy boundary (Šrámek and Zhong, 2012). An elliptical dichotomy shape could result from one-ridge convection, where the upwelling planform is a single ridge spread over half of Mars (Keller and Tackley, 2009). Furthermore, although the dichotomy boundary appears elliptical, the pre-Tharsis boundary computed by removing Tharsis depends on the elastic plate thickness (Andrews-Hanna et al., 2008) and contributions of lateral or temporal elastic thickness variations are unexplored (Šrámek and Zhong, 2010).

The extent of crustal thickness variation between the northern and southern hemispheres of Mars, as inferred from gravity and topography data (*e.g.,* Neumann et al., 2004; Wieczorek, 2015), is possible with both exogenic and endogenic dichotomy formation mechanisms. Coupling of melt/crust production with mantle convection models can produce crust in one hemisphere of similar thickness to the present-day highlands (Šrámek and Zhong, 2012; Keller and Tackley, 2009), however, such crust production depends on the vigor of convection and not all plumes produce melt (Sekhar and King, 2014). The required crustal thickness variation can also be produced by magmatism resulting from an impact megadome (Golabek et al., 2011). For a Borealis-scale impact, numerical impact simulations show that the resulting crustal thickness variation is generally consistent with present observations (*e.g.,* Marinova et al., 2008; Nimmo et al., 2008). An additional effect of excavating crust in the northern hemisphere via a giant impact is the formation of a circum-Mars debris disk that could explain the formation of the Martian moons Phobos and Deimos (*e.g.,* Craddock, 2011; Citron et al., 2015; Rosenblatt et al., 2016). The sharp dichotomy boundary expected from an impact could also induce edge driven convection, possibly explaining the buried mass anomalies on the eastern dichotomy boundary (Kiefer, 2005).

Another constraint on dichotomy formation is the remnant crustal magnetic signatures that are observed over the entire planet, indicating another global process active early in Martian history (Acuna et al., 1999). The remnant magnetic signatures are significantly stronger in the southern hemisphere, and also contain a unique pattern of lineations of alternating polarity (Connerney et al., 2005). The emplacement of the magnetic signatures most likely occurred prior to the cessation of the Martian dynamo ∼4.1 Ga (Lillis et al., 2013a), although it is uncertain if the magnetic signatures were emplaced before, during, or after dichotomy formation. The magnetic signatures must post-date a giant impact because a Borealis-scale impact could have completely erased magnetic signatures in the northern lowlands (Lillis et al., 2013b), and the thick ejecta blanket could have demagnetized the entire southern crust as well (Citron and Zhong, 2012). Even if an impact occurred in the presence of a strong magnetic field, the pattern of magnetic lineations of alternating polarity is difficult to reconcile with Borealis-scale impact/ejecta generated melt or magmatisim associated with an impact megadome (*e.g.,* Golabek et al., 2018), which would have cooled on a short timescale in the vertical direction. The alternating polarity of the lineations could be explained by crust production radiating from a single large plume in a reversing magnetic field, which might explain why the geometry of the lineations roughly corresponds to concentric circles centered around a single pole that is <300 km from the centroid of the thickened southern crust (Citron and Zhong, 2012). However, the melting history is likely more complex than the simple model of Citron and Zhong (2012), and could involve multiple migrating plumes and more complex melt extraction and crust evolution. Furthermore, the pattern of lineations observed from orbit does not necessarily represent the distribution of magnetized material at depth. Still, emplacement of the magnetic signatures during thickening of the southern crust could at least explain the higher strength and concentration of remnant magnetic signatures in the southern hemisphere, particularly if degree-1 convection promotes the development of a hemispherical dynamo (Stanley et al., 2008).

The formation of Tharsis on the dichotomy boundary also favors the endogenic theory of dichotomy formation. If degree-1 convection sufficiently thickens the southern crust, it would create a layer of highly viscous melt residue under the thickened crust. This lateral variation in viscosity could cause differential rotation of the lithosphere or migration of the degree-1 upwelling, until the plume reaches the dichotomy boundary and creates Tharsis (Zhong, 2009; Šrámek and Zhong, 2010, 2012). Plume migration from the south pole to Tharsis' location is supported by observations of volcanic resurfacing, demagnetization, and increased crustal thickness along that path (Hynek et al., 2011; Cheung and King, 2014), and is consistent with the creation of Tharsis within a few hundred Myrs of dichotomy formation (Phillips et al., 2001; Solomon et al., 2005; Nimmo, 2005).

2.2.2 A hybrid origin

Neither a purely exogenic nor endogenic model can easily or obviously explain all geophysical observations related to dichotomy formation. Because of this, we examine a hybrid model in which a giant impact forms the Borealis basin, producing an initial nearly hemispherical

difference in crustal thickness and composition that induces degree-1 convection with the upwelling centered under the thicker, enriched (in radiogenic elements) crust opposite the impact site (Fig. 2.2). Although initially an upwelling should develop under the impact site, such an upwelling should dissipate relatively quickly (Roberts et al., 2009; Roberts and Arkani-Hamed, 2012; Ghods and Arkani-Hamed, 2011; Roberts and Arkani-Hamed, 2017), allowing for the composition and structure of the crust/lithosphere to control the convection pattern over longer timescales (100s of Myr). We expect the northern and southern post-impact crusts to differ in composition, specifically the concentration of radiogenic heating elements, because of the depletion of such elements from the mantle over time. During Mars' initial crust formation, radiogenic elements would be partitioned into the crust, creating an ancient crust enriched in radiogenic elements and depleting the mantle of the same elements. The giant impact would strip the northern hemisphere of its original, enriched crust, and the new crust in the northern hemisphere would be derived from an already depleted mantle, resulting in a new northern crust that is depleted in radiogenic elements relative to the southern crust. The compositional difference between the newer depleted crust in the northern hemisphere and the ancient crust in the southern hemisphere could persist for billions of years (Ruedas and Breuer, 2017), and may explain hemispheric differences in martian lithosphere thickness (Thiriet et al., 2018). On early Mars, the thicker, enriched crust in the hemisphere opposite the impact should have an insulating effect that increases the mantle temperature and promotes hot spot and plume formation under the thicker, enriched southern crust (van Thienen et al., 2006), similar to the effect of supercontinents on Earth (*e.g.,* Gurnis, 1988;

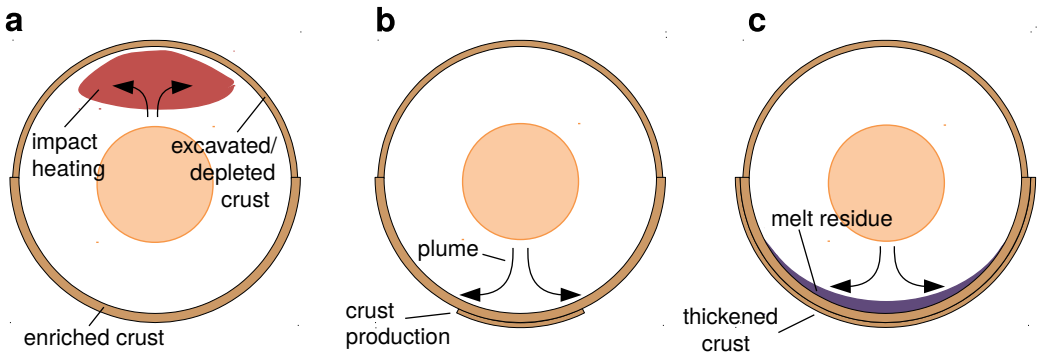

Figure 2.2: Proposed hybrid model of dichotomy formation. (a) An impact causes excavation, heating, and a transient upwelling in the northern hemisphere. While a new northern crust would form relatively rapidly, it would form from an already depleted mantle (depleted from forming the original crust) and thus be depleted in radiogenic elements relative to the older, more enriched southern crust. (b) The insulating effect of the thicker, enriched southern crust results in degree-1 convection with a large upwelling in the southern hemisphere. (c) Melt generation from the upwelling(s) further thickens the crust in the hemisphere opposite the impact, and resulting melt residue could explain subsequent migration of the plume/lithosphere and the formation of Tharsis at the dichotomy boundary (Zhong, 2009).

Lowman and Jarvis, 1995; Lenardic et al., 2005). In this scenario, the initial crustal thickness variation caused by the Borealis impact is not as extensive as currently observed, but is amplified by the additional melt produced by the superplume that naturally develops in the southern hemisphere due to the insulating southern crust. New crust production in the southern hemisphere could explain the formation of the remnant crustal magnetic signatures (provided that the crust is produced before the end of the dynamo), and could also result in a layer of highly viscous melt residue. The melt residue under the southern crust could induce plume migration and/or differential lithosphere rotation resulting in the formation of Tharsis on the dichotomy boundary (Zhong, 2009; Šrámek and Zhong, 2010).

Degree-1 convection has previously been shown to migrate so that the upwelling becomes centered under an insulating cap (Šrámek and Zhong, 2010), however, these simulations relied on a large viscosity jump (*e.g.,* Roberts and Zhong, 2006) to initiate degree-1 convection without the presence of an insulating cap. Because a possible mechanism for a large mid-mantle viscosity jump, a transition from ringwoodite to a basal perovskite/ferropericlase layer, likely occurs in the deepest mantle or not at all on Mars (*e.g.,* Ruedas et al., 2013b), crustal thickness and composition may be more important factors in Martian mantle dynamics. Crustal structure has been shown to have an important effect on mantle convection on present-day Mars (Plesa et al., 2016), and experiments and numerical simulations suggest that upwellings could have focused under an insulating lid on early Mars (Wenzel et al., 2004; van Thienen et al., 2006). In this study, we examine if degree-1 convection forms on Mars as a natural response to an impact-generated insulating cap with no viscosity jump in the mid-mantle, and with the upwelling centered in the hemisphere opposite the impact site. We conduct numerical simulations of mantle convection for a range of initial crustal thickness variations and insulating effects.

2.3 Methods

Mantle convection simulations are conducted using CitcomS (Zhong et al., 2000; Tan et al., 2006), a finite element mantle convection code widely used in studies of Earth and other planetary bodies. The Martian mantle is represented by a spherical shell heated from below and within using the Boussinesq approximation, given by the following non-dimensional governing equations:

$$\nabla \cdot \mathbf{u} = 0 \tag{2.1}$$

$$-\nabla P + \nabla \cdot [\eta(\nabla \mathbf{u} + \nabla^T \mathbf{u})] + \mathrm{Ra} T \mathbf{e_r} = 0 \tag{2.2}$$

$$\frac{\partial T}{\partial t} + \mathbf{u} \cdot \nabla T = \nabla \cdot (\kappa(r) \nabla T) + H_{int} - H_L \tag{2.3}$$

where $\mathbf{u}$, P, T, and η are the velocity vector, pressure, temperature, and viscosity, respectively, and $\kappa(r)$ is a non-dimensional prefactor for the thermal diffusivity to account for a

reduced thermal conductivity in the crust. The latent heating rate from magma melting is H_L. The Rayleigh number Ra is defined as

$$Ra = \frac{\rho_m g \alpha_0 \Delta T R_p^3}{\kappa_0 \eta_0} \tag{2.4}$$

where R_p is the planetary radius, g is gravitational acceleration, ΔT is the super-adiabatic temperature difference, and ρ_m, α_0, κ_0, and η_0 are the reference values for mantle density, thermal expansivity, thermal diffusivity, and viscosity, respectively. The reference viscosity corresponds to the value at the base of the mantle. The internal heating number H_{int} is defined as

$$H_{int} = \frac{Q R_p^2}{\rho_m C_p \Delta T \kappa_0} \tag{2.5}$$

where C_p is the specific heat at constant pressure and Q is a variable volumetric heating rate based on Wanke and Dreibus (1994) that decays with time (starting at 50 Myr after solar system formation). We allow for cooling of the core based on the heat flux from the bottom boundary (*e.g.,* Plesa et al., 2016, and references therein):

$$C_c \rho_c V_c \frac{dT_{CMB}}{dt} = -q_c A_c \tag{2.6}$$

where we assume an adiabatic core with constant specific heat capacity C_c=800 J K^{-1} kg^{-1} and density ρ_c=7200 kg m^{-3}, q_c is the heat flux from the core, and V_c and A_c are the volume and surface area of the core, respectively.

For simplicity, we use the Boussinesq approximation, neglecting adiabatic heating/cooling and instead adding an adiabatic gradient to the simulation temperature before computing melting (Li et al., 2016). The effect of using the Boussinesq approximation instead of the extended Boussinesq approximation should be small due to the low dissipation number for Mars (Plesa and Breuer, 2014). Although our simplification could affect the amount of melting, it should not affect the convective pattern and significantly alter our main conclusions.

The Martian mantle may deform via either diffusion or dislocation creep. We use a non-dimensional pressure- and temperature-dependent viscosity similar to Roberts and Zhong (2006) but with no viscosity layering prefactor:

$$\eta = \exp\left(\frac{E' + V'(1-r)}{T + T_s} + \frac{E' + V'(1-R_c)}{1 + T_s}\right) \tag{2.7}$$

where r is the non-dimensional radius, and the non-dimensional parameters E', V', and T_s, and non-dimensional temperature T, are given by

$$E' = \frac{E_a}{R\Delta T}, \quad V' = \frac{\rho_m g R_p V_a}{R\Delta T}, \quad T_s = \frac{T_{surf}}{\Delta T}, \quad T = \frac{T_d}{\Delta T} + T_s \tag{2.8}$$

where E_a, V_a, R, and T_{surf} are the activation energy, activation volume, gas constant, and surface temperature, respectively, and T_d is the dimensional temperature.

The simulation is composed of 12 spherical caps, each with a resolution of 64 x 64 x 64 elements, with an increasing radial resolution near the boundary layers. We use isothermal, free-slip boundary conditions on the top and bottom boundaries. We use the parameters listed in Table 2.1 and an initial non-dimensional mantle temperature T_m=0.75, with top/bottom thermal boundary layers determined by a conductive half-space cooling/heating model (error function) with a time of 50 Myr. We start the simulation with random perturbations of 0.01 to the non-dimensional temperature in the mid-mantle.

We use an activation energy of 157 kJ/mol for dislocation creep, but also run a simulation with an activation energy of 300 kJ/mol for diffusion creep, which may be more appropriate for Mars (*e.g.,* Grott and Breuer, 2009). For the higher activation energy run, we increase the Rayleigh number in order to obtain a similar viscosity profile (Figure 2.3). We also run two simulations with a lower activation volume and higher Rayleigh number (Table 2.4).

We use a Rayleigh number of 10^8 which, given the parameters listed in Table 2.1, initial temperature profile, and temperature- and pressure-dependent viscosity, results in an average initial mantle viscosity of $\sim 1.58 \times 10^{21}$ Pa·s (Fig. 2.3). Experiments have suggested viscosity variations of ∼100–1000 across the sublithospheric mantle on Earth (Karato and Wu, 1993; Karato and Jung, 2003). The Martian mantle, presumably also primarily olivine, contains ∼17 wt% FeO (Dreibus and Wanke, 1985) compared to ∼8 wt% in the Earth's upper mantle (McDonough and Sun, 1995), which could reduce the viscosity of Mars' mantle by a factor of 10 relative to Earth's mantle (Zhao et al., 2009). Increased iron content could also result in a higher activation volume for the Martian mantle, leading to increased viscosity variations with depth (Raterron et al., 2017).

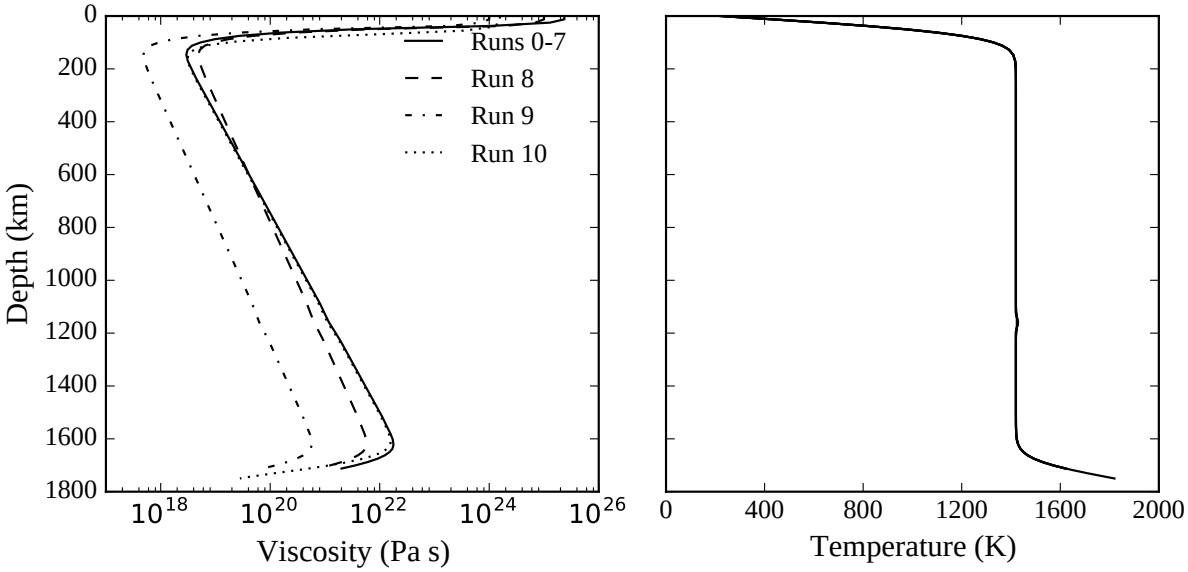

Figure 2.3: Initial viscosity and temperature profiles with depth.

Table 2.1: Model Parameters

Parameter	Symbol	Value
Planetary radius	R_p	3400 km
Core radius	R_c	1650 km
Gravitational acceleration	g	3.73 m s^{-2}
Mantle density	ρ_m	3400 kg m^{-3}
Specific heat	C_p	1200 J K^{-1} kg^{-1}
Thermal diffusivity	κ_0	10^{-6} m^2 s^{-1}
Thermal expansivity	α_0	3×10^{-5} K^{-1}
Activation energy	E_a	157 kJ mol^{-1}
Activation volume	V_a	5.69 cm^3 mol^{-1}
Latent heat of melting	L	640 kJ kg^{-1}
Surface temperature	T_{surf}	220 K
Temperature difference across mantle	ΔT	1600 K
Rayleigh number	Ra	10^8

To simulate the effect of an initial crustal thickness variation caused by a Borealis-scale giant impact, we add a crustal cap of thickness $d_{cr} = 25$ or 50 km to the southern hemisphere. In CitcomS, this is accomplished by adding an insulating effect to elements in the upper 25 or 50 km of the computational mesh in the southern hemisphere. The insulating effect of the cap is parameterized using a reduction of thermal diffusivity κ_0 by a factor κ_{ins} and/or an enrichment in heat production Q by a factor Q_{ER} (crustal thermal diffusivity κ_{cr}=$\kappa_{ins} \cdot \kappa_0$ and crustal heat production Q_{cr}=$Q_{ER} \cdot Q$). We use a factor of 0.75 for κ_{ins}, representing the difference between the thermal conductivity of 2−3 W m^{-1} K^{-1} for crustal rocks (Clauser and Huenges, 1995) and 4 W m^{-1} K^{-1} for mantle rock (Hofmeister, 1999), and the density difference between the crust and mantle. Some simulations do not modify the diffusivity in the crust, to examine if a hemispherical difference in heat producing elements alone can drive degree-1 convection. Radiogenic elements are preferentially partitioned into the crust, and we use a crustal enrichment factor Q_{ER}=4 relative to the mantle, similar to the enrichment found at mid-ocean ridge basalts (Basaltic Volcanism Study Project, 1981). The northern hemisphere crust is excluded from most of our calculations because of its low volume and low concentration of heating elements relative to the southern crust. However, to examine the effect of including a thinner, less enriched northern crust, we complete a simulation (Run 4) in which we include a northern crust with thickness $d_{cr,N}$=25 km and radiogenic enrichment $Q_{ER,N}$=4, a southern crust of thickness d_{cr}=50 km and radiogenic enrichment Q_{ER}=10 (Taylor et al., 2006); both Q_{ER} and $Q_{ER,N}$ are relative to the mantle, which in Runs 4 and 5 is depleted in radiogenic elements by a factor Q_{DE}=0.5. We compare Run 4 to a case where both the northern and southern hemisphere have different thicknesses, but the same amount of radiogenic enrichment (Run 5).

Melt production is computed during the simulation using the tracer method described in

Li et al. (2016). The melt fraction (by mass) F is computed using the dry parameterization given by Katz et al. (2003). We extract melt when it exceeds a threshold value $F > 0.04$. On Earth, the melt extraction threshold is between 1 and 4 % (Li et al., 2016) (and references therein), and we expect a higher extraction threshold on Mars due to the lower gravity. Because the simulation is Boussinesq, we first add an adiabatic temperature gradient of 0.18 K km^{-1} before computing the melt fraction. We extract melt only at depths <540 km, where melt is buoyant on Mars (*e.g.,* Plesa and Breuer, 2014, and references therein). The latent heat of melting is used as a temperature sink in Equation 3. We sum the melt production for elements in the uninsulated northern and insulated southern hemispheres to compute the cumulative melt production in each hemisphere over time. It is important to note that we do not consider the effects of crust production on the calculation itself (except for latent heating); crust produced in either hemisphere does not alter the crustal thickness/enrichment assumed at the start of the simulation.

Although impact heating from a giant impact is expected to dissipate relatively quickly (*e.g.,* Roberts and Arkani-Hamed, 2017) we test this by including localized impact heating in two of our simulations. We insert an initial temperature pulse from a giant impact using the method described in Golabek et al. (2011) (and references therein). We examine initial temperature perturbations from impactors of radius $R_{imp} = 600$ and 1200 km. The resulting temperature perturbation roughly corresponds to a temperature increase of ∼400 K within $\sim 1.4R_{imp}$ of the impact site, radially decreasing in magnitude at further distances to <100 K at $\sim 2R_{imp}$ from the impact site.

2.4 Results

The results for 11 simulations, including a control run, are reported in Table 2.4. We determine the time until degree-1 convection is reached, t_{D1}, based on when the dominant spherical harmonic of the temperature in the lower, middle, and upper mantle are all degree-1. We also report the time that single plume convection, t_{SP}, is achieved, based on when a clear single plume is visible extending through the entire mantle, centered under the insulating crust in the southern hemisphere. Run 0 is a control case with no insulating cap that never achieved degree-1 convection for the simulation duration (600 Myr).

We find that an insulating cap can induce degree-1 convection on relatively short timescales <100 Myr (Table 2.4). In most simulations, large single plumes are observed under the insulating southern crust in <100 Myr (Fig. 2.4). This occurs even when the thickness of the southern cap is reduced to 25 km (Run 3), and when there is only a change in enrichment factor, with no change in thermal diffusivity in the crust (Run 2). Simulations with initial impact heating included (Runs 6 and 7) still achieve degree-1 convection in under 100 Myr, showing that variations in crustal thickness and composition result in a single upwelling under the insulating crust, even if earlier upwellings are concentrated under the impact site (Figure 2.5). A lower activation volume (Run 8) slightly increases t_{SP}, while a higher Rayleigh number (Run 9) decreases t_{SP} to only 16 Myr. Use of a higher activation energy

Table 2.2: Simulation Results

Run	d_{cr} (km)	κ_{ins}	Q_{ER}	Non-default parameters	t_{D1} (Myr)	t_{SP} (Myr)
0	–	–	–	–	never	never
1	50	0.75	4	–	3.3	59
2	50	–	4	–	3.3	60
3	25	0.75	4	–	3.3	60
4	50	–	10	$d_{cr,N}$=25 km, $Q_{ER,N}$=4, Q_{DE}=0.5	3.5	61
5	50	–	10	$d_{cr,N}$=25 km, $Q_{ER,N}$=10, Q_{DE}=0.5	never	never
6	50	0.75	4	Impact heating (R_i=600 km)	45*	60*
7	50	0.75	4	Impact heating (R_i=1200 km)	63*	89*
8	50	0.75	4	Ra=2.39×10^8, V_a=4.65 cm^3 mol^{-1}	3.5	67
9	50	0.75	4	Ra=2.39×10^9, V_a=4.65 cm^3 mol^{-1}	2.6	16
10	50	–	4	Ra=1.52×10^9, E_a=300 kJ mol^{-1}	43	158 (72)†

* This is the time when degree-1 convecton is dominant in the southern hemisphere. The initial impact heating perturbation causes earlier degree-1 patterns in the northern hemisphere.

† Time in parentheses indicates when upwellings are concentrated in the southern hemisphere, but not yet a single plume.

(Run 10) results in a longer timescale for single-plume convection ($\sim$ 160 Myr), although multiple plumes are still concentrated in the southern hemisphere in <75 Myr.

We also include a crust in both the southern and northern hemispheres, and show that increased enrichement in the thicker southern crust relative to the thinner northern crust results in development of a superplume under the southern crust (Run 4), while equal enrichment in the northern and southern crusts results in no degree-1 convection and multiple plumes in both hemispheres (Run 5). The relative concentration of radiogenic elements between the northern and southern crusts is the primary driver of degree-1 convection.

The focusing of upwelling(s) under the insulating cap increases melt production in the southern hemisphere (Fig. 2.6). In most simulations, a melt volume equivalent to 10–20 km of additional crust is produced in the insulated southern hemisphere. The amount of crust produced in the uninsulated northern hemisphere is negligible, except in simulations that begin with an impact heating perturbation (Runs 6 and 7). The crust production following impact heating is not expected to affect the overall result, because of its low volume/enrichment relative to the southern crust. For example, in Run 4 the simulation begins with 25 km of crust in the northern hemisphere (twice the thickness of northern crust produced in Runs 6 and 7), which is depleted relative to the more enriched southern crust, and a superplume still develops under the southern crust. In Runs 6 and 7, the cumulative crust production antipodal to the impact site eventually becomes greater than the northern,

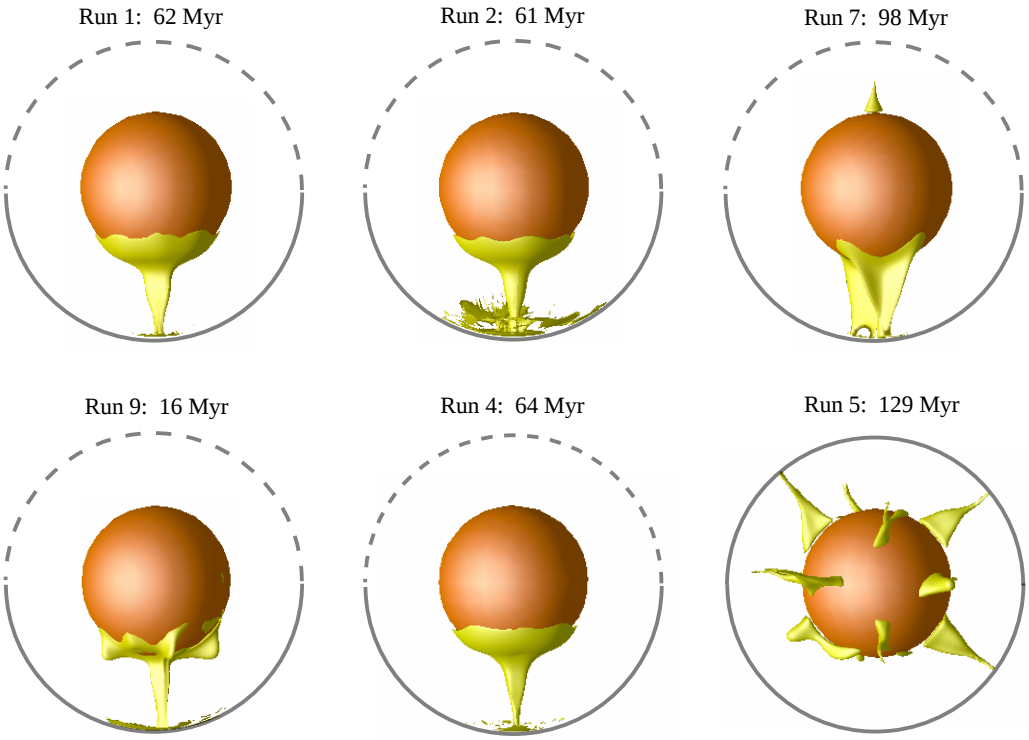

Figure 2.4: Sample outcomes for several simulations. Upwelling contours for residual temperature of 80 K, with the upper 100 km omitted for clarity. The southern crust (solid grey line) is enriched relative to the mantle and unenriched northern crust (dashed grey line). A single large upwelling under the insulating southern crust dominates the convection pattern in 10s to 100s of Myr. Run 7 has a residual lower mantle plume in the northern hemisphere, caused by the initial impact heating perturbation, but has still become dominated by degree-1 convection in <100 Myr. Run 9 uses a higher Rayleigh number and achieves single plume convection in ∼16 Myr. In Run 4, both the northern and southern crusts are enriched by a factor of 4 and 10, respectively, relative to the mantle, and the upwelling concentrates under the more enriched and thicker southern crust. In Run 5, the northern and southern crusts are enriched by the same amount relative to the mantle, and no degree-1 convection pattern develops.

post-impact crust production, even for R_{imp}=1200 km, indicating that melt production in the southern hemisphere is enhanced by the increased vigor of the degree-1 upwelling (e.g., Figure 2.5) and the increased subcrustal temperatures caused by the higher concentration of heating elements and decreased thermal diffusivity in the insulating cap.

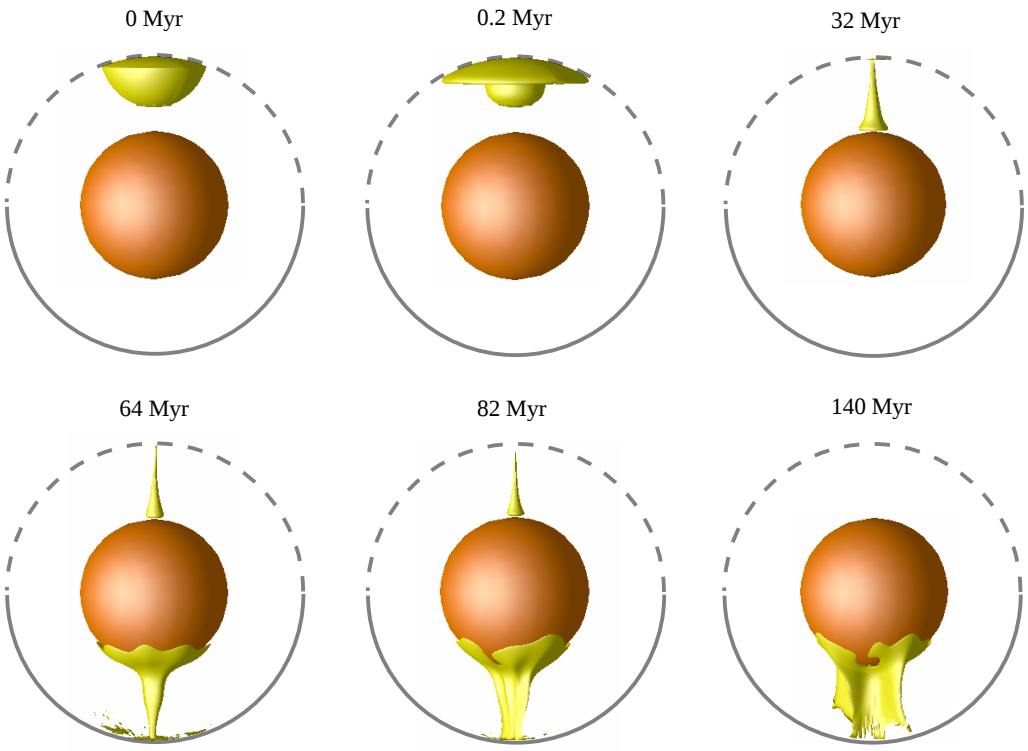

Figure 2.5: Evolution of Run 6 over time. The simulation begins with a temperature perturbation from a giant impact in the northern hemisphere, which quickly dissipates and causes a short-lived northern upwelling. Over time, an upwelling develops in the southern hemisphere under the insulating crust, and the northern upwelling dissipates. The southern plume dominates the convection pattern after ∼60 Myr. Upwelling contours are plotted for residual temperature = 80 K, with the upper 100 km omitted for clarity. The depleted northern crust and enriched southern crust are shown as dashed and solid gray lines, respectively.

2.5 Discussion

The results of our simulations, particularly τ_{SP} and the crust production rate, could vary depending on mantle rheology, composition, and melting model. The use of a highly temperature-dependent viscosity promotes long-wavelength convection, because low viscosity layers below cold boundary layers (and above hot ones) reduce horizontal shear dissipation, allowing for longer wavelength cells (Lenardic et al., 2006). Similarly, the additional inclusion of a viscosity jump in the mantle (*e.g.,* Roberts and Zhong, 2006) would likely decrease τ_{D1} and τ_{SP}. Inclusion of a non-newtonian rheology is not expected to have a significant effect on the vigor of convection on Mars (Hauck and Phillips, 2002), although it could raise mantle temperatures, allowing for enhanced partial melting even with a dry rheology (Grott and Breuer, 2009). Phase transitions in the mid-mantle have been shown to have a weak

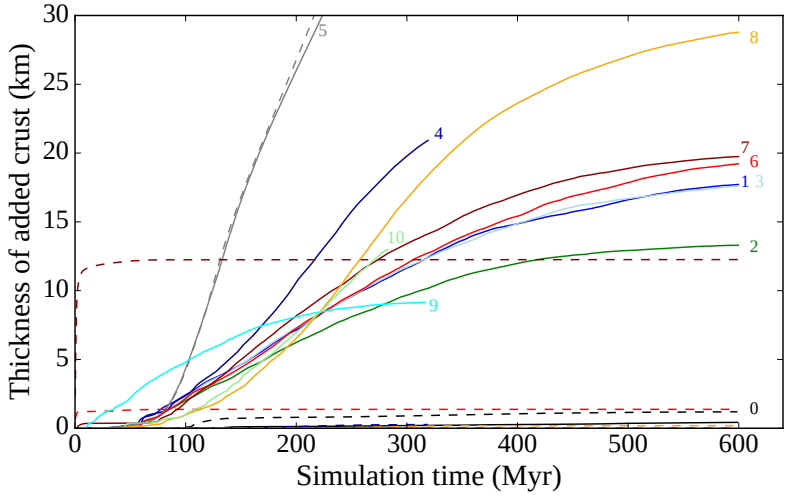

Figure 2.6: Melt production for all simulations over time. The cumulative thickness of additional crust produced is shown for the hemisphere with the insulated cap (solid lines) and the un-insulated hemisphere (dashed-lines). Run number is given next to the corresponding line. Thickness is computed by dividing the volume of melt production in each hemisphere by the surface area of each hemipshere. Crust production generally begins within the first 100 Myr, and continues for several hundred Myr before tapering off.

effect on Martian mantle dynamics (Ruedas et al., 2013a), and a perovskite+ferropericlase layer at the base of the mantle is unlikley (Ruedas et al., 2013b). Partial melting and water content can also have significant effects for mantle convection on Mars (Plesa and Breuer, 2014; Breuer et al., 2016; Ruedas et al., 2013b), motivating the use of more complex melting models that account for volatile depletion (*e.g.,* Li et al., 2016) or two-phase flow (*e.g.,* Dannberg and Heister, 2016). However, we do not expect the inclusion of more complex melting models to affect τ_{D1}, because most melt production occurs after degree-1 convection is achieved.

Cumulative crust production depends on the mantle composition and solidus (Kiefer et al., 2015), and the compressibility of melt extracted from depth (Dannberg and Heister, 2016). The solidus we use from Katz et al. (2003) is similar to other models of melting on Mars to the depths that we extract melt (Ruedas and Breuer, 2017), so a different the solidus should not affect our results. Inclusion of two-phase flow and melt migration/depletion could affect plume dynamics (Dannberg and Heister, 2016) and alter the crustal thickness distribution due to lateral transport of melt below the surface, however, the different timescales over which melt and mantle materials flow makes it computationally expensive to couple the two processes in global simulations, and effects of two-phase flow are generally localized and should not affect the global convection/melting patterns we observe. Although different melting models would have variable effects on cumulative melt production, examining the

full range of compositional considerations and variables such as melt extraction threshold and is outside of the scope of this work. Effects that reduce crust production, such as permeability extraction barriers (Schools and Montési, 2018), could be compensated for with increased mantle temperature or higher initial water content (which may the the case for early Mars; *e.g.*, Wade et al. (2017)). Thus, while more complex rheologies and melting models could affect crust production and τ_{D1}, we do not expect such considerations to alter our main conclusion that crustal heating/insulation promotes the development of degree-1 upwelling(s) and melt production under the thicker, enriched southern crust within 100s of Myr of a giant impact.

We show that for reasonable estimates of melt extraction, the additional crust produced in the southern hemisphere is within the constraints of Mars' inferred crustal thickness (*e.g.,* Neumann et al., 2004). Mars' crustal thickness may be lower or higher depending on the assumed density of the Martian crust. While Neumann et al. (2004) suggest an average crustal thickness of 45 km, a higher assumed crustal density (Wieczorek and Zuber, 2004; Baratoux et al., 2014; Plesa et al., 2016) could allow for an average crustal thickness up to 81 km. Likewise, lower (and possibly laterally varying) crustal densities could result in lower inferred crustal thicknesses (Goossens et al., 2017). Such considerations would result in varying constraints for crust production. In particular, higher assumed crustal thickness would increase the insulation and the melt production in our simulations. Higher crust production could be compensated for if a portion of the newly produced crust is subsequently recycled via delamination (*e.g.,* Rudnick, 1995).

Our model relies on a giant impact resulting in a northern crust depleted in radiogenic elements relative to the older southern crust. It is important to note, however, that such a dichotomy in radiogenic elements is not observed in gamma ray spectrometer measurements, which show little variation in Th and K abundance across the Martian surface (Taylor et al., 2006). Those measurements only sample the upper few tens of cm of regolith, and may not constrain the distribution of heat producing elements deeper in the crust (Plesa et al., 2016). Small differences in the distribution of K and Th may reflect different underlying compositions (*e.g.,* Karunatillake et al., 2007), but may also be explained by weathering and aqueous alteration (Dohm et al., 2009). Furthermore, observations suggest the southern crust is less dense than the northern crust (*e.g.,* Baratoux et al., 2014), implying a buried felsic component to the southern crust, which would be enriched in radiogenic elements such as K.

The short timescale we find for the crust to control the convective pattern is consistent with estimates of the influencing timescale of crustal thickness variations on mantle flow. We estimate the timescale for changes in crustal thickness to influence temperature and hence flow, τ_{crust}, as the time it takes for a temperature anomaly to develop under the crust comparable to the temperature difference between a mantle plume and the surrounding mantle ($\sim$100 K). We compare the time-dependent temperature solution for a solid half-space with a constant heat production rate (Carslaw et al., 1959) for an uninsulated medium with $k = 4$ W m^{-1} K^{-1} and $Q = 7.4 \times 10^{-8}$ W m^{-3} (typical for the first 100s of Myr of Mars' history (Wanke and Dreibus, 1994)), and an insulated medium with $\kappa_{ins} = 0.75$

and $Q_{ER} = 4$. The time it takes for the temperature difference between the insulated and uninsulated medium at 50 km depth to reach 80 K yields $\tau_{crust} \sim 37$ Myr. The timescale for temperature changes to influence flow, τ_{flow}, should scale as $\sim v/d$, where v is the plume velocity and $d = R_p - R_c$. Determining a scaling relationship for velocity in a spherical shell that is heated both from below and within is a challenge (Deschamps et al., 2012). We extrapolate the results of Weller et al. (2016), which scale fluid velocity versus $H_{int}Ra^{-1/3}$, to the values used in our simulations, which yields $v \sim 30$mm yr^{-1} and $\tau_{flow} \sim 58$ Myr. It thus seems reasonable that variations in crustal thickness could influence the convective pattern on <100 Myr timescales.

While we do not include the production or effects of melt-residue in our model, lateral variations in lithosphere thickness and highly viscous melt residue have been shown to drive differential rotation of the Martian lithosphere, resulting in the migration of the Tharsis plume to the dichotomy boundary (Zhong, 2009; Šrámek and Zhong, 2010). Differential rotation of the lithosphere with respect to the plume occurs even if the lithosphere remains stationary (Zhong, 2009; Šrámek and Zhong, 2010). We expect the plume to migrate and the lithosphere to remain stationary, because the equitorial bulge should stabilize the planet against large scale true polar wander (Daradich et al., 2008). The likely pre-Tharsis rotation pole of Mars is only $\sim 20°$ from the current pole, corresponding to the fossil bulge identified by Matsuyama and Manga (2010). We expect limited Tharsis-induced true polar wander to have occurred only after the plume migrated from the center of the Southern crust to emplace Tharsis at the dichotomy boundary. Migration of the Tharsis plume along such a track is evidenced by volcanic resurfacing and crustal thickening (Hynek et al., 2011; Cheung and King, 2014).

Because of the importance of giant impacts and mantle dynamics on planetary evolution, the origin of the crustal dichotomy is critical to understanding Mars' subsequent geophysical evolution. Both giant impacts and degree-1 convection have been proposed as a mechanism to produce an early hemispherical Martian dynamo (Stanley et al., 2008; Amit et al., 2011; Monteux et al., 2015). Various dynamo models can constrain and be constrained by the relation between the rate and distribution of crust production and the timescale of magnetic reversals (*e.g.,* Dietrich et al., 2015). Termination of the Martian dynamo could be modulated by the outgassing of mantle water over time (Sandu and Kiefer, 2012), which is related to the vigor of mantle convection and efficiency of melt production. The pattern and vigor of convection on early Mars could also have important implications for the compositional evolution of crust-mantle system (Grott et al., 2013), spatial and temporal variations in Martian lithosphere thickness (*e.g.,* Kiefer and Li, 2009; Grott and Breuer, 2010), and volcanic outgassing (*e.g.,* Grott et al., 2011), in addition to the geophysical constraints discussed in Section 1.1.

2.6 Conclusion

Our simulations show that a natural consequence of a Borealis-scale giant impact is the development of single-plume convection and significant melting in the southern hemisphere. This hybrid model is consistent with many of the geophysical observations related to crustal dichotomy formation. The formation of upwellings antipodal to the impact site allows for the preservation of the elliptical ditchotomy boundary from a giant impact. Development of degree-1 convection in the southern hemisphere is rapid (< 100 Myr), and could produce sufficient additional melt to further thicken the southern crust by $\sim$10–20 km, due to both the increased vigor of the degree-1 upwelling and the increased subcrustal heating caused by the insulating effect of the thicker southern crust. The short timescale in which additional crust is produced (within 100s of Myr of Mars' formation) can explain the formation of strong remnant crustal magnetic signatures in the southern hemisphere before the end of the Martian dynamo. Depending on the extent of crust production, extraction of melt to the surface could leave sufficient highly viscous melt residue under the southern crust to induce plume migration (Zhong, 2009; Šrámek and Zhong, 2010), resulting in the formation of Tharsis on the dichotomy boundary. The hybrid model for dichotomy formation can therefore bridge the gap between an early Borealis impact 4.5 Ga (Bottke and Andrews-Hanna, 2017) and a late Noachian formation of Tharsis >3.7 Ga (*e.g.,* Bouley et al., 2016), with broad implications for the geophysical evolution of Mars.

2.7 Acknowledgements

We thank Mingming Li for providing the melting subroutines for CitcomS and for helpful discussions. R.C. was supported by NSF EAR-1135382. This work used the Savio computational cluster resource provided by the Berkeley Research Computing program at the University of California, Berkeley (supported by the UC Berkeley Chancellor, Vice Chancellor for Research, and Chief Information Officer), the Extreme Science and Engineering Discovery Environment (XSEDE) (supported by National Science Foundation grant number ACI-1053575), and resources of the National Energy Research Scientific Computing Center, a DOE Office of Science User Facility (supported by the Office of Science of the U.S. Department of Energy under Contract No. DE-AC02-05CH11231). CitcomS is available through the Computational Infrastructure for Geodynamics (geodynamics.org). We thank reviewer A.C. Barr, one anoynmous reviewer, and editor W.B. McKinnon for comments and suggestions that clarified the presentation and refined the models.

Chapter 3

Superplume evolution and Tharsis formation: Migration, Magmatism, and Magnetism

3.1 Summary

An early martian superplume has been proposed to explain two key features of ancient Mars: the origin of Tharsis on the dichotomy boundary and the unique pattern of remanent crustal magnetic signatures. Formation of Tharsis on the dichotomy boundary (as opposed to any random point on the surface) is hypothesized to result from migration of a superplume originally formed under the thicker southern crust. Such a superplume could generate a large amount of melt residue that could promote plume migration to the dichotomy boundary. Migration of melting zones and crustal production from an evolving zone is also a mechanism proposed to explain the lineations of reversing polarity observed in Mars' remanent crustal magnetic field. A superplume can originate on Mars due a layered mantle viscosity, resulting in a superplume origin of the crustal dichotomy. Alternatively, a superplume could develop as a result of a giant impact on early Mars, forming under the thicker, more enriched (in radiogenic heat producing elements, HPEs) crust in the hemisphere opposite the impact. Regardless of the formation mechanism, the subsequent evolution of an early martian superplume and if it can explain the formation of Tharsis and the magnetic lineations is poorly constrained. Using a suite of mantle convection simulations, we examine the formation and evolution of superplumes on early Mars, with a focus on plume migration, melt production, and remanent magnetism. We find that it is difficult for large scale plume migration to occur when the superplume originates under a southern crust that is enriched in HPEs; explaining the pattern of magnetic lineations and origin of Tharsis remains a challenge.

3.2 Introduction

Two ancient geophysical features of Mars have been proposed to relate to formation of the Martian crustal dichotomy: the emplacement of Tharsis on the dichotomy boundary, and the pattern of lineations observed in the remanent crustal magnetic field (Figure 3.1). Both of these features are not readily explained by a giant impact origin of the crustal dichotomy, but may be related to degree-1 mantle convection (Zhong, 2009; Citron and Zhong, 2012).

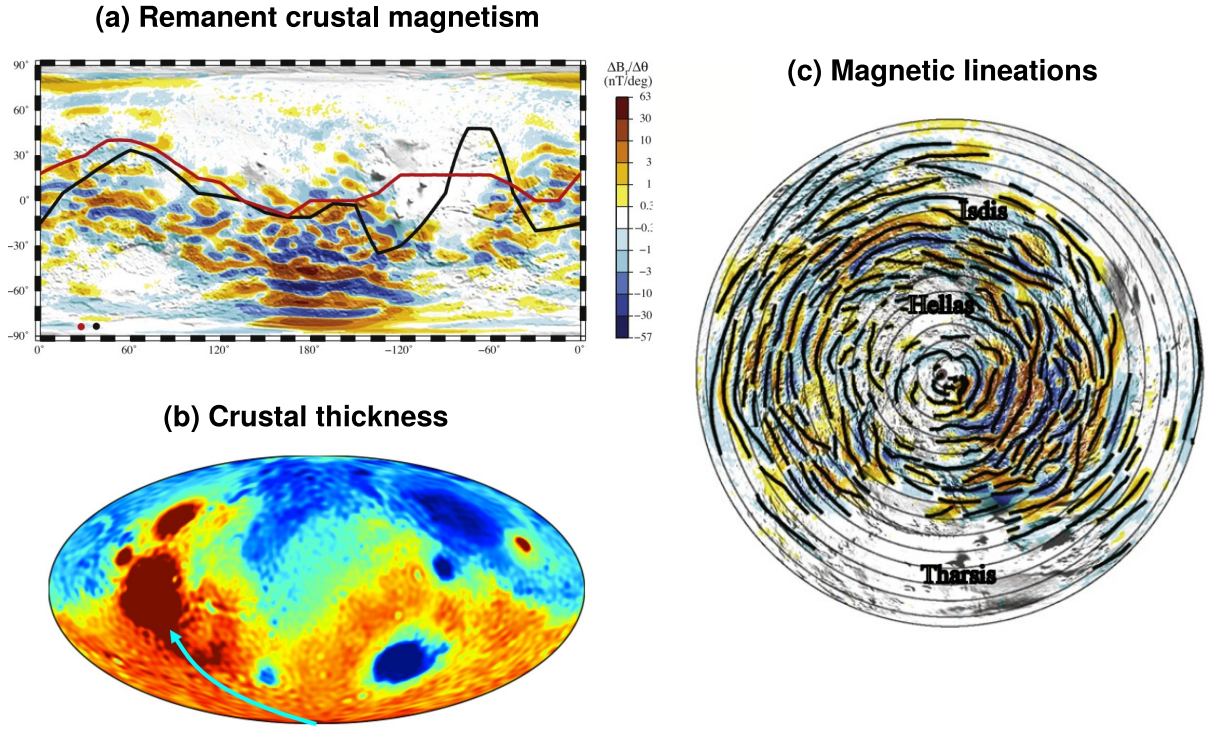

Figure 3.1: Remanent crustal magnetism and crustal thickness on Mars. (a) Map of remanent crustal magnetism on Mars using magnetic field data from Connerney et al. (2005), overlain on MOLA topography. Red and black lines trace possible dichotomy boundaries from Roberts and Zhong (2007), with corresponding centroids of a uniformly thick southern crust plotted as red and black circles. (b) Crustal thickness map of Mars using data from Genova et al. (2016). The proposed migration path of Tharsis is plotted as a cyan arrow. (c) Polar projection of the remanent crustal magnetic map from (a), centered on 76.5°E, 84.5°S, the best fit point from Citron and Zhong (2012) about which the magnetic lineations (thick black lines, data from Kobayashi and Sprenke (2010)) can be fit to a series of concentric circles (thin black circles, 1000 km spacing). Panels (a) and (c) are adapted from Citron and Zhong (2012).

The formation of Tharsis is peculiar in part because of its emplacement on the dichotomy boundary, a seeming coincidence given that it might have formed at any random location on the Martian surface. Zhong (2009) proposed that the location of Tharsis on the dichotomy boundary is due to migration of the superplume that formed the crustal dichotomy by thickening the crust in the present-day southern hemisphere. If degree-1 convection thickened crust in one hemisphere, the highly viscous melt residue produced by melt extraction and crust production would have created lateral variations of viscosity and thickness in the lithosphere, which could excite differential rotation of the lithosphere relative to the rest of the mantle (Zhong, 2009; Šrámek and Zhong, 2010). The lithosphere would rotate over the superplume, initially centered under the thicker southern crust, until the plume reaches the dichotomy boundary (*i.e.*, the edge of the melt residue). As the plume reaches the dichotomy boundary and encounters unmelted upper mantle material and a thinner lithosphere, enhanced melt production leads to the formation of Tharsis on the dichotomy boundary. Relative migration of the Tharsis superplume from the present-day south pole to Tharsis' location on the dichotomy boundary (proposed path shown in Figure 3.1) is supported by evidence of increased crustal thickness and volcanic resurfacing along such a track (Cheung and King, 2014; Hynek et al., 2011). However, it has also been proposed that Tharsis formed in-place, without prior migration. While the formation of Tharsis is still up for debate, migration of the Tharsis superplume from the southern hemisphere to the dichotomy boundary would create a causal link between the formation of the crustal dichotomy and Tharsis, two of the most prominent geophysical features of Mars.

Remanent crustal magnetization on Mars may also record processes controlled by dichotomy formation (Citron and Zhong, 2012). As shown in Figure 3.2a,b, although the magnetic anomalies are spread over the entire planet, they are much stronger in the southern hemisphere than in the north, suggesting a potential correlation between the strength of the magnetization and the dichotomy in crustal thickness. Like the crustal dichotomy, the magnetic signatures are also an ancient feature, necessarily emplaced before the demise of the Martian dynamo, which may have occurred $\sim$4.1 Ga, shortly after the Utopia impact (Lillis et al., 2013a). Large portions of the crust were then demagnetized by large impacts (such as Hellas, Argyre, and Isidis) and volcanic activity (such as Tharsis and Elysium). Although it has been suggested that formation of the dichotomy by a giant impact could have demagnetized the crust in the northern hemisphere, explaining the weak magnetic signatures there, Citron and Zhong (2012) show that the ejecta from such an impact could have thermally demagnetized the entire crust, even in the southern hemisphere. The remanent crustal magnetic signatures also contain a unique pattern of east-west trending anomalies, commonly referred to as lineations, that are 100-200 km wide and can be as long as 2000 km, and can alternate in polarity (*e.g.*, Connerney et al., 1999, 2005). Several mechanisms have been proposed to explain the formation and polarity reversals of the magnetic lineations, including plate tectonics (Connerney et al., 1999, 2005; Sprenke and Baker, 2000; Whaler and Purucker, 2005), accretion of terrains (Fairén et al., 2002), chemical remnant magnetization (Connerney et al., 1999), dike intrusion with a moving locus (Nimmo, 2000), and plume tracks from lithospheric drift (Kobayashi and Sprenke, 2010). Citron and Zhong (2012)

proposed that the lineations formed coincident with dichotomy formation due to degree-1 mantle convection. In this scenario, the superplume that thickens the crust in the southern hemisphere produces new crust radially progressively further from the plume head, in a series of concentric circles. If the new crust is emplaced in the presence of an alternating magnetic field, the magnetic signatures would form a series of concentric circles of alternating polarity. Citron and Zhong (2012) showed that the lineations can be approximated with a series of concentric circles that are centered near the centroid of the thicker southern crust (Figure 3.1c), which would be expected if the lineations and thicker crust were both generated by crustal production spreading radially from a superplume.

Both the magnetic lineations and the formation of Tharsis have proposed causal links to dichotomy formation via degree-1 mantle convection. However, the feasibility of producing these two features from an evolving martian superplume has not been fully tested. For the magnetic lineations, the formation mechanism proposed by Citron and Zhong (2012) has not been supported with a numerical model showing a superplume would generated crust in a pattern consistent with the distribution of magnetized crust. For the formation of Tharsis, while Šrámek and Zhong (2010) showed that rotation of the lithosphere over a superplume can result in the formation of Tharsis at the dichotomy boundary, such plume migration has not been examined in the context of the hybrid model of dichotomy formation discussed in Chapter 2. Accordingly, in this chapter we model superplume formation and evolution on Mars to determine the feasibility of generating the magnetic lineations and/or Tharsis following crustal dichotomy formation on early Mars.

We propose an extension of the hybrid model discussed in Chapter 2, in which the magnetic lineations and the formation of Tharsis are causally linked to the formation of the crustal dichotomy (Figure 3.2). In this scenario, an initial dichotomy in crustal thickness generated by a giant impact causes a superplume to develop under the thicker, more enriched (in HPEs) southern crust, as in Chapter 2 (Figure 3.2a). Crust produced by the superplume is generated progressively further from the center of the upwelling, due to the increased viscosity and difficulty of re-melting upper mantle regions where melt was already extracted. If this occurs in the presence of an alternating magnetic field, a series of magnetic lineations are produced, corresponding to a series of roughly concentric circles radiating from the plume center (Figures 3.1c and 3.2b). The additional crust produced in the southern hemisphere results in a layer of highly viscous melt residue under the southern crust, which can excite superplume migration until the plume reaches the dichotomy boundary where it forms Tharsis (Figure 3.2c,d). In contrast to Šrámek and Zhong (2010) in which the lithosphere rotated with respect to the mantle, we expect the plume to migrate under the lithosphere/crust, because the rotational bulge of the planet would resist reorientation away from the equator, preventing differential rotation of the elastic lithosphere.

In the extended hybrid model of dichotomy formation (Figure 3.2), there are two main hypotheses to test: (1) that crust can be produced progressively radially away from the superplume in a manner consistent with the formation of the magnetic lineations, and (2) that viscous melt residue produced by the thickening of the southern crust can result in plume migration and the formation of Tharsis on the dichotomy boundary. Either of these

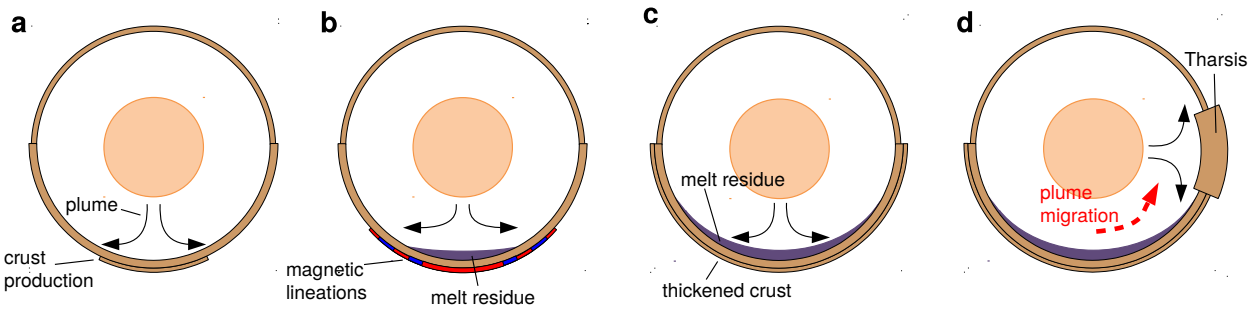

Figure 3.2: Proposed model of magnetic lineation formation, plume migration, and Tharsis emplacement. (a) A superplume develops in the southern hemisphere due to the post-impact variation in crustal thickness and composition (see Chapter 2). (b) As melt is produced and the crust is thickened above the plume, mantle where melt has been extracted results in highly viscous and harder to remelt (*i.e.*, melt residue). Zones of melt production and extraction therefore progress radially outward from the plume center. If this process occurs in the presence of a reversing magnetic field, magnetic lineations could be produced (red and blue segments). (c) A layer of highly viscous melt residue is formed under the southern crust, due to the melt production generated by the degree-1 upwelling(s) in the southern hemisphere. (d) Because of the viscous melt residue, the upwelling can no longer transport heat to the surface, the plume therefore migrates until it reaches the edge of the melt residue (the dichotomy boundary), where it breaches the surface and forms Tharsis.

processes could occur without the other, so a null result for the formation of the lineations by a superplume does not preclude the possibilty of plume migration and Tharsis formation, and vice versa. It is also possible that neither hypothesis is feasible, which would further constrain the types of processes required to explain early Mars geodynamics. In order to determine the viability of either of these processes occurring in the context of the hybrid model of dichotomy formation, we build on our work from Chapter 2. We conduct a suite of numerical simulations of (post-impact) superplume formation on early Mars, with a particular focus on subsequent crustal production and plume migration.

3.3 Methods

Simulations of mantle convection are very similar to those conducted in Chapter 2. We conduct 3D simulations using the CitcomS mantle convection code (Zhong et al., 2000; Tan et al., 2006) with the same resolution as in Chapter 2. However, instead of using the Boussinesq approximation we use the extended Boussinesq approximation, adding an adiabatic heating term to the governing equations (we also allow thermal expansivity and diffusivity to vary with depth):

$$\nabla \cdot \mathbf{u} = 0 \tag{3.1}$$

$$-\nabla P + \nabla \cdot [\eta(\nabla \mathbf{u} + \nabla^T \mathbf{u})] + \mathrm{Ra}\alpha(r) T \mathbf{e_r} = 0 \tag{3.2}$$

$$\frac{\partial T}{\partial t} + \mathbf{u} \cdot \nabla T = \nabla \cdot (\kappa(r) \nabla T) + H_{int} + H_A - H_L \tag{3.3}$$

where H_A is adiabatic heating, $\kappa(r)$ and $\alpha(r)$ are non-dimensional prefactors allowing thermal diffusivity and expansivity, respectively, to vary with depth (as in Roberts and Zhong (2006)), and the rest of the variables are as defined in Section 2.3. Model constants are similar to those in Chapter 2, with some slight variations, as shown in Table 3.1. In particular, we use a larger core radius, based on recent studies (Plesa et al., 2018; Samuel et al., 2019), and use a thermal diffusivity and thermal expansivity that linearly vary with depth from the surface to the core-mantle boundary (CMB) as in Roberts and Zhong (2006); Šrámek and Zhong (2010). All non-dimensional variables (*e.g.*, *Ra* and H_{int}) are defined using the dimensional variable values at the CMB.

Although in Chapter 2 we considered radiogenic heating with decay, here we use a constant internal heating rate H_{int}. Because we are interested in the Noachian evolution of the mantle (the first 500-700 Myr after Mars' formation), approximating the heating rate as constant in this time period reduces the complexity of the model and allows us to focus

Table 3.1: Model Constants

Parameter	Symbol	Value	unit
Planetary radius	R_p	3400	km
Core radius	R_c	1850	km
Gravitational acceleration	g	3.73	m s^{-2}
Mantle density	ρ_m	3400	kg m^{-3}
Specific heat	C_p	1200	J K^{-1} kg^{-1}
Thermal diffusivity (CMB)	κ_{CMB}	2×10^{-6}	m^2 s^{-1}
Thermal diffusivity (surface)	κ_{surf}	1×10^{-6}	m^2 s^{-1}
Thermal expansivity (CMB)	α_{CMB}	2×10^{-5}	K^{-1}
Thermal expansivity (surface)	α_{surf}	4×10^{-5}	K^{-1}
Effective activation energy	E^*	80-157	kJ mol^{-1}
Effective activation volume	V_a	2-6	cm^3 mol^{-1}
Latent heat of melting	L	640	kJ kg^{-1}
Surface temperature	T_{surf}	220	K
Initial mantle temperature	T_m	1400-1600	K
Temperature difference across mantle	ΔT	1580-1780	K
Radiogenic heating rate	Q_0	6.56×10^{-8}	W kg^{-1}

our study on the effect of other model parameters. Simulations can require some spin-up time to reach a stable convective state, and decaying heat production would make it difficult to decouple the effect of varying viscosity parameterizations from differences in heat production introduced by spin up times that change depending on the simulation parameters. While some spin up time to achieve convection is expected, it is difficult to estimate given the uncertainty in the true post-accretion temperature of Mars that would define the initial temperature perturbation of the mantle. Therefore, we use a constant radiogenic internal heating rate $Q_0 = 6.56 \times 10^{-8}$W kg^{-1}, which corresponds to the average heating rate from 4.5 to 3.7 Ga given the initial concentrations of U, Th, and K from Wanke and Dreibus (1994), which are based on compositional analysis of the SNC Martian meteorites. Because we are only interested in the model evolution until the end of the Noachian (∼3.7 Ga), using the average heating rate from the pre-Noachain and Noachian allows us to reduce the complexity of the model and better compare simulations in which other model parameters are varied. It is possible that the internal heating rate is higher (*e.g.*, Lodders and Fegley, 1997) or lower (*i.e.*, sub-chondritic (Phillips et al., 2008)) than the estimate of Wanke and Dreibus (1994), however, we do not vary this parameter due to limitations in computational resources and the number of additional simulations it would require.

We use the same temperature-dependent viscosity as in Section 2.3, except we add a viscosity layering prefactor (as in Roberts and Zhong (2006)) because in some simulations we include a viscosity jump in the mid-mantle. The non-dimensional pressure- and temperature-dependent viscosity is given by:

$$\eta = \eta_0(r) \exp\left(\frac{E' + V'(1-r)}{T + T_s} + \frac{E' + V'(1-R_c)}{1 + T_s}\right) \tag{3.4}$$

where $\eta_0(r)$ is the non-dimensional viscosity prefactor that can be used to impose a viscosity jump in the mid-mantle, and the rest of the parameters are as defined in Section 2.3. The dimensional viscosity is given by $\eta_{dim} = \eta_{ref} \cdot \eta$, with the reference viscosity defined at the CMB.

The extent that mantle viscosity depends on temperature is controlled by the activation energy E_a, which depends on the rheology and creep regime. The creep regime for the martian mantle is uncertain, and the mantle could deform by either diffusion creep or dislocation creep. We use a Newtonian viscosity formulation, meaning the power law relating strain rate to stress has a stress exponent $n = 1$, which is appropriate for diffusion creep but not for dislocation creep. For non-Newtonian dislocation creep we rely the approximation of Christensen (1984), using an effective activation energy $E^* = E_a/n$ where n is the stress exponent. For example, olivine dislocation creep has E_a=470 kJ mol^{-1} and n=3 (Mei and Kohlstedt, 2000), yielding E^*=157 kJ mol^{-1}. The effective activation volume is similarly defined as $V^* = V_a/n$, where V_a is the activation volume.

Because the viscosity profile of the mantle can strongly influence the convective behavior, we test three different viscosity models representing three different levels of temperature and depth dependence of viscosity: weak, medium, and strong. The weak temperature and depth dependence viscosity model has E^*=80 kJ mol^{-1} and V^*=2 cm^3 mol^{-1}, representing

a dislocation creep regime with E^* and V^* values from Samuel et al. (2019), based on constraints from the orbital evolution of Phobos. The medium temperature and depth dependence viscosity model is also for the dislocation creep regime, but with E^*=157 kJ mol^{-1} and V^*=6 cm^3 mol^{-1}, based on experimental studies (*e.g.*, Mei and Kohlstedt, 2000; Karato and Wu, 1993). The strong temperature and depth dependence viscosity model has E^*=157 kJ mol^{-1} and a higher V^*=6 cm^3.

Because the viscosity depends on temperature, for each viscosity dependence model we consider both a hot and cold case, where we adjust the initial mantle temperature and the total temperature difference across the mantle. For each viscosity temperature and depth dependence (weak, medium, or strong) and temperature model (hot or cold), we consider a case with and without a viscosity jump in the mid-mantle (for a total of 12 model types). The existence of a viscosity jump in the mid-mantle in uncertain, but has been suggested based on observations of a weak upper mantle on Earth. A viscosity jump could result from a transition from diffusion to dislocation creep (Karato and Wu, 1993), partial melting in the upper mantle (Zhong and Zuber, 2001), or a mid-mantle mineralogical phase transition (Keller and Tackley, 2009). A sharp increase in viscosity in the mid-mantle can strongly influence the convective pattern, and has been shown to promote more long-wavelength (even degree-1) convection on Mars (*e.g.*, Roberts and Zhong, 2006). If a viscosity jump does exist, the depth and magnitude of the viscosity increase are still unconstrained. We place the viscosity jump in the mid-mantle, at a depth of 850 km. While Roberts and Zhong (2006) use a 25-fold increase in viscosity in the mid-mantle, we use a 50-fold increase similar to Plesa et al. (2018). When we use a 50-fold increase in viscosity in the mid-mantle, we lower the effective activation volume V^* from 6 cm^3 mol^{-1} to 2 cm^3 mol^{-1}, to produce a similar total viscosity change across the mantle as in the simulations with no viscosity jump.

The initial mantle temperatures for the hot and cold models vary depending on the viscosity model, and are shown with the other model parameters in Table 3.2. The initial viscosity and temperature profiles are shown in Figure 3.3. Initial temperature profiles include top and bottom thermal boundary layers determined by a conductive half-space cooling/heating model (error function) with a time of 50 Myr. As in Chapter 2, we start the simulation with random perturbations of 0.01 to the non-dimensional temperature in the mid-mantle.

For each of the 12 model types, we run three different stages of simulations: pre-impact, post-impact, and superplume evolution. The pre-impact simulations determine the convective pattern of each model with no imposed crustal structure. The post-impact simulations use the output of the pre-impact simulations and determine how the convective pattern changes when we impose a hemispherical difference in crustal thickness, with the goal of determining for which models degree-1 (superplume) convection develops (with the upwelling(s) centered under the thicker southern crust). The superplume evolution simulations use the output of the post-impact simulations (only those where a superplume formed) and determine how new crust is distributed and if the superplume migrates as a result of viscous stiffening due to melt extraction.

For pre-impact simulations, we run each model for 100s of Myr until some form of multi-

plume convection is achieved that can be used as a starting point for the post-impact simulations. We expect most models to result in multi-plume convection, although longer wavelength convection is possible for simulations with a viscosity jump in the mid-mantle. Each simulation is labeled as follows: `Vweak`, `Vmed`, and `Vstrong` correspond to weak, medium, and strong temperature-dependence of viscosity, and `Thot` and `Tcold` correspond to hot or cold mantle temperature parameters. We also include a `jump` label if the simulation includes a 50-fold viscosity increase in the mid-mantle. For example, the `Vweak_Thot_jump` simulation uses the weak temperature and depth dependent viscosity model, the hot temperature parameters, and includes a viscosity jump in the mid-mantle.

For the post-impact simulations, we begin each simulation with the output of the corresponding pre-impact simulation at a timestep where multi-plume convection has already begun. We impose a post-impact crustal thickness variation, and determine if a superplume forms under the thicker (and possibly more enriched) southern crust. We use two post-impact crust models, both of which use a northern crust 25 km thick and a southern crust 50 km thick. The first post-impact crust model contains a southern crust that is more enriched in radiogenic heat producing elements than the northern crust, as discussed in Chapter 2. We enrich the southern crust relative to the mantle by a factor of $Q^S_{ER} = 5$, and the northern crust relative to the mantle by a factor of $Q^N_{ER} = 2$. In order to obtain a bulk mantle heating rate equal to Q_0, we offset the enrichment of the crust by depleting the mantle in radiogenic heat producing elements by a factor of $Q_{DE} = 0.8$. Thus, relative to the bulk heating rate Q_0, the crust has a heating production rate $Q^S_{cr} = Q^S_{ER} \cdot Q_{DE} = 4$ and $Q^N_{cr} = Q^N_{ER} \cdot Q_{DE} = 1.6$. In this model we do not include any decrease in the thermal conductivity of the crust. For simulations that use the crustal enrichment model ($Q^N_{ER} = 2$, $Q^S_{ER} = 5$) we add `cr25` to the

Table 3.2: Model labels and adjusted parameters

Simulation label	E^* (kJ mol^{-1})	V^* (10^{-6} cm^3 mol^{-1})	T_m (K)	ΔT (K)	η_{ref} (10^{20} Pa s)
`Vweak_Tcold`	80	2	1400	1580	1.58
`Vweak_Thot`	80	2	1600	1780	1.58
`Vweak_Tcold_jump`	80	2	1400	1580	6
`Vweak_Thot_jump`	80	2	1600	1780	6
`Vmed_Tcold`	157	4	1400	1680	0.71
`Vmed_Thot`	157	4	1500	1780	0.71
`Vmed_Tcold_jump`	157	2	1400	1680	0.71
`Vmed_Thot_jump`	157	2	1500	1780	0.71
`Vstrong_Tcold`	300	6	1480	1580	0.5
`Vstrong_Thot`	300	6	1600	1750	0.5
`Vstrong_Tcold_jump`	300	2	1480	1580	1
`Vstrong_Thot_jump`	300	2	1600	1750	1

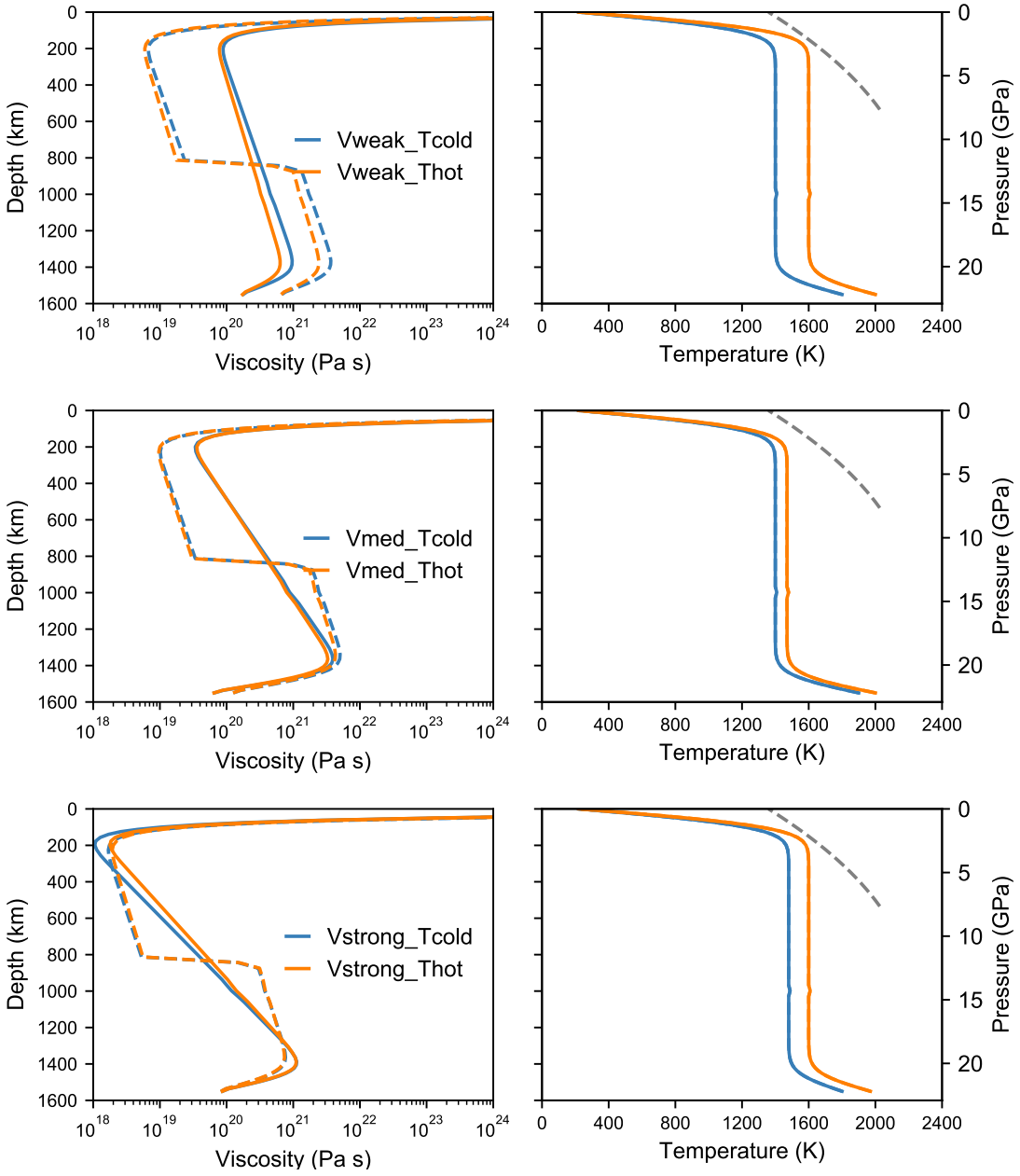

Figure 3.3: Initial viscosity and temperature profiles. The initial variation of viscosity and temperature with depth is shown for the models with weak, medium, and strong temperature and depth dependence of viscosity. For each viscosity type, the hot and cold temperature are plotted in orange and blue, respectively. Models that include a viscosity jump in the mid-mantle are plotted with a dashed line. The solidus from Katz et al. (2003) is plotted in dashed grey where melt extraction is considered (<7 GPa).

simulation label. We also use some other models with slightly different crustal heating and thickness parameters. Each simulation is labeled with the corresponding crust model as in Table 3.3.

For superplume evolution simulations, we determine the distribution of melt production and if melt extraction can induce superplume migration. We only conduct superplume evolution simulations for models that resulted in superplume formation in the post-impact simulations. We initialize each superplume evolution simulation with the temperature profile from the corresponding post-impact simulation after a superplume formed (centered under the thicker southern crust). We use a melt-extraction model that computes the crust production and melt extraction. Melt production is computed using the tracer method described in Chapter 2, based on the formulation from Li et al. (2016). We extract melt when it exceeds a threshold value $F > 0.02$. Because the simulation uses the extended Boussinesq approximation, we no longer add the adiabatic temperature gradient before computing the melt fraction, as we did in Chapter 2. We extract melt only at depths less than 540 km ($<$ 7 GPa) where melt is buoyant with respect to the mantle on Mars (Plesa and Breuer, 2014). The time and location of extracted melt is recorded to determine the spatio-temporal distribution of added crust. As in Chapter 2, we do not consider the effects of crust production on the calculation itself (except for the effect of latent heat as a temperature sink in Equation 3.3); crust produced in either hemisphere does not alter the crustal thickness/enrichment assumed at the start of the simulation. Melt extraction can affect the simulation because it devolatilizes (dehydrates) the mantle relative to portions of the mantle that have not been partially melted. Mantle that has increased viscosity due to melt extraction (dehydration) is termed 'melt residue'. We adopt the melt residue parameterization of Šrámek and Zhong (2012), increasing the viscosity of melt residue with either a step function or continuously varying function. We test both cases. For the step function, regions with >5% melt extraction are given a 200-fold viscosity increase. For the continuously varying case, the viscosity increase from melt extraction is given by $\eta_F = [1 + F(D_H^{-1} - 1)]^p$, up to a maximum of 200, where F is the degree of melt extraction, D_H=0.01 is the distribution coefficient of hydrogen, and p is the exponent for hydrogen viscosity variation (see Šrámek and Zhong (2012), and references therein). The step and continuous viscous stiffening parameterizations are labeled as 'Step Melt Residue' and 'Continuous Melt Residue' in the corresponding plots. We compute melting as described above in the pre- and post-impact simulations, but we only add the melt residue calculation to the superplume evolution simulations. While it is possible to have included melt residue in the pre- and post-impact simulations, we include

Table 3.3: Crust Models

Crust Model	d_{cr}^N (km)	d_{cr}^S (km)	Q_{ER}^N	Q_{ER}^S	Q_{DE}
`cr25`	25	50	2	5	0.8
`cr25B`	25	50	2	5	0.5
`cr14`	0	50	1	4	1

it only when examining superplume evolution in order to isolate the effect of melt residue on superplume migration and crust production. Inclusion of melt residue in the pre- and post-impact simulations could overly stiffen the lithosphere from partial melting, particularly since we do not account for delamination of the crust/lithosphere in our simulations; Šrámek and Zhong (2012) also only invoked the melt residue parameterization on models that used a superplume as the initial condition. For superplume evolution simulations where we track melt residue, we add `meltres` to the simulation label.

Although most simulations are conducted with the parameters described above, we sometimes re-run a model with a slightly different temperature or melting parameterization. This is done because melting is a highly temperature dependent process, where a change in 100K can greatly affect the melt production and the associated crust production and melt residue. Accordingly, for some models we might slightly change the temperature or melting model to see if the result changes significantly. Such models are described and labeled accordingly when they appear in subsequent sections.

3.4 Results

3.4.1 Pre-impact simulations

The results for the pre-impact simulations are shown in Figure 3.4. The simulations are used to produce the initial conditions for the post-impact simulations. Because a giant impact is expected to occur <100 Myr after Mars' formation, we use the temperature distribution at 100 Myr (or 250 Myr for the `Vweak` simulations) as the initial temperature field at the start of the post-impact simulations. As seen in Figure 3.4, after 100 Myr the simulations have reached convective states with multiple plumes (or longer-wavelength convection when a viscosity jump is included).

Although we use each simulation's early convective state as the initial condition for the corresponding post-impact simulations, we allow each simulation to proceed for >500 Myr to examine the long-term evolution. This allows us to further explore the parameter space in which degree-1 or long-wavelength convection could develop on early Mars, a proposed endogenic mechanism of crustal dichotomy formation (Roberts and Zhong, 2006) (as discussed in Chapter 2.

We find that longer wavelength convection develops for simulations with a viscosity profile that depends more strongly on temperature (and pressure). The inclusion of a 50x viscosity jump in the mid-mantle also results in longer wavelength convection, resulting in upwellings that are annular, ridge-like, or long-wavelength plumes, depending on the temperature and depth dependence of viscosity. Our results are in agreement with other studies that find that strongly temperature and depth dependent viscosity results in longer wavelength convection, an effect that can be enhanced by the inclusion of a viscosity jump in the mid-mantle (*e.g.*, Roberts and Zhong, 2006; Šrámek and Zhong, 2012).

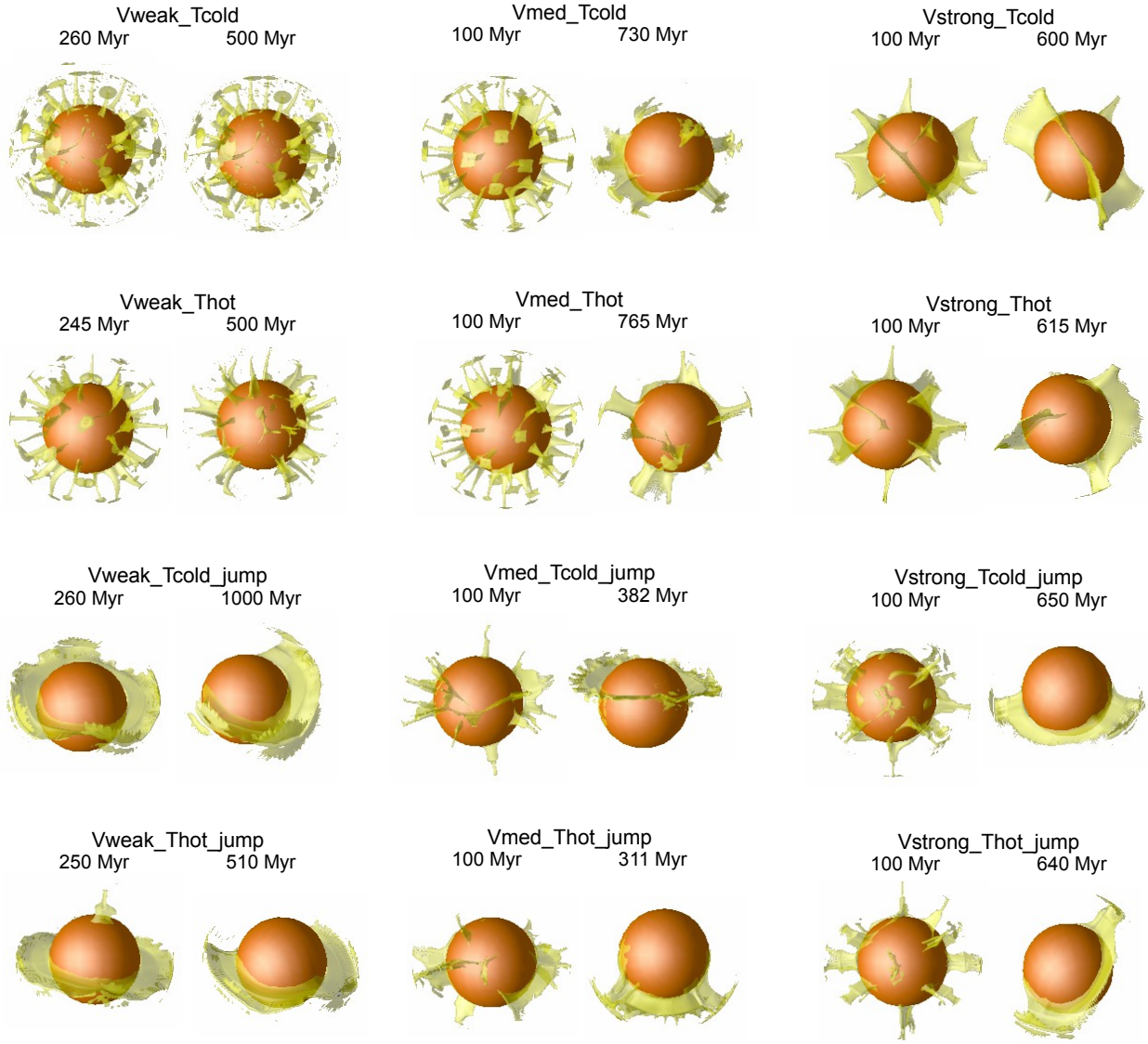

Figure 3.4: Outcomes for pre-impact convection simulations. Upwellings contours are plotted in yellow for residual temperatures of 30-70 K (depending on the simulation). All simulations from Table 3.2 are shown, with the columns corresponding to weak, medium, and strong temperature and depth dependence of viscosity, and rows corresponding to cold and hot mantles (with and without a mid-mantle viscosity jump). For each model we show a snapshot of the early convective pattern and the end state of the simulation. The early snapshots (at 100 Myr, except for the `Vweak` cases) correspond to the temperature states used as initial conditions in the post-impact simulations.

3.4.2 Post-impact simulations

For the post-impact simulations where the crust is more enriched in HPEs in the southern hemisphere (`cr25`), we find that the HPE-enrichment of the southern crust promotes superplume formation in the southern hemisphere. As shown in Figure 3.5 and Table 3.4, an enriched southern crust can induce superplume formation in 100s of Myr. While superplumes do not form in all simulations, the `cr25` crust model induces superplume formation for model parameters that would not have developed degree-1 convection in the absence of a crust model. For example `Vweak_Thot_jump` is shown in Figure 3.4 to develop annular or ridge-like convection without a crust, but is shown in Figure 3.5 to develop degree-1 convection when an enriched southern crust is added. An enriched southern crust can induce superplume formation even with no viscosity jump in the mid-mantle, although this is easier when using a strongly temperature and depth dependent viscosity (see `Vstrong_Tcold`, Figure 3.5c).

In the context of the hybrid model of dichotomy formation, our results for the `cr25` crust model show that an enriched crust in the southern hemisphere can induce superplume formation under a wider range of parameters than those explored in Chapter 2. Inclusion of a viscosity jump in the mid-mantle makes superplume formation easier, but superplumes can still form when a viscosity jump is not included, although the viscosity must be highly temperature and depth dependent. Even though crust is also included in the northern hemisphere, the larger thickness and higher degree of enrichment of the southern crust promotes superplume formation.

Table 3.4: Timescales of superplume formation for a post-impact crust where the southern crust is more enriched in HPEs (crust model `cr25`).

Simulation label	τ_{SP} (Myr)	Simulation label	τ_{SP} (Myr)
`Vweak_Tcold_cr25`	–	`Vweak_Tcold_cr25_jump`	<356
`Vweak_Thot_cr25`	–	`Vweak_Thot_cr25_jump`	<213
`Vmed_Tcold_cr25`	$< 500^*$	`Vmed_Tcold_cr25_jump`	<300
`Vmed_Thot_cr25`	$< 500^*$	`Vmed_Thot_cr25_jump`	$< 300^*$
`Vstrong_Tcold_cr25`	<340	`Vstrong_Tcold_cr25_jump`	<323
`Vstrong_Thot_cr25`	< 475	`Vstrong_Thot_cr25_jump`	<320

* Not a single plume, but multiple plumes concentrated in the southern hemisphere.

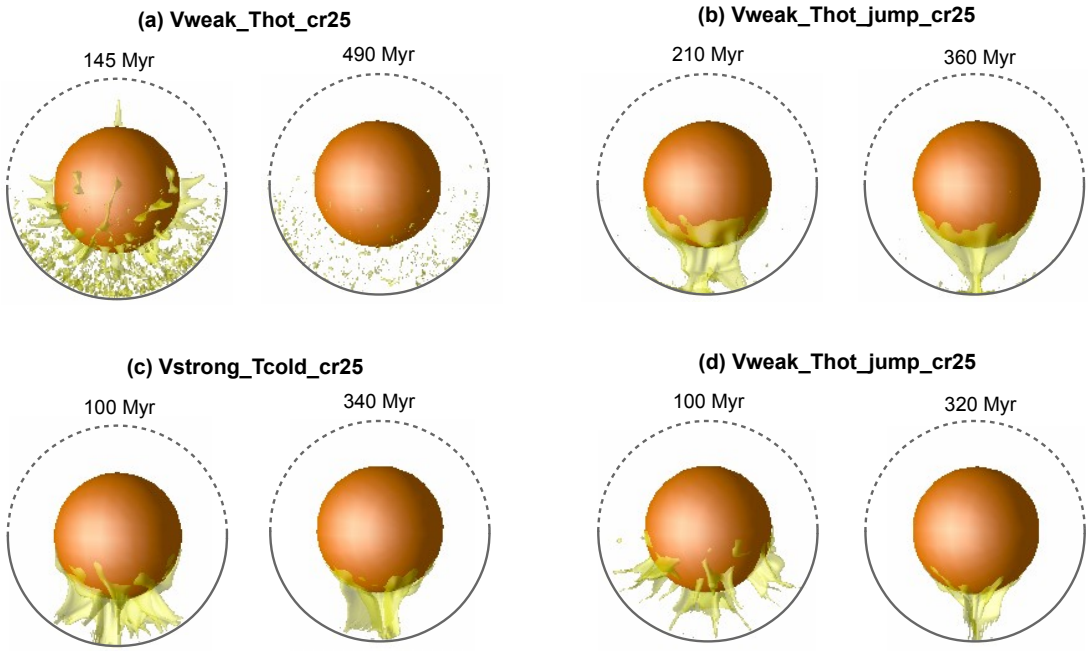

Figure 3.5: Example outcomes for post-impact simulations. Upwellings contours in yellow show residual temperatures of 30-70 K. For these post-impact models, we show the results for the `cr25` post-impact crust model, in which the crust was enriched by a factor of 5 in the southern hemisphere (50 km thick) and 2 in the northern hemisphere (25 km thick), relative to the depleted mantle. In the simulation snapshots the more enriched southern crust is marked by a solid grey line, and the less enriched and thinner northern crust is marked by a dashed grey line. (a,b) For weakly temperature and depth dependent viscosity, when there is no viscosity jump plumes concentrate under the southern crust but then dissipate after 100s of Myr, but when a viscosity jump is included a superplume develops under the southern hemisphere. (c,d) For strongly temperature and depth dependent viscosity, a superplume develops both with and without a viscosity jump.

3.4.3 Superplume evolution

3.4.3.1 Plume migration

To examine the influence of melt residue on plume migration, we first conduct a set of simulations with parameters similar to Šrámek and Zhong (2012). These simulations are labeled SZ1-4. The parameters are identical to those used in Šrámek and Zhong (2012), except that $\Delta T = 1700$ K instead of 1780 K. As in Šrámek and Zhong (2012) each model has a 25x viscosity jump in the mid-mantle. Each model begins with an initial temperature distribution corresponding to a superplume. Run SZ1 uses no crust. Run SZ2-4 use the `cr14` crust model (50 km thick crust in the southern hemisphere, enriched by a factor of 4 relative

to an undepleted mantle, and no crust in the northern hemisphere). Run SZ3 uses a higher temperature difference (1750 K instead of 1700 K). Run SZ4 uses a continuous melt residue parameterization, while SZ1-3 use a step melt residue parameterization. One main deviation from Šrámek and Zhong (2012) is the use of no slip upper velocity boundary. While Šrámek and Zhong (2012) use a free-slip surface to see if the lithosphere differentially rotates relative to the mantle, we use no-slip to simulate a surface fixed in place by the equatorial bulge and examine if the plume moves relative to the lithosphere/crust.

The results for the benchmarking cases SZ1-4 are shown in Figure 3.6. When no crust is included (SZ1, Figure 3.6a), large-scale plume migration occurs. The melt residue promotes plume migration of 90 degrees in 530 Myr. The plume moves relative to the crust, and not necessarily in a straight line but in a slightly curved and non-direct path. We did not observe, however, such large-scale plume migration when an enriched crust was included in the southern hemisphere (SZ2-4, Figure 3.6b-d). In models SZ2 and SZ3, a step melt residue formulation is used, and the plume migrates slightly but then stays in the southern hemisphere and moves along the boundary of the melt residue. In model SZ3 the temperature is slightly increased, which causes increased melt residue and slightly larger plume migration, but the plume remains in the southern hemisphere. Possibly the same process that promotes plume formation under the enriched southern crust also works to suppress plume migration out of the southern hemisphere. It is possible this can be overcome with sufficient melt residue, as we saw increased migration when we raised the temperature and had more melt residue, but we have not yet observed large-scale migration in our simulations when including an enriched southern crust. We also find that the melt formulation can affect the model behavior. In model SZ4 (Figure 3.6), the melt residue formulation is changed to a continuous function instead of a step function, which results in plume splitting instead of the small scale migration observed in models SZ2 and SZ3. While Šrámek and Zhong (2012) found plume migration did not depend strongly on the melt residue parameterization (step vs continuous, or the maximum viscosity increase), when an enriched southern crust is included the model behavior seems more dependent on the melt residue parameterization. Overall melting is highly temperature dependent, and small changes in temperature (including those cause by the heating from the enriched crust) can affect the simulation behavior.

Building on the benchmarking cases, we examined if any superplume migration could occur for the post-impact simulations which produced superplumes. We found that as in the benchmarking cases, no large scale plume migration occurred (Figure 3.7). While small scale migration can occur, the insulating effect of the enriched southern crust keeps upwellings focused in the southern hemisphere. For both continuous and step melt residue parameterization, plume splitting can occur, depending on the model parameters. Overall, our results indicate that it may be difficult for a plume formed under an enriched southern crust to migrate to the dichotomy boundary, as hypothesized in Section 3.2.

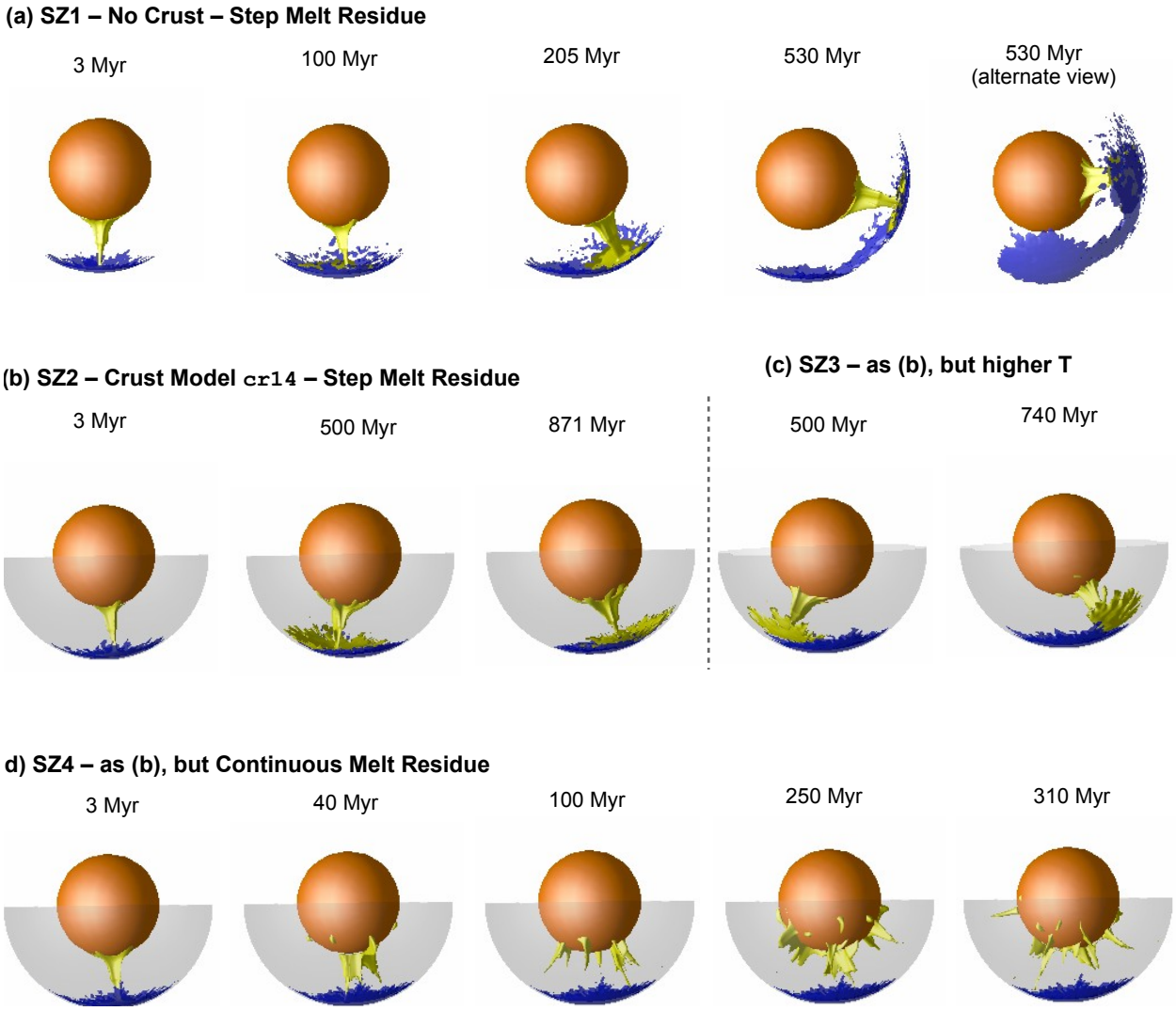

Figure 3.6: Example outcomes for plume migration benchmarking. Yellow contours show upwellings with residual temperatures of 50-90 K. Blue contours show regions with melt extraction of 5% (except in (c) where it is 10% for clarity). The grey contour shows the southern crust. Model parameters are similar to Šrámek and Zhong (2012). In (a), no crust is included and the plume migrates 90° in 530 Myr. In Model (b), a 50 km thick crust is included in the southern hemisphere, enriched by a factor of 4 relative to the mantle. A step function is used to treat viscous stiffening of regions where melt was extracted (viscosity is increased by a factor of 200 when melt extraction is $\geq 5\%$. Model (b) is similar to (c) but the mantle starts 50 K warmer. Model (d) is similar to (b) but uses a continuous function to describe viscous stiffening of melt residue from melt extraction.

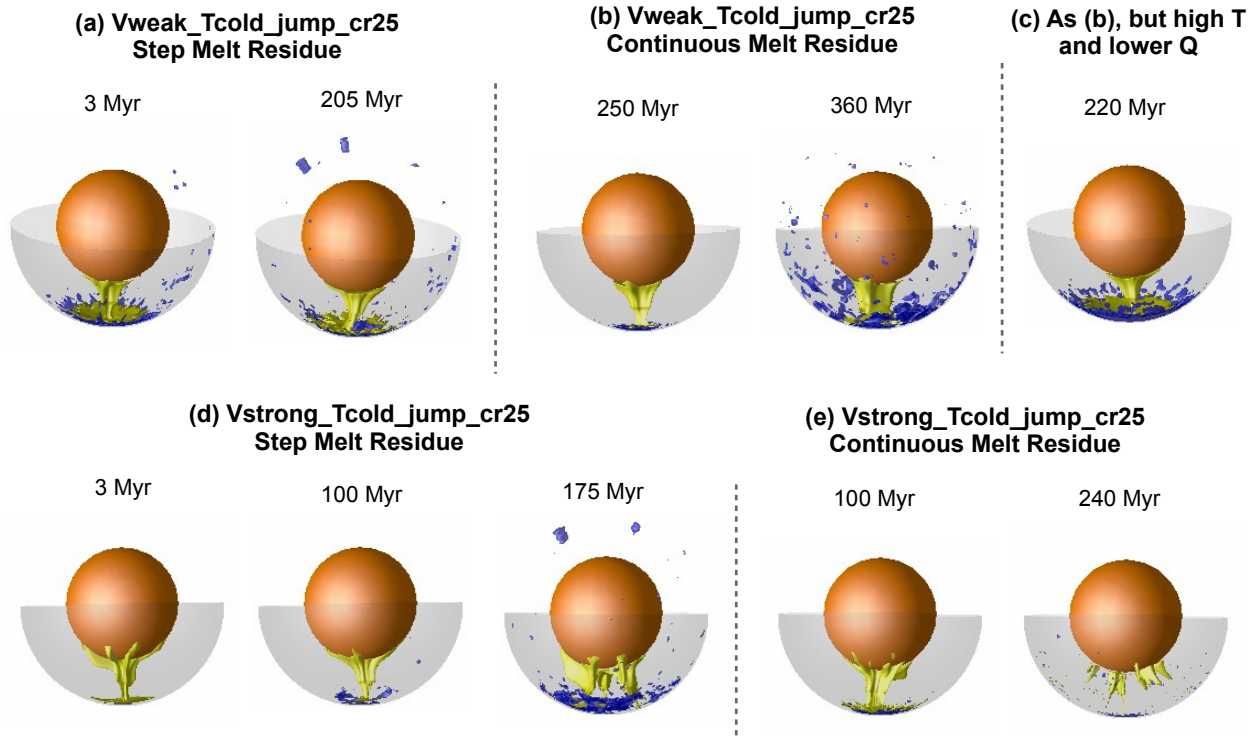

Figure 3.7: Example outcomes for superplume evolution simulations. Yellow contours show upwellings with residual temperatures of 50-90 K. Blue contours show regions with melt extraction of of 5%. The grey contour shows the enriched southern crust. No large scale plume migration occurs in these simulations, although plume splitting can occur depending on the model parameters.

3.4.3.2 Magnetic lineations

In addition to plume migration, we examine the effect of melt production on the expected distribution and polarity of remanent crustal magnetic signatures. In particular, we test the hypothesis discussed in Section 3.2 that the observed pattern lineations of reversing polarity in the remanent crustal magnetism data is due to melt/crust production spreading radially away from a superplume (Citron and Zhong, 2012).

To estimate the polarity of crustal magnetism produced from a superplume, we examine the spatial and temporal distribution of crust produced in the simulations from Section 3.4.3. Given a timescale of polarity reversal, we estimate the cumulative polarity of the remanent crustal magnetism by integrating the crust produced with a positive or negative polarity at each point on the surface over the course of the simulation. If at a given surface location an equal amount of crust is produced with both positive and negative polarity, then the cumulative polarity at that location will be zero. If more crust is produced with either a positive or negative polarity, then the cumulative polarity at that location will be positive

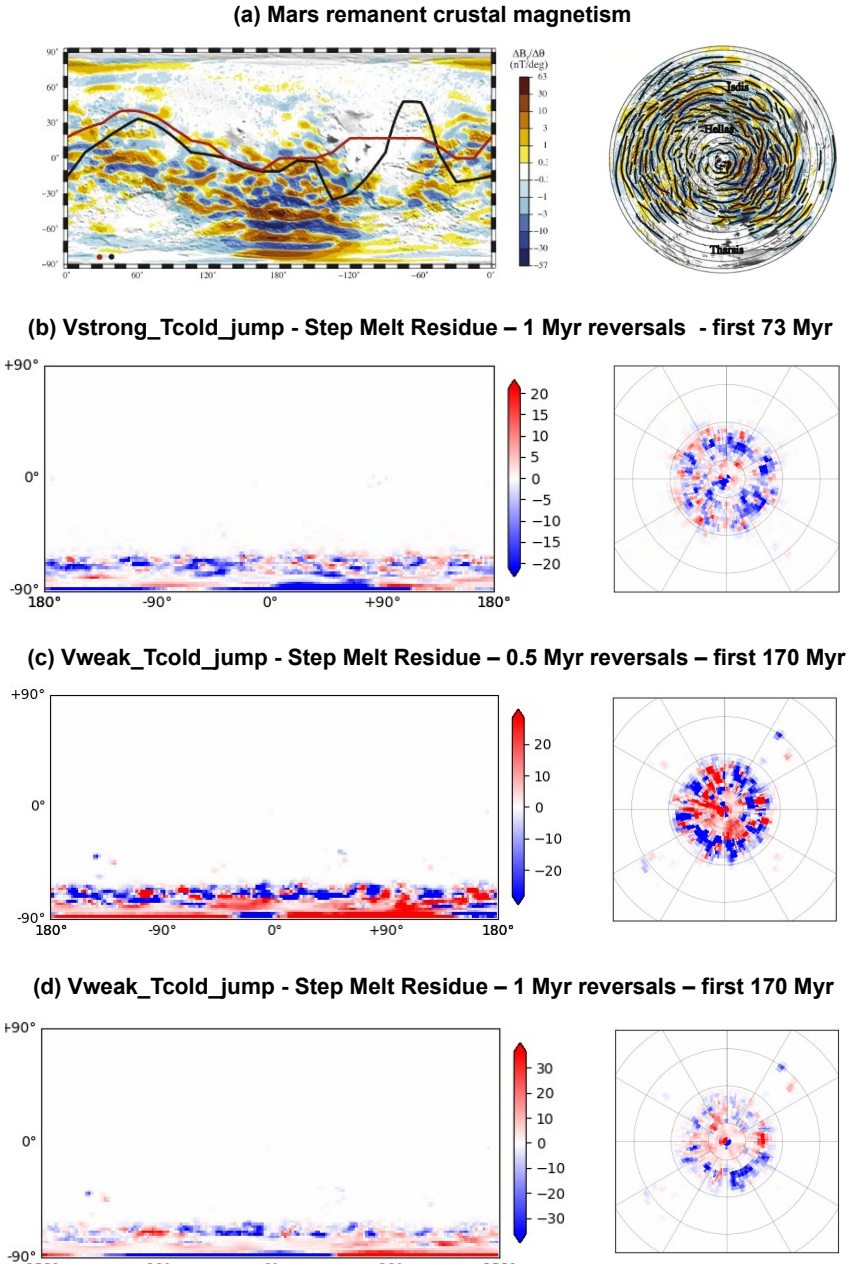

Figure 3.8: Polarization estimates for several example simulations. (a) Remanent crustal magnetization using data from Connerney et al. (2005) (plot adapted from Citron and Zhong (2012)). (b-d) Estimated remanent crustal magnetism polarization for several simulations (arbitary units). Polarization is the cumulative polarity of added crust, normalized to total crustal thickness. The timescale of polarity reversal is 0.5 or 1 Myr. Polar plots in (b-d) are centered on the south pole, with latitude marked 20° intervals from -80°S northward.

or negative, respectively. In order to emphasize locations where significant crust has been produced, we scale the cumulative polarity by the total thickness of crust added. While the timescale of polarity reversals on Earth is 0.05 to 1 Myr (not normally distributed) (Harland et al., 1990), the timescale of reversals on Mars is unconstrained. We examine timescales between 0.1 and 10s of Myr. The results are shown in Figure 3.8.

In general we were not able to reproduce the nearly global distribution of lineations observed on Mars (Figure 3.8). While some patterns resembling lineations are seen in our simulations, the locus of crust production did not spread much beyond 70°S. This does not support the hypothesis that lineations were produced from melt generated progressively further away from the superplume. It is possible that varying model parameters, such as the mantle temperature, melt model, or dehydration stiffening could result in melting that spreads further from the plume, however we did not observe such behavior. Another possibility for generating a varying locus of melt production is large scale migration of the superplume, however, as we observed in Section 3.4.3 the enriched crust in the southern hemisphere helps confine the superplume to the southern hemisphere. Overall while we are able to show that some lineations can be generated by superplume melting, we were unable to reproduce the global pattern of lineations observed on Mars.

3.5 Discussion

Our models necessarily used several simplifying assumptions and examined a limited parameter space. We could only explore a limited selection of mantle rheologies, initial temperature states, crust models, and melting parameterizations. Each of these can strongly affect the model outcome, but are largely unconstrained for early Mars. Full examination of these processes would require an unreasonable amount of computing power, so we attempted to examine a reasonable portion of the parameter space. While larger changes in bulk mantle properties are required to alter the global dynamics, small changes in mantle temperature or internal heat production can greatly affect the amount of melt production and the corresponding amount of melt residue. Using a different parameterization for dehydration stiffening of melt residue (*e.g.*, Plesa and Breuer, 2014; Fraeman and Korenaga, 2010; Ruedas et al., 2013b; Morschhauser et al., 2011) may affect plume migration and the distribution of melt production. We also used an anhydrous melt parameterization, based on the assumption that dehydration has a larger effect on the rheology (dehydration stiffening) than the melting curve. However, use of a hydrous melting parameterization (*e.g.*, Katz et al., 2003) may make it more difficult to re-melt dehydrated mantle, and could affect the corresponding spatial distribution of melt generated by a superplume. So while understanding the global dynamics requires examining end members of the range of plausible mantle properties, within each global convection state, the melting-induced dynamics and crust production can change a great deal depending on the melting model. Full examination of the required parameter space is therefore difficult given computational constraints.

In order to examine more first order controls on convection patterns, we also ignore more

complex processes that could affect the simulation dynamics. More complex models could include the effects of phase changes and a fully temperature and pressure dependent thermal diffusivity and expansivity, which can have an effect on Mars mantle convection (Ruedas et al., 2013a). We also did not account for delamination of the crust. A layered mantle with a higher density basal layer is also possible for Mars, but was not considered here.

Our examination of the magnetic lineations was also necessarily simplified. The lineations in the magnetic signatures observed at altitude may not represent the true distribution of magnetism in the crust. Extrapolating the magnetic field at altitude to the surface present a non-unique solution, and several types of patters of remanent crustal magnetization may be possible. The reversal rate is also unconstrained for Mars, and could vary with time. However, given the size of the lineations, a qualitative assessment of the feasibility of producing a compatible spatial distribution of melt should be possible.

3.6 Conclusions

We expanded on our work from Chapter 2 and examined the subsequent evolution of martian superplumes arising from impact-generated hemispherical differences in crustal thickness and composition. We were not able to support our hypothesis that early martian superplumes generated following a giant impact could migrate to form Tharsis on the dichotomy boundary, or would produce melting in a pattern similar to the distribution of magnetic lineations. We did support our conclusions from Chapter 2 and show that superplumes could form under a wider parameter space than we previously examined. However, we found that the insulating effect of the enriched southern crust worked as an opposing force against melt-residue induced plume migration, keeping the upwelling(s) focused in the southern hemisphere. Still, small-scale migration could occur, and depending on the melt parameterization, the superplume could split into multiple plumes, a possible mechanism to form multiple volcanic centers. It is possible that different model parameters could still result in superplume migration and Tharsis formation on the dichotomy boundary, however fine tuning model parameters to achieve such a result is ad hoc and not a general solution. Instead, Tharsis may have formed in-place due to a process such as edge-driven convection (Kiefer, 2005; Redmond and King, 2004; King and Redmond, 2005). For the formation of the magnetic lineations, the focusing of the upwellings under the south pole prevented the region of melt production to expand a significant distance from the plume center. Different melting models might produce a different distribution of melt production than found in our simulations, and can be the focus of future work. While melting and the corresponding melt residue can clearly influence plume migration and crust production, the link between early martian mantle convection and the formation of Tharsis and the magnetic lineations remains enigmatic.

3.7 Acknowledgements

This work was supported by NASA grant 80NSSC19K0545. We thank Mingming Li for providing the melting subroutines for CitcomS and for helpful discussions. This work used the Savio computational cluster resource provided by the Berkeley Research Computing program at the University of California, Berkeley, and resources of the National Energy Research Scientific Computing Center, a DOE Office of Science User Facility. CitcomS is available through the Computational Infrastructure for Geodynamics (geodynamics.org).

Chapter 4

A Giant Impact on Early Mars: High-Resolution Modeling with Material Strength

4.1 Summary

A giant impact is a compelling hypothesis for the origin of the Mars crustal dichotomy. A giant impact could explain the elliptical shape of the dichotomy boundary, and the bimodal difference in crustal thickness between the northern lowlands and southern highlands. However, impact models of dichotomy formation predict large variations in crustal thickness and annular thickening of the basin rim due to ejecta, which are both not observed on present-day Mars. We examine if the inclusion of material strength in giant impact models can result in a post-impact crustal thickness distribution more consistent with observations of Mars. In particular, we examine if impact models can result in the spatial distribution of sharp and gradual transitions in crustal thickness observed across various sections of the dichotomy boundary. We find that strength can play an important role in giant impact basin formation, however, our models do not result in crustal thickness distributions comparable to what is observed on Mars. An impact model fully consistent with the dichotomy boundary remains elusive.

4.2 Introduction

Mars is fundamentally divided into two hemispheres: the heavily cratered terrains of the southern highlands and the smooth plains of the northern lowlands. The boundary between these two provinces traces a stark difference in elevation and crustal thickness known as the martian crustal dichotomy (as discussed in Chapter 2; see Figure 2.1). The northern lowlands, also known as the Borealis basin, cover about a third of the Martian surface, but prior to the later formation of Tharsis could have covered 42% of the surface, corresponding

to an ellipse 10,600 km by 8,500 km (Andrews-Hanna et al., 2008). One leading theory of the formation of the Borealis basin (*i.e.*, formation of the crustal dichotomy) is a giant impact (*e.g.,* Wilhelms and Squyres, 1984), which could have stripped the crust in the present-day northern hemisphere, creating a vast impact basin. The hypothesis that the Borealis basin formed via giant impact early in Mars' history ($\sim$4.5 Ga) is supported by several lines of evidence. Most compelling is the elliptical shape of the dichotomy boundary (Andrews-Hanna et al., 2008), as shown in Figure 4.1a,b; while smaller impacts produce circular craters (even for oblique impacts), a giant impact would produce an elliptical basin due to the scale of the impact and the effects of planet curvature (Andrews-Hanna et al., 2008; Collins et al., 2011). An early giant impact >4.5 Ga is also supported by analysis of martian meteorites, based on both the melting history of the oldest martian mineral samples (Moser et al., 2019), and the abundances of highly siderophile elements in the martian mantle that suggests late accretion via a giant impact (Brasser and Mojzsis, 2017; Bottke and Andrews-Hanna, 2017). Furthermore, giant impacts were a common process in the late stages of planetary formation, making a giant impact on early Mars an expected outcome of its formation.

Although other mechanisms of dichotomy formation have been proposed (as discussed in Chapter 2), we focus on a giant impact in the northern hemisphere because the elliptical shape of the Borealis basin appears so compelling. Although the dichotomy boundary cannot be readily traced around the entire planet because Tharsis is superimposed on part of the dichotomy boundary, Andrews-Hanna et al. (2008) found that the likely sub-Tharsis path of the dichotomy would complete the elliptical shape of the basin. The bi-modal distribution of crustal thickness, and the relatively sharp transition in crustal thickness and topography across the dichotomy boundary has also been cited as evidence for a giant impact, because degree-1 convection is expected to produce a more gradual change in crustal thickness (Andrews-Hanna et al., 2008). Marinova et al. (2008) tested the impact hypothesis using smoothed particle hydrodynamic simulations of giant impacts on early Mars, finding that the elliptical Borealis basin could have formed from a giant impactor of diameter 1600-2700 km, impact at 6-10 km s^{-1} at an angle of 30-60°. Nimmo et al. (2008) also performed numerical simulations of a Borealis-scale impact, however the simulations were in 2D so were only able to reproduce the difference in crustal thickness caused by the impact (not the elliptical shape of the impact basin).

Despite the early success of impact simulations of dichotomy formation (*e.g.,* Marinova et al., 2008), there are two main uncertainties that we identify in reconciling giant impact simulations with the formation of the Borealis basin. First, the results of the simulations of Marinova et al. (2008, 2011) show large variations (up to a factor of 2) in crustal thickness produced by ejecta emplacement following the impact, including an increase in crustal thickness in the circum-basin rim, and an accumulation of ejecta downrange in oblique impacts. Such large variations in crustal thickness are not observed in the southern highlands (except when there is a clear impact basin or volcanic province). It is possible that the variations in crustal thickness are due to the low resolution of the Marinova et al. (2008) models, in which the crust is represented by only the outermost layer of SPH particles. Higher resolution simulations could test this by better resolving the post-impact distribution of crust

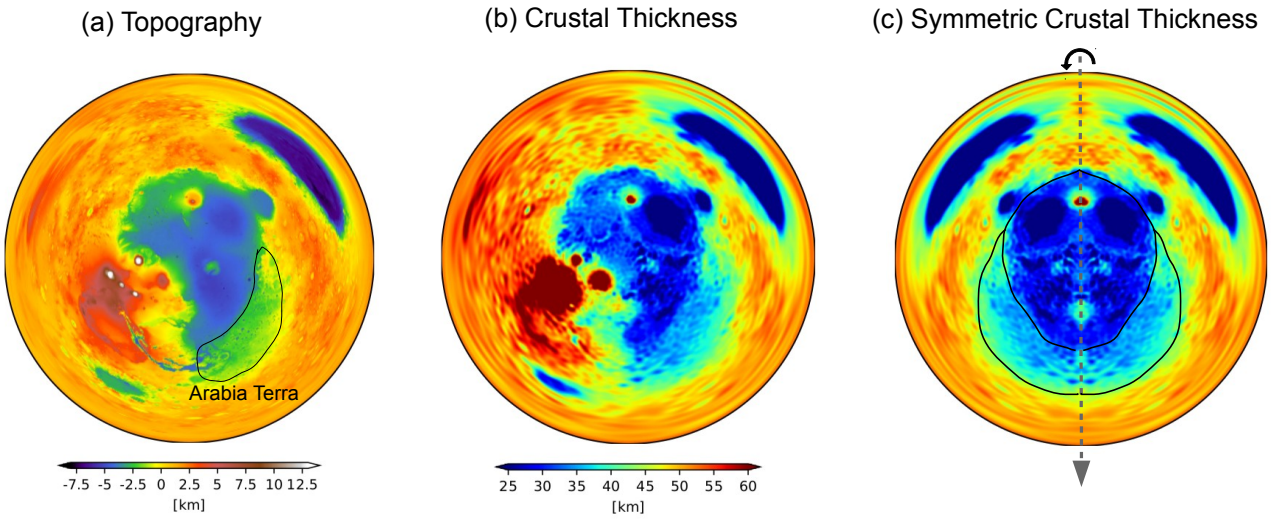

Figure 4.1: Topography and crustal thickness of the Borealis basin, and its hypothetical symmetry. (a,b) Mars topography (Smith et al., 2003) and crustal thickness (Genova et al., 2016) are projected in polar coordinates, centered on 67°N, 208°, the basin center from Andrews-Hanna et al. (2008). The Arabia Terra region is outlined in black. (c) A hypothetical symmetric crustal thickness model, constructed by making the image from (b) symmetric about the suspected impact plane (grey dashed line), so that the side to the left of the grey line (the side containing Tharsis) is removed and replaced with a mirror image of the crustal thickness distribution to the right of the grey line. This emphasizes the potential pre-Tharsis shape of the Borealis basin and its downrange rim (Arabia Terra), which are outlined in black; the mirror image also includes copies of the Hellas and Isidis basins, which should be ignored. The grey arrowhead points downrange of the proposed impact direction.

and ejecta. Alternatively, it may be possible that post-impact variations in crustal thickness are expected, and post-impact viscous relaxation and crustal flow (*e.g.,* Karimi et al., 2016) could have smoothed out impact-induced topography and crustal thickness variations.

The second uncertainty we identify regarding simulations of dichotomy formation via giant impact is the differences in the dichotomy transition observed at different portions of the dichotomy boundary; in some sections (such as south of Elysium or next to Isidis) the transition from low to high crustal thickness across the dichotomy boundary is quite sharp, however, the vast Arabia Terra segment of the dichotomy boundary displays a gradual change in crustal thickness. The anomalous slope of the dichotomy transition across Arabia Terra is likely a remnant of dichotomy formation (Nimmo, 2005) and not due to subsequent erosion (Evans et al., 2010). Andrews-Hanna et al. (2008) propose that Arabia Terra represents a partial multi-ring structure created during the giant impact and the post-impact modification of the impact basin. However, why a multi-ring structure would form only on a portion of

the impact basin rim is unclear. We hypothesize that Arabia Terra initially extended further west, underneath Tharsis, and is the downrange impact basin rim. Arabia Terra actually terminates at Tharsis, so it is conceivable that prior to Tharsis formation, the gradual slope of the dichotomy boundary of Arabia Terra continued westward until it was covered by Tharsis. Because inferring the pre-Tharsis dichotomy boundary beneath Tharsis is highly sensitive to model parameters, it is difficult to determine the true pre-Tharsis slope of the sub-Tharsis portion of the dichotomy boundary. However, an impact basin is expected to be roughly symmetric across the vector of the impact. A hypothetical extended pre-Tharsis dichotomy boundary, constructed by making martian crust symmetric about the impact plane (ignoring the Tharsis half) is shown in Figure 4.1c.

In the proposed pre-Tharsis crustal distribution of 4.1c, Arabia Terra is part of the downrange rim of the impact basin, which exhibits a more gradual transition in crustal thickness than the uprange portion of the rim. A more gradual slope of the downrange rim of a giant impact basin might be expected due to the dynamics of an oblique impact and post-impact modification. Smaller scale oblique impacts, including those expected to form elliptical craters on Mars, exhibit a sharper slope on the uprange rim than the downrange rim (Elbeshausen et al., 2013). This change in morphology accompanies the transition from circular to elliptical crater formation, which occurs for impacts below the elliptical crater threshold angle, which varies depending on the projectile size and velocity, and the target material properties (Elbeshausen et al., 2013). For smaller impacts (projectile diameters $<$10 km), the threshold angle could be $<15°$, but for larger impacts the projectile size and curvature of the planet can affect crater formation, and projectiles $>$1000 km in diameter could have elliptical threshold angles $>45°$ on Mars (Collins et al., 2011). The most likely impact angles for a giant impact on Mars (30-60°) could therefore form impact basins with morphologies similar to oblique impact craters, such as a sharper uprange rim and more gradual downrange rim, although the dynamics of post-impact modification and crater collapse could be different for giant impacts than for smaller, simple craters. Another possibility is that post-impact modification and crustal flow was enhanced downrange of the impact. Marinova et al. (2008, 2011) show that melt from Borealis-scale impacts is preferentially deposited downrange. This could create a hotter, weaker crust downrange of the impact amplifying post-impact crustal flow and modification of the downrange basin rim, resulting in the gradual crustal thickness transition of the Arabia Terra formation.

Although a giant impact is perhaps the most commonly accepted theory for the origin of the Borealis basin, no impact model has produced a post-impact crust distribution fully consistent with the Mars crustal dichotomy, for the reasons mentioned above; the two major uncertainties appear to be that the distribution of ejecta varies in thickness more than present-day crustal thickness variations in the southern highlands, and the impact basin rim displays variations in its slope that have not yet been reproduced in giant impact simulations. The main issues with prior simulations of a Borealis-scale impact are the resolution (the crust is only one SPH particle thick in the Marinova et al. (2008) simulations) and the lack of inclusion of material strength. While giant impacts are expected to occur in the gravity-regime of impact cratering, where strength should have limited effects, the inclusion

of strength may be necessary to resolve the effects of varying ejecta thickness and formation of the impact basin rim. Emsenhuber et al. (2018) recently modeled giant impacts on Mars with SPH including material strength, finding that inclusion of strength could have a substantial effect on the impact outcome. However, Emsenhuber et al. (2018) only modeled impacts of velocities 4 km s^{-1}, lower than the expected impact velocities of $6 - 15$ km s^{-1}, and on Mars-like bodies with relatively cold mantles (compared to the expected warm early mantle). Using a low impact velocity and a colder target would both amplify the importance of strength on the impact outcome, so it is still unclear how important strength is for a higher velocity giant impact on a Mars-like body with a warmer mantle. Although there have been other recent studies of giant Borealis-scale impacts on early Mars (*e.g.,* Hyodo et al., 2017), these studies have generally focused on determining if such impacts can produce sufficient debris to form the Martian moons, and do not examine the formation of the impact basin. However, detailed comparison of impact model outcomes, particularly with the inclusion of strength, with the crustal thickness distribution of Mars could better constrain the type of giant impact that could have formed the Borealis basin, in particular the impact size, velocity, and angle, and the pre- and post-impact thermal state of Mars and the impacting body. If Arabia Terra can be shown to represent part of the downrange rim of the impact basin, then detailed modeling could constrain the impact direction and the post-impact rotational state of Mars, potentially also resolving if the Borealis impact is the cause of Mars' relatively fast spin rate (*e.g.,* Craddock, 2011).

Accordingly, in order to determine if the structure of the Borealis basin is consistent with a giant impact, and to better constrain the expected impact parameters, we conduct a suite of high resolution simulations of giant impacts on early Mars. We use adaptive mesh refinement to better resolve the post-impact distribution of crust, and include the effects of material strength to quantify its importance in producing impact models consistent with the shape and structure of the Borealis basin.

4.3 Methods

We conduct a suite of high-resolution simulations of Borealis-scale giant impacts onto a Mars-like body, including the effects of material strength. We use the numerical hydrocode CTH (version 11.1) (McGlaun et al., 1990; Schmitt et al., 2015), which is widely used to model planetary impacts (*e.g.,* Leinhardt and Stewart, 2009), and has also been used to model giant impacts (Canup et al., 2013). All simulations are conducted in 3D (to model oblique impacts), using both self-gravity and adaptive mesh refinement (Crawford, 1999).

Adaptive mesh refinement allows us to increase the resolution in regions of interest and decrease the resolution in other portions of the domain, allowing us a maximum resolution otherwise computationally infeasible if applied to the entire simulation domain. We increase the resolution in regions where there is crustal material, allowing us to better model the final crustal thickness distribution (the most important output of our simulations). We also increase refinement (at various levels) of high-density material and material interfaces, but

decrease the refinement further away from the planetary body. The maximum resolution achieved is a cell size of 25 km.

Mars is modeled as a spherical body with a core, mantle, and crust, while the impacting body consists of a core and mantle (no crust). We use the M-ANEOS equation of state (Melosh, 2007), a molecular version of the the ANEOS equation of state (Thompson and Lauson, 1972) that better models impact vaporization. For mantle material, we use M-ANEOS parameters for dunite from Canup et al. (2013). We model the crust as basalt using the M-ANEOS parameters from Pierazzo et al. (2005). The iron core is modeled using the ANEOS parameters for iron included in CTH.

To model the effect of strength, we use the geological yield surface model (GEO model) included in CTH (Schmitt et al., 2015). The GEO model parameterizes the material strength as a pressure-dependent yield surface, including the effect of thermal softening. The yield surface has a shear strength of Y_0 at zero pressure, which increases with pressure to a maximum value of Y_M (the yield strength at high pressure), with a slope equal to the coefficient of internal friction. We use the same GEO model parameters as the 'strong' GEO model from Leinhardt and Stewart (2009): Y_0=0.1 MPa and Y_M=3.5 GPa, with a Poisson's ratio of 0.3 and coefficient of internal friction of 1. The parameters for the strong GEO model are meant to represent intact rock, which typically have a dynamic shear strength of a few GPa. We use the same strength parameters for both the basalt crust and the dunite mantle. The iron core is treated as strengthless. As in Emsenhuber et al. (2018), we neglect the effects of tensile strength. We also conduct some simulations without any strength model to compare the effect of using strength versus using fluid bodies (as done in most previous SPH simulations).

The Mars-like target has a planetary radius of 3400 km and core radius of 1750 km, corresponding to a planet 30% iron by mass. We use a crust with an initial thickness of 120 km. While this is nearly twice as large as the thickness of the crust under the southern highlands, it is a necessary approximation in order to resolve the crust with 4-5 cells at maximum resolution. This is still a somewhat low resolution of the crust (although four times the resolution of Marinova et al. (2008), which used a 140 km thick crust), but allows us to complete a suite of exploratory simulations with sufficient computational time; future work will test the effects of using a higher resolution and thinner crust. We set initial temperature to 1900 K at the center of the core (0 km), 1680 K at the core-mantle boundary (1680 km), 1500 K at the base of the lithosphere (3250 km), 980 K at the base of the crust (3312 km), and 220 K at the surface (3400 km), interpolating linearly between those points. This is based roughly on the temperatures used by Emsenhuber et al. (2018), temperature profiles from parameterized models of Martian mantle convection (Hauck and Phillips, 2002), and estimated adiabatic temperature gradients through the core and mantle given an initially sub-solidus upper mantle.

The impacting body is given a radius (R_i) of 1000 or 1300 km, with a core radius set to yield a planetary body 30% iron and 70% dunite by mass. An impactor radius of 1000-1300 km is within the size range examined by other impact models (Marinova et al., 2008; Emsenhuber et al., 2018), and Brasser and Mojzsis (2017) suggest an impactor with radius

>600 km is necessary explain the late addition of highly siderophile elements to the martian mantle. Marinova et al. (2008) find that the Mars crustal dichotomy is best reproduced in SPH simulations by an impactor 800-1350km in radius with a velocity of 6-10 km s^{-1} and an impact angle of 30-60°. Accordingly, we model impacts with velocities (v_i) of 6, 10, or 15 km s^{-1}, corresponding to 1.2, 2, and 3 times the mutual escape velocity (v_{esc} ≈5 km s^{-1}), and impact angles (θ_i) between 30-60° (defined such that 90° is head-on). Most impacts are expected to occur within this impact angle range, with the most likely impact angle being 45° and hit-and-run type collisions having more oblique impact angles $\lesssim$30°. The initial temperature profile of the impactor is given by a linear interpolation between a temperature of 1700 K at the center (0 km), 1500 K at the core-mantle boundary (535 or 700 km for R_i= 1000 or 1300 km, respectively), 1480 K beneath the lithosphere (900 or 1200 km), and 220 K at the surface (1000 or 1300 km), based roughly on the temperatures used by Emsenhuber et al. (2018) and estimated adiabatic temperature gradients through the core and mantle.

Overall, we conduct a suite of 30 simulations considering impacting bodies with a radius (R_i) of 1000 or 1300 km, impact velocity (v_i) of 6, 10, or 15 km s^{-1}, and impact angle (θ_i) of 30, 37.5, 45, 52.5, or 60°. For R_i=1000 km and v_i=6 and 10 km s^{-1}, we conduct two additional simulations without material strength, and two additional simulations with an undifferentiated impactor (100% dunite), to test these effects, for a total of 34 simulations.

4.4 Results

Snapshots from representative CTH simulations are shown in Figures 4.2 and 4.3. The simulation outcome varies greatly depending on the impact parameters. Grazing impacts strip a small fraction of the crust and a large portion of the impactor escapes. More incident impacts cause more disruption of the crust and planetary target (Figure 4.2c). During these impacts the mantle can rebound hundreds of km beyond the original planetary radius. Impactors with high velocity cause more disruption of the planetary target (Figure 4.3b), and impactors that are too large can cause catastrophic disruption of the planet inconsistent with dichotomy formation (Figure 4.3c). An undifferentiated impactor results in less target disruption (Figure 4.3d), due to the lower impact energy (compared to a differentiated impactor with the same radius).

We compare the final crustal thickness distributions from our CTH simulations with the present-day estimated crustal thickness of Mars (Figures 4.4 and 4.5). No simulation can reproduce the present crustal thickness distribution observed on Mars, but our simulations highlight several features relevant to further study of an impact origin of the Borealis basin.

We find that impacts can produce a large amount of ejecta, resulting in a highly varied final crustal thickness. Thickening in the rim of the impact basins is a common result in the CTH simulations, which contrasts with the lack of such a rim observed on Mars. Depending on the impact parameters, significant downrange souring can occur (*e.g.*, Figure 4.4c. This is similar to what is seen in some of the simulations from Marinova et al. (2008, 2011). However, no such feature is readily observed on Mars. An undifferentiated impactor results in much

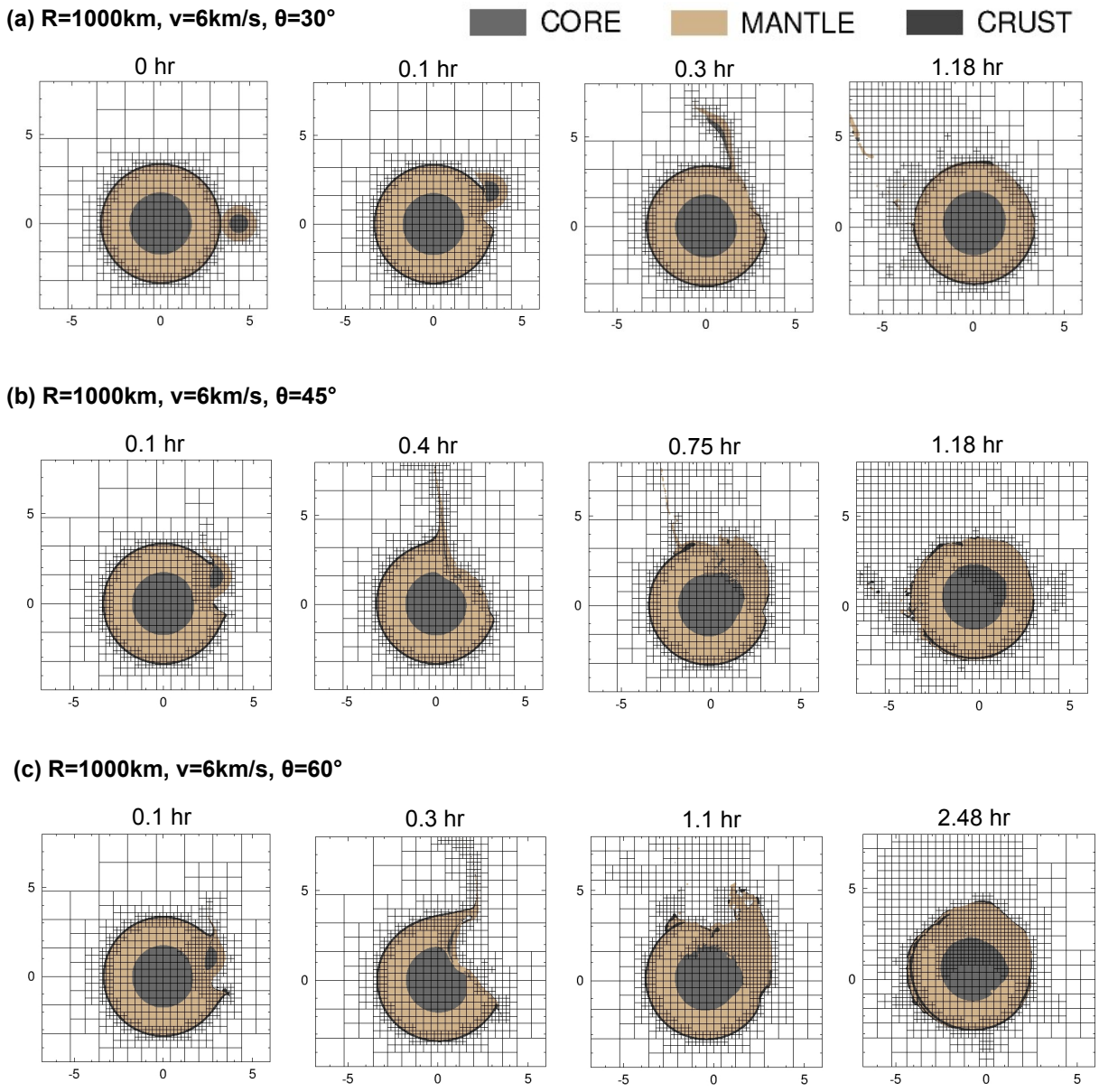

Figure 4.2: Example CTH simulation outcomes for varying impact angle. Each snapshot shows a 2D slice of the distribution of materials (core, mantle, and crust). The three simulations have $R_i = 1000$ km, $v_i = 6$ km s^{-1}, and $\theta = 30$, 45, or 60 °. Axis distance units are in 10^6 m. Black lines delineate the adaptive mesh refinement blocks. The true resolution is 8x smaller than each block (black square), because each block is subdivided into 8x8x8 cells (not shown).

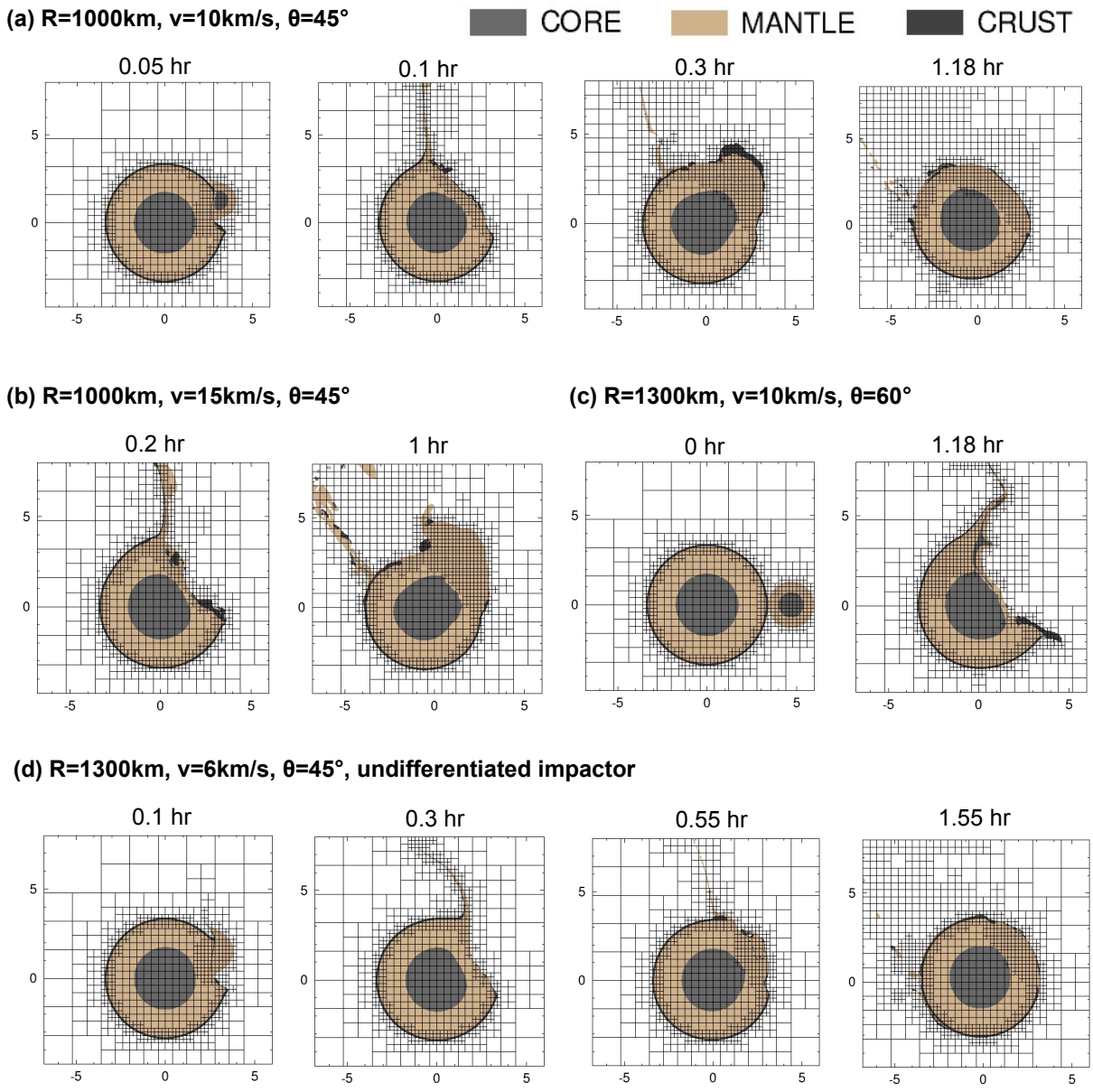

Figure 4.3: Example CTH simulation outcomes for varying impact parameters. (a) A simulation similar to that in Figure 4.2 but with a higher impact velocity (10 km s^{-1}). (b) Catastrophic collision caused by high impact velocity. (c) Extremely catastrophic collision caused by large projectile radius (1300 km) and more incident impact angle (60°). (d) Impact of an undifferentiated body, which causes less disruption compared to the impact by a differentiated body with the same impact parameters (Figure 4.2b).

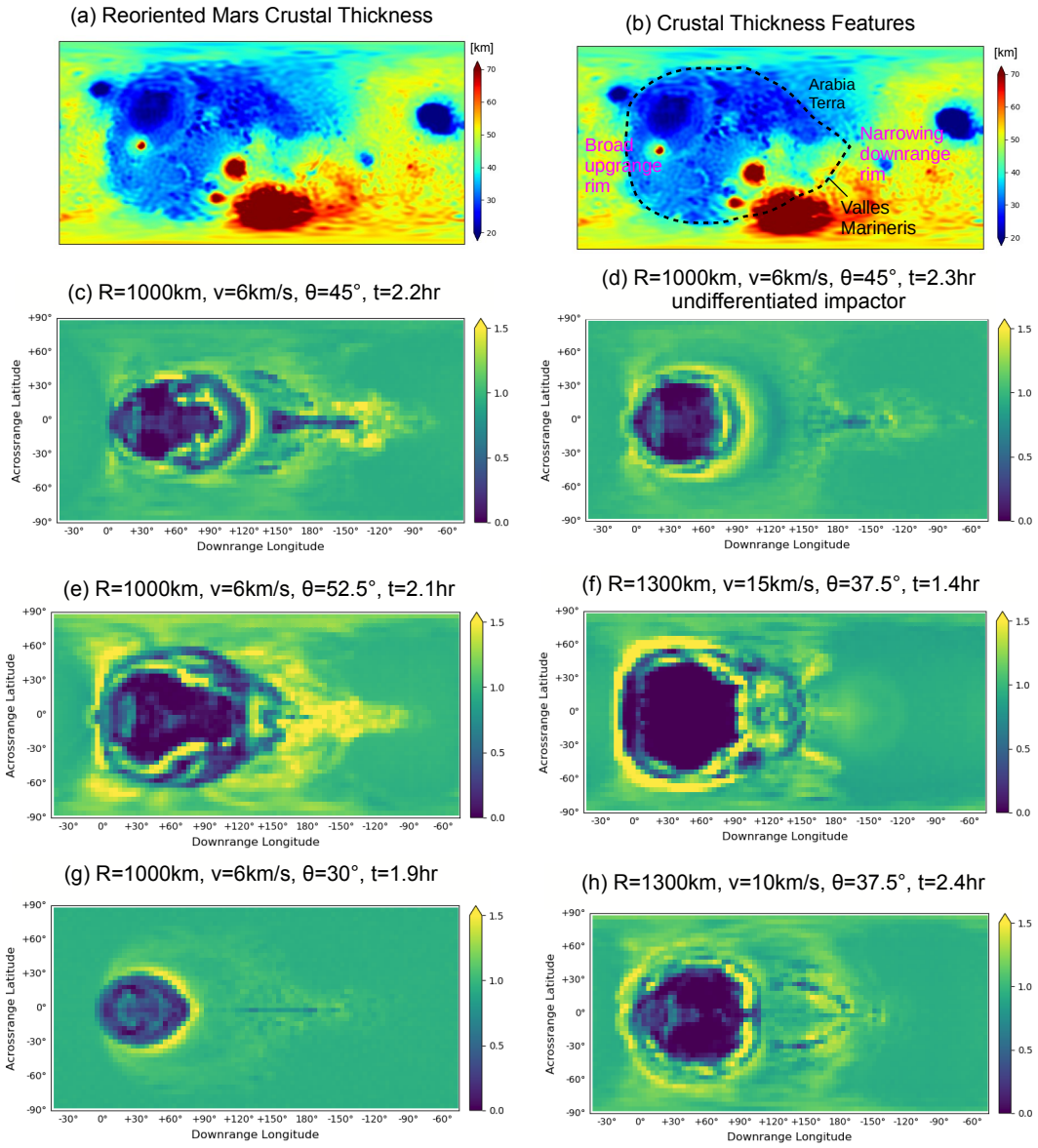

Figure 4.4: Crustal thickness outcomes for CTH simulations. (a) Present-day Mars crustal thickness (Genova et al., 2016), reoriented in the proposed uprange/downrange direction. (b) Crustal thickness with labels for the proposed broad upgrange rim and narrow downrange rim. The proposed rim cuts through Valles Marineris canyon, which is suggested to orient along the buried dichotomy boundary SE of Tharsis cite. (c-h) Final crustal thickness distributions of several example CTH simulations. Crustal thickness is normalized to the initial uniform thickness (120 km). Downrange longitude is distance in the impact direction; the impactor first contacts the target at 0°.

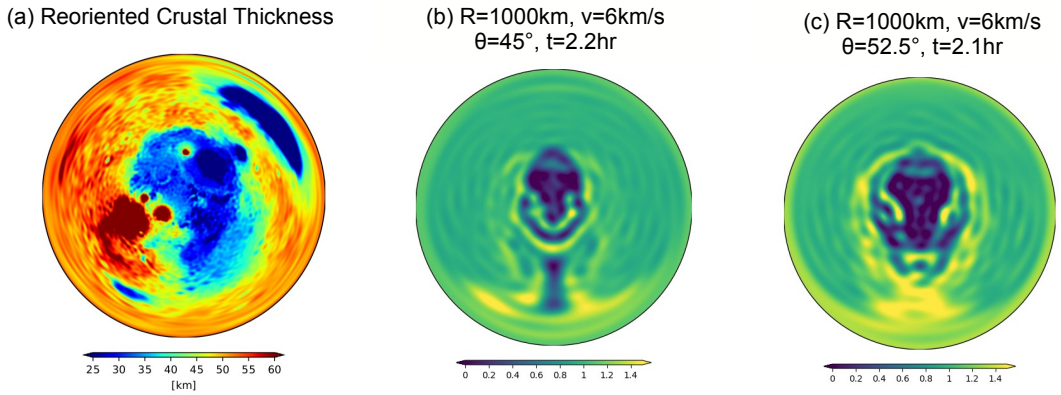

Figure 4.5: Polar plots of example CTH simulations. A polar view of the present-day crustal thickness (a) is comapred to the final normalized crustal thickness distribution of two CTH simulations.

less downrange scouring (Figure 4.4d) and smoother distribution of ejecta. However, the undifferentiated impactor still results in unrealistic annular thickening of the impact basin rim.

In Figure 4.4b, we identify some features related to Borealis basin formation to compare with the simulation outcomes. We propose the Borealis basin contains a broad uprange rim, and a narrow downrange rim. Such a feature identified in some impact simulations, such as Figures 4.4e and f. The 1000 km, 6 km/s, 52.5° impact Figure 4.4e has an outer rim that roughly corresponds to the proposed rim outlined in Figure 4.4b, however, the CTH simulation shows several crustal blocks that have slumped into the impact basin, in addition to a large amount of downrange ejecta, both features not observed on Mars. Some CTH simulations result in a broader downrange rim and a narrower uprange rim (*e.g.*, Figure 4.4h), suggesting our proposed uprange/downrange rims could be incorrect. We had also proposed Arabia Terra was a result of a more gradual uprange rim crustal thickness transition (Figure 4.1). However, this was not observed in our simulations. Although some simulations (*e.g.*, Figure 4.4c) resulted in a partial multi-ring structure in the uprange direction, the geometry of the crustal thickness transition was not comparable to the observed crustal thickness transition across Arabia Terra (Figure 4.5).

4.5 Discussion

While our results did not reproduce the crustal dichotomy, we have demonstrated the importance of including material strength when modeling dichotomy formation. Prior work (*e.g.* Marinova et al., 2008) operated under the assumption that a Borealis-scale impact would be in the gravity regime, where crater formation is dominated by gravitational stresses instead of material strength (Melosh, 2007). The transition from the strength regime to the gravity

regime is expected to occur at 10 km on Mars, using the scaling from Melosh (2007). Hence, neglecting material strength is a common practice when modeling giant impacts on Mars and other planetary bodies. However, as shown in Emsenhuber et al. (2018), material strength can be an important factor for Borealis-scale impacts. However, Emsenhuber et al. (2018) uses a lower impact velocity and colder projectile and target than Marinova et al. (2008), both assumptions that would enhance the effects of material strength. Here we show that for higher impact velocities material strength still has an important effect on the simulation outcome.

We find that the inclusion of material strength results in a smaller impact basin compared to a pure fluid approximation. Prior work that relied on the fluid approximation may underestimate the size of impact necessary to form the Mars crustal dichotomy. Material strength also affects the final crater shape, and the results of our simulations (Figure 4.4) produce different crustal structures than those resulting from purely hydrodynamic models (Marinova et al., 2011). Though not examined here, the amount and distribution of impact ejecta is also likely affected by material strength, an important consideration when constraining the types of giant impacts that could have generated a debris disk within the mass constrain necessary to form the martian moons (*e.g.*, Citron et al., 2015; Hyodo et al., 2017; Canup and Salmon, 2018).

In addition to the inclusion of a material strength model, the type of strength model, and the model parameters, can strongly influence the outcome of the simulation. Due to computational constraints, we examined only one strength model, but in preliminary work (not shown) we found that using different strength models or varying the yield strength resulted in different basin structures. However, how material strength operates on the planetary scales necessary to model large impact basins is not well understood. Various strength models have been used to model impacts on planetary surfaces (*e.g.*, Senft and Stewart, 2007; Collins et al., 2004). While these strength models have been effective at modeling small to moderate sized impact craters (*e.g.*, Davison et al., 2011; Senft and Stewart, 2008), in addition to lunar impact basins 100s of km in diameter (Johnson et al., 2016; Schultz and Crawford, 2016), few studies have incorporated strength models into simulations of larger basin forming impacts (*e.g.*, Ivanov et al., 2010; Emsenhuber et al., 2018). Because of our lack of understanding at the material properties under the conditions expected during giant impacts, it is unclear how well material strength models translate to accurately modeling material behavior during giant impact basin forming events. For this reason in this work we used a simple strength model (the GEO strength model included in CTH) to examine the effect of including a high material yield strength. However, due to the uncertainty in which material strength model and parameters are most applicable during giant impacts, a comprehensive study of basin formation partially becomes a search to determine which strength model type and parameters can produce a reasonable result, vastly increasing the required parameter space to examine and the required computational time. However, improvements are being made in constructing strength models that may be more applicable to giant impacts (*e.g.*, Elbeshausen and Melosh, 2018), which may increase our ability to more accurately model large impact basin formation.

It is also possible that a comprehensive model of impact basin formation must include not just a realistic strength model, but full consideration of post-impact secular crustal flow and viscous relaxation. Annular thickening of the impact basin rim and variations in downrange crustal thickness from ejecta emplacement may be expected results of giant impacts regardless of the strength model used. If that is the case, post-impact modification processes would be required to explain the relatively smooth crustal thickness distribution of the martian highlands. Viscoelastic relaxation can modify impact basins on planetary bodies, affecting the final crustal thickness distribution (Mohit and Phillips, 2007; Freed et al., 2014; Karimi et al., 2016), and moderate lower-crustal flow may have occurred along sections of the Mars dichotomy boundary (Nimmo, 2005). Relaxation of topography and crustal flow might explain how variations in crustal thickness caused by ejecta emplacement could have disappeared over time. However, if the relaxation of topography was significant enough to have erased the large variations in crustal thickness suggest by impact simulations, then it should have also reduced the sharp gradients in crustal thickness observed along sections of the dichotomy. One explanation might be that viscous relaxation is greater on the downrange rim of the impact basin and where the ejecta is deposited, as suggested by impact simulations (Marinova et al., 2011). Preferential deposition of heat downrange could result in enhanced post-impact crustal flow of the downrange rim and ejecta, reducing topography caused by ejecta emplacement and producing a smoother transition in crustal thickness across the downrange rim. If Arabia Terra is a section of the downrange rim of a Borealis impact, enhanced crustal flow due to downrange heat deposition and melting might offer an explanation for the gradual change in crustal thickness across the Arabia Terra section of the dichotomy boundary in comparison to the sections south of Elysium (the proposed uprange direction).

4.6 Conclusions

Modeling an impact origin of the Mars crustal dichotomy remains a challenge. Our results indicate that material strength can have a strong effect on impact basin formation during a giant impact, but no simulation in the limited parameter space we explored was able to reproduce the crustal structure of the Mars dichotomy. It is possible that impact modeling alone might be able to reproduce Mars' crustal structure by varying some combination of the model resolution, equation of state, strength model, projectile composition (differentiation), and initial thermal profiles of the projectile and target. However, it is also possible that the crustal structure observed on Mars is the result of post-impact modification from viscous relaxation and crustal flow, and such processes must be be coupled to the end state of impact models. While an impact origin of the crustal dichotomy remains a compelling hypothesis, further modeling is required to fully explain Mars' observed crustal thickness distribution.

4.7 Acknowledgements

This work was supported by NASA grant 80NSSC19K054. Computational resources supporting this work were provided by the NASA High-End Computing (HEC) Program through the NASA Advanced Supercomputing (NAS) Division at Ames Research Center. The CTH hydrocode is developed at Sandia National Laboratories.

Chapter 5

Early Martian Oceans: Geophysical Constraints from Shoreline Deformation Models

This chapter is adapted with substantial changes and additions from:

> Citron, R. I., Manga, M., and Hemingway, D. J. (2018), "Timing of oceans on Mars from shoreline deformation." *Nature*, 555.7698, 643.

5.1 Summary

Widespread evidence points to the existence of an ancient Martian ocean. Perhaps most compelling are the geological contacts lining the northern plains hypothesized to represent paleo-shorelines. However, the shorelines fail to follow an equipotential, which has been used to challenge the notion of their formation via (and the existence of) an early ocean. The shorelines' deviation from a constant elevation can be explained by true polar wander occurring after the formation of Tharsis, a volcanic province that dominates the gravity and topography of Mars. However, surface loading from the oceans can only drive polar wander if Tharsis formed far from the equator, and most evidence indicates Tharsis formed near the equator, meaning there is no current explanation for the shorelines' deviation from an equipotential that is consistent with our geophysical understanding of Mars. Here we show that variations in shoreline topography can be explained by deformation due to the emplacement of Tharsis. We find the shorelines must have formed prior to and during the emplacement of Tharsis, instead of after Tharsis as previously assumed. Our results indicate that oceans on Mars formed early, concurrent with the valley networks, and point to a close relationship between the evolution of oceans on Mars and the initiation and decline of Tharsis volcanism, with broad implications for the geology, hydrological cycle, and climate of early Mars.

5.2 Introduction

5.2.1 The Mars Ocean Hypothesis

Whether or not Mars once hosted ancient oceans is the subject of much debate. While it is likely that liquid water flowed on Mars' surface 3-4 billion years ago, as evidenced by valley networks (ancient river channels), deltas, alluvial fans, outflow channels, and lakes (Di Achille and Hynek, 2010; Kite, 2019), the duration of warm climates on early Mars and if ancient oceans were possible is more controversial.

The main evidence for early Martian oceans is geological, including hypothetical shorelines, stepped deltas, and tsunami deposits, which line the northern lowlands basin, the proposed site of an ancient ocean (Baker et al., 1991; Parker et al., 1989, 1993; Head et al., 1999; Di Achille and Hynek, 2010; Clifford and Parker, 2001; Carr and Head, 2003b; Rodriguez et al., 2016). Many of these features date from the early Noachian to early Hesperian (3.6-4.1 Ga). Hypothetical shorelines are perhaps the most prominent line of evidence for early Martian oceans, and will be described in more detail below. Deltas are also significant, because the morphologies of some deltas indicate that rivers drained into a standing body of water occupying the northern plains. Tsunami deposits (Rodriguez et al., 2016; Costard et al., 2017) further suggest that the northern plains once supported an ocean. Vast outflow channels on the upper slopes of the northern lowlands are a potential source of catastrophic flooding that could have filled the lowlands with water, and several other lines of evidence, such as crater morphology, have been used to suggest an aqueous origin for some of the northern plains units. However, given the age of the geological features such as shorelines, it is difficult to conclusively prove the existence of an ocean.

The main arguments against an ocean are primarily based on atmospheric modeling, geochemistry, geology, and water volume estimates. From an atmospheric modeling perspective, it is difficult to explain how Mars could have been warm enough early in its history to support such an ocean (Wordsworth, 2016), although this is debated (Ramirez and Craddock, 2018). However, while it may be difficult to support a persistently warm early Martian climate, it is possible that Mars could have experienced periods of transient warming (Wordsworth et al., 2017; Halevy and Head, 2014). From a geochemical perspective, there is a notable lack of carbonate deposits in the northern hemisphere (Pan et al., 2017), whereas one might expected widespread carbonates to exist if an ocean persisted for a significant amount of time. However, it has been proposed that an ocean could exist in periods of enhanced volcanic outgassing, which could inhibit carbonate production (Halevy et al., 2007; Halevy and Schrag, 2009). Still, it is possible that ancient oceans could have existed intermittently, during episodically warm climates, or that some piece of the early Mars climate puzzle is missing, and the geological evidence for an early Martian ocean cannot be ignored. Geological arguments against an ocean mainly involve disputing the geological arguments for oceans. For example, the interpretation of geological contacts as ocean shorelines has been disputed (*e.g.,* Sholes et al., 2019). Additionally, to circumvent the warm Mars suggested by valley networks carved by rainfall, several studies have suggested the valley networks could have

been carved by subglacial flow (*e.g.*, Carr and Head, 2003a). Finally, it has been suggested that the volume of water required to fill the hypothesized oceans is too great, because it would not have been able to escape over the last >3.5 Gyr (Carr and Head, 2015). However, it is suggested that a large portion of water can be sequestered into the cryosphere (Weiss and Head, 2017) and crust (Mustard, 2019), and more efficient mechanisms of atmospheric escape have been proposed (Shaposhnikov et al., 2019).

The early Mars ocean hypothesis has prompted healthy debate (*e.g.,* Wordsworth et al., 2018), and many lines of evidence for and against oceans can be discussed in great detail. Here, we focus on one of the earliest and arguably most significant lines of evidence for oceans on Mars: paleo-shorelines.

5.2.2 Mars Shorelines

One of the most compelling and controversial lines of evidence for early Martian oceans are geological contacts lining the northern plains for thousands of kilometers, which have been interpreted as paleo-shorelines (Parker et al., 1989, 1993; Head et al., 1999; Clifford and Parker, 2001; Carr and Head, 2003b). Although the interpretation of these geological contacts as paleo-shorelines is hypothetical, we will henceforth refer to them as shorelines. The shorelines are not purely wave-cut shorelines in the classical sense, but trace a range of geomorphological features suggesting the shorelines represent the boundary of an ancient ocean. The two most prominent shorelines are the Arabia shoreline and the Deuteronilus shoreline (Contacts 1 and 2, respectively, in Parker et al. (1989, 1993), where they were first identified in Viking Orbiter images). The Deuteronilus shoreline contains an isolated segment lining the Isidis basin, which we refer to here as the Isidis shoreline.

The Arabia shoreline is one of the oldest shorelines identified on Mars. It roughly follows the dichotomy boundary, enclosing nearly the entirety of the northern plains. Its age is perhaps best estimated from its superposition over large impact basins; based on the Arabia shoreline tracing the rim of the Isidis basin, we can constrain its age to < 3.9 Ga (based on the age of Isidis from Robbins et al. (2013)). Classification of the Arabia contact as a shoreline is based on several erosional features, such as cliffs, strandlines, and changes in slope along the fretted terrain of the dichotomy boundary. Surprisingly few studies have reexamined these features using more recent high-resolution data; a recent study by Sholes et al. (2019) suggests that these erosional features may not be coastal, however, identification of shoreline features in orbital imagery is notoriously difficult (Clifford and Parker, 2001), particularly if the shoreline is 3.9 Ga. Perhaps the most compelling evidence for the interpretation of the Arabia contact as a shoreline is its coincidence with deltas and Valley Network termini. It has been noted that many valley networks terminate at the Arabia shoreline (Parker et al., 1993; Chan et al., 2018), which would be expected if the valley networks were carved by rivers that drained into an ocean. Many deltas are also found along the Arabia shoreline, and some of these deltas have notable stepped fans, which is expected if the deltas were created by drainage into a standing body of water (*e.g.*, Fawdon et al., 2018).

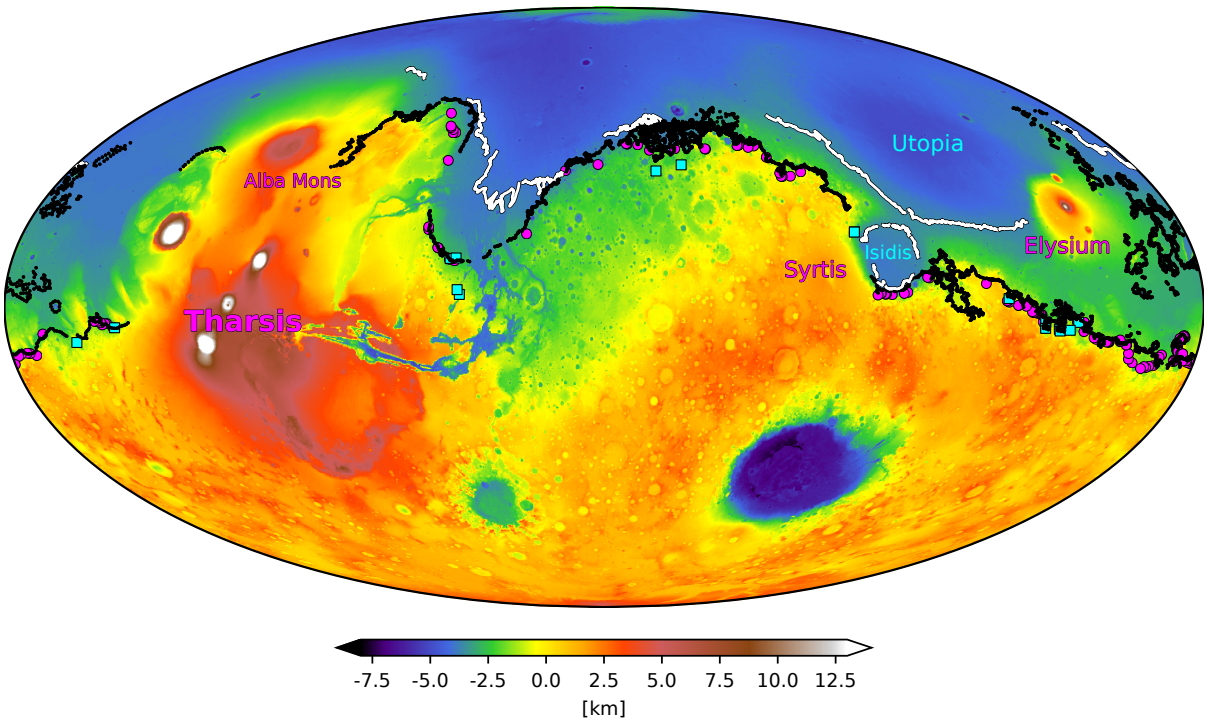

Figure 5.1: Map of Mars topography and shoreline locations. The Arabia shoreline is in black and the Deuteronilus and Isidis shorelines are in white. Valley network termini are plotted as magenta circles, using the "high confidence VN termini" data from (Chan et al., 2018). Delta locations are plotted as cyan squares, using the deltas classified as 'open' (draining into the northern plains) from Di Achille and Hynek (2010). Volcanic centers and basins discussed in the text labeled in cyan and magenta, respectively. The Arabia shoreline data is from (Clifford and Parker, 2001), and the Deuteronilus and Isidis shoreline data is from (Ivanov et al., 2017). Topography is from gridded MOLA data (Smith et al., 2003).

The Deuteronilus shoreline is younger and more prominent than the Arabia shoreline, and was recently remapped by Ivanov et al. (2017) and dated to 3.6 Ga. Located interior of the dichotomy boundary, the Deuteronilus shoreline traces the Vastitas Borealis Formation (VBF), a vast plains unit commonly interpreted as deposited by a body of water or ice (Ivanov et al., 2017). It has been suggested that the emplacement of the VBF and Deuteronilus shoreline coincides with catastrophic flooding that could have carved Mars' prominent outflow channels and inundated the northern plains with water (Carr and Head, 2003b). The Deuteronilus contact is much better defined than the Arabia shoreline, and can be identified by a sharp change in thermal inertia across the contact, consistent with the material interior of the shoreline being sedimentary in nature (Ivanov et al., 2017). The boundary of the Deuteronilus shoreline contains several erosional features such as lobes, ridges, and thumbprint terrain. However, it is suggested that these features do not represent

a wave-cut shoreline, but deposits of a muddy layer at the base of a frozen layer of ice, remnants of a past ocean. The features associated with the Deuteronilus shoreline (the edge of the VBF) are remarkably consistent along the extent of the shoreline (even for segments on opposite sides of the northern plains). The Isidis shoreline is morphologically similar to the Deuteronilus shoreline, but is separated by the topographic rise of Isidis' northeast rim. The Isidis shoreline is also dated to 3.5 Ga (Ivanov et al., 2017), slightly younger than Deuteronilus.

Although the Arabia and Deuteronilus shorelines display several morphologies indicative of an ocean, the shorelines display long-wavelength deviations in elevation from an equipotential (by up to several kilometers for Arabia and several hundred meters for Deuteronilus). These significant deviations in shoreline elevation from equipotential surfaces (*e.g.*, sea levels) have been used as an argument against formation of the contacts adjacent to a body of liquid water, the interpretation of the features as shorelines, and the existence of a Martian ocean (Malin and Edgett, 1999). However, it is possible the shorelines followed past equipotentials that were subsequently deformed by various geophysical processes. If this can be shown, it would provide additional evidence for the interpretation of the contacts as shorelines, as it would otherwise be a remarkable coincidence that features broadly consistent with a shoreline would follow paleo-equipotential surfaces along the entire boundary of the plains.

5.2.3 Shoreline deformation, True Polar Wander, and Tharsis

Perron et al. (2007) showed that the elevation changes of the Arabia and Deuteronilus contacts can be explained by deformation due to 30-60° and 5-25° of post-Tharsis true polar wander (TPW, solid-body reorientation a planet with respect to its spin axis), respectively, because a varying rotation pole also changes the orientation of a planet's equatorial bulge, or polar flattening, altering equipotential surfaces globally. Such large magnitudes of TPW can be driven by ocean loading/unloading, *but only if Tharsis formed far from the equator* (Perron et al., 2007). If Tharsis formed near the equator, then the remnant fossil bulge would have prevented ocean loading from causing significant amounts of post-Tharsis TPW (see 5.2).

However, most evidence points to the formation of Tharsis near the equator (Willemann, 1984; Roberts and Zhong, 2007; Daradich et al., 2008; Matsuyama and Manga, 2010; Bouley et al., 2016). Mars' remnant rotational figure (fossil bulge) is close to the equator, indicating a paleopole of ($259.5 \pm 49.5°$ E, $71.1^{+17.5°}_{-14.4}$ N), the likely pre-Tharsis orientation of Mars (Matsuyama and Manga, 2010). The pre-Tharsis paleopole also matches the likely orientation of Mars during valley network formation (Bouley et al., 2016). Formation of Tharsis likely drove only limited ($\sim 20°$) TPW to reach Mars' current configuration, which precludes the possibility that surface loads drove sufficient TPW to deform the shorelines (Perron et al., 2007; Kite et al., 2009).

We propose that the Arabia shoreline instead formed prior to or during the early stages of Tharsis emplacement, which initiated >3.7 Ga (Anderson et al., 2001) when the rotation

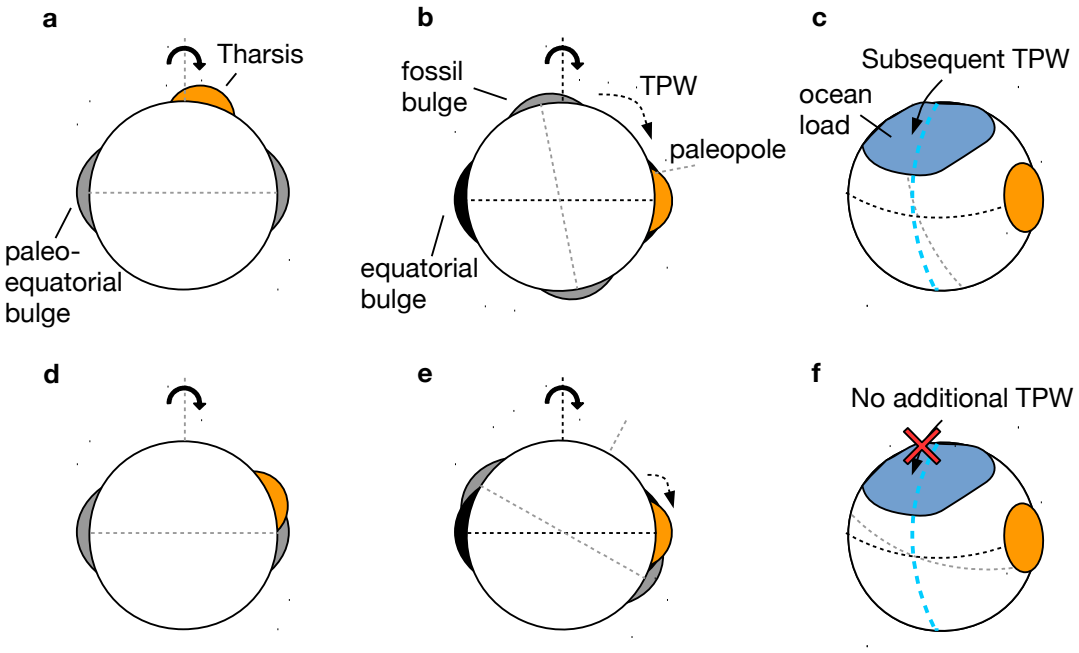

Figure 5.2: Illustration of the feasibility of post-Tharsis TPW depending on the location of Tharsis' formation. (a) Tharsis forms far from the paleo-equator, causing (b) large scale TPW as the planet reorients so Tharsis is at the equator. After the reorientation, the fossil bulge is far from the current equatorial bulge, making the rotation pole sufficiently unstable to allow for (c) ocean loading to cause subsequent TPW along an arc 90° from Tharsis (blue dashed line) (Perron et al., 2007). Alternatively, (d) Tharsis forms near the paleo-equator, causing (e) limited ($\sim$ 20°) TPW. (f) The position of the fossil bulge near the equator stabilizes the planet against subsequent TPW caused by oceans and other surface loads (see Figure S1 of Perron et al. (2007)). Formation of Tharsis near the equator is supported by Matsuyama and Manga (2010) and Bouley et al. (2016).

pole of Mars was at the paleopole (259.5° E, 71.1° N) corresponding to the fossil bulge identified by Matsuyama and Manga (2010). The Arabia shoreline, potentially emplaced $\sim$4 Ga (Clifford and Parker, 2001), would have been modified by both topographic changes from Tharsis (which dominates Mars' topography and gravity on a global scale), and the $\sim$20° of Tharsis-induced TPW. The Deuteronilus shoreline, which differs less from a present-day equipotential than the older Arabia shoreline, is dated to $\sim$ 3.6 Ga (Ivanov et al., 2017), after most of Tharsis was emplaced. However, Tharsis had complex and multi-stage growth that extended into the Hesperian and Amazonian (Anderson et al., 2001; Dohm et al., 2007; Bouley et al., 2018), meaning that the Deuteronilus shoreline would have been deformed by the late stages of Tharsis' emplacement. We examine a chronology in which shoreline deformation is due mainly to Tharsis (Table 5.2.3), and compare expected deformation due to Tharsis with the elevation profiles of the Arabia and Deuteronilus contacts.

Table 5.1: Proposed Shoreline Timeline

Time (epoch)	Event	Effect
$\sim$ 3.9 Ga (Early Noachian)	Arabia shoreline	
$>$ 3.6 Ga (Late Noachian/ Early Hesperian)	Majority of Tharsis forms	Tharsis emplacement/loading deforms the Arabia shoreline*
3.6 Ga (Early Hesperian)	Deuteronilus shoreline	
3.5 Ga (Late Hesperian)	Isidis shoreline	
3.6 Ga $-$ present (Early Hesperian$-$ Late Amazonian)	Remainder of Tharsis forms	Remaining Tharsis growth deforms Arabia, Deuteronilus, and Isidis shorelines
3.5 $-$ 3.0 Ga (Late Hesperian/ Early Amazonian)	Loading of Isidis/Utopia	Flexure from Isidis/Utopia loading deforms shorelines

* Limited contribution also from Tharsis-induced TPW (20°)

5.3 Methods

To determine if the shorelines would have followed equipotentials earlier in Mars' history, we compare the present day topography of the shorelines to the expected deformation that may have occurred since their formation. We construct shoreline deformation profiles to determine how an equipotential surface (at the coordinates of each shoreline) would have been deformed since its formation. If the present-day shoreline topography has low misfit compared to the shoreline deformation profile, then it is possible the shoreline represents a paleo-equipotenial surface subsequently deformed by the processes used to construct the shoreline deformation profile. Although many small-scale processes can cause short-wavelength shoreline deformation, we focus on three main processes that can cause long-wavelength deformation of the shorelines: flexure associated with True Polar Wander, the growth of Tharsis, and surface loading.

5.3.1 Deformation from True Polar Wander

The topographic response to True Polar Wander (TPW) is given by the change in the flattening of the planet caused by the difference between the centrifugal potential at the initial and final rotation poles (Perron et al., 2007). For a shoreline in place before TPW occurs, the deformation of the shoreline topography due to TPW (Perron et al., 2007) is:

$$\Delta T_{\mathrm{TPW}}(\theta,\phi) = \frac{\omega^2 a^2}{3g}[P_{2,0}(\cos\gamma) - P_{2,0}(\cos\theta)][h_2 - (1+k_2)] \tag{5.1}$$

where a is the mean planetary radius, ω is the rotation rate, γ is the angular distance between the current colatitude and longitude (θ,ϕ) and the paleo-pole, the unnormalized degree-2 Legendre polynomial $P_{2,0}(\cos\eta) = \frac{1}{2}(3\cos^2\eta - 1)$, and h_2 and k_2 are the secular (fluid-limit) degree-2 Love numbers that depend on the density and elastic structure of Mars.

In Perron et al. (2007), TPW due to post-Tharsis ocean unloading was considered as the only source of shoreline deformation, and accordingly they conducted a global search for paleopoles that produced shoreline deformation profiles matching present-day shoreline topography. Here, we assume that the majority of TPW was driven by Tharsis loading. We fix the paleopole at (259.5° E, 71.1° N), which corresponds to the fossil bulge identified by Matsuyama and Manga (2010), which also matches rotation pole at the time that the valley networks formed (Bouley et al., 2016). This corresponds to $\sim 20°$ of TPW.

Whether Tharsis-driven TPW could have deformed a shoreline depends on the shoreline's age. The Arabia shoreline, dated to the Noachian, could have been emplaced prior to or during the early stages of Tharsis' formation, and therefore could have been deformed by subsequent Tharsis-driven TPW. The Deuteronilus shoreline, however, was likely emplaced during the late stages of Tharsis' formation, and therefore probably post-dates most Tharsis-induced TPW. Tharsis driven TPW should have occurred within a few Myr of load emplacement (Rouby et al., 2008), and estimates of load-driven TPW on Mars suggest timescales less than 10 Myr (Harada, 2012; Chan et al., 2014; Hu et al., 2017), well within the required pre-Deuteronilus timescale. Although a fraction of the 20° of Tharsis-induced TPW may be due to relaxation of the lithosphere and occur on longer timescales (Moore et al., 2017), this should have a negligible effect given the small influence of TPW on shoreline deformation (Figure 1a).

In Figure 5.3a,b we compare the expected deformation due to TPW driven by ocean unloading (Perron et al., 2007) or Tharsis formation (Matsuyama and Manga, 2010). For Tharsis-driven TPW, we use best-fit pre-Tharsis paleopole (259.5° E, 71.1° N) from Matsuyama and Manga (2010) and an elastic lithosphere thickness T_e = 58 km, the expected value at the time of Tharsis' emplacement (Matsuyama and Manga, 2010), corresponding to h_2=2.0 and k_2=1.1 (Bouley et al., 2016). For TPW driven by ocean unloading, we use the best-fit paleopole for the Arabia shoreline (334° E, 40° N) from Perron et al. (2007) for T_e=200km, corresponding to h_2=1.663 and k_2=0.899. Because of the low T_e and low magnitude of Tharsis-driven TPW (18.9°), we find that Tharsis-driven TPW results in small (almost negligible) amounts of shoreline deformation compared to the ocean unloading driven TPW of Perron et al. (2007), which considered larger values of T_e (100-400 km) and larger magnitudes of TPW (up to 60°) (Figure 5.3a,b).

5.3.2 Deformation from Tharsis

Tharsis dominates the shape and gravity figure of Mars. Tharsis' emplacement and associated loading caused global deformation of the planet, resulting in the Tharsis rise, an antipodal bulge, and a circum-Tharsis trough. Any shoreline that formed prior to Tharsis, would have experienced significant deformation due to flexure associated with Tharsis' growth. Any shoreline that formed in the middle stages of Tharsis' growth would have been deformed by whatever Tharsis-induced flexure occurred after the shoreline's emplacement.

The change in topography due to the emplacement of Tharsis and its associated loading is:

$$\Delta T_{\text{Tharsis}}(\theta, \phi) = S_{\text{Tharsis}}(\theta, \phi) - N_{\text{Tharsis}}(\theta, \phi) \tag{5.2}$$

where S_{Tharsis} and N_{Tharsis} are Tharsis' contribution to the shape and geoid of Mars, respectively.

Equation 5.2 can be scaled depending on when the shoreline is expected to have formed. If a shoreline formed prior to all of Tharsis' formation, the contribution of Tharsis in the shoreline deformation profile would be $\Delta T_{\text{Tharsis}}$. However, if for example a shoreline was emplaced after Tharsis was 60% complete, the contribution of Tharsis deformation to the shoreline deformation profile would be $0.4 \cdot \Delta T_{\text{Tharsis}}$, the expected flexure due to the remaining 40% of Tharsis emplacement and associated loading.

Primarily, we use the gravity and shape coefficients for Tharsis up to degree-5 from Matsuyama and Manga (2010). However, for the Deuteronilus shoreline we also use a degree-50 gravity model for Tharsis provided by James Keane. Both Tharsis deformation models show that the expected deformation due to Tharsis is much greater than that of TPW, suggesting that Tharsis could be a more significant factor in shoreline deformation than TPW (see Figure 5.3 for a comparison of expected deformation from Tharsis and TPW models).

The degree-50 Tharsis gravity model was developed by J. Keane using the same methods that Keane and Matsuyama (2014) used to examine the fossil figure of the Moon. While the degree-5 model is based on a single axisymmetric load, the degree-50 model is constructed using a linear combination of multiple uniform density spherical caps, producing a globally non-axisymmetric Tharsis geoid model. We computed the corresponding change in shape due to Tharsis using the degree-50 gravity coefficients and following the method of Matsuyama and Manga (2010). To compute the load and displacement load Love numbers, we used the ALMA code (Spada, 2008) and a 5-layer model of Mars from Matsuyama and Manga (2010). While the degree-50 model has the potential to eventually be more accurate, it is still a work in progress and a full parameter search for the best fit cap location and surface densities has not yet been conducted. However, because the degree-50 model is composed of several distinct caps, it is possible to isolate the contribution of certain regions of Tharsis to the geoid. This is useful for a shoreline like Deuteronilus, where there is evidence that while the Deuteronilus shoreline likely formed after Tharsis was mostly complete, select volcanic centers may have formed entirely after the Deuteronilus shoreline was emplaced.

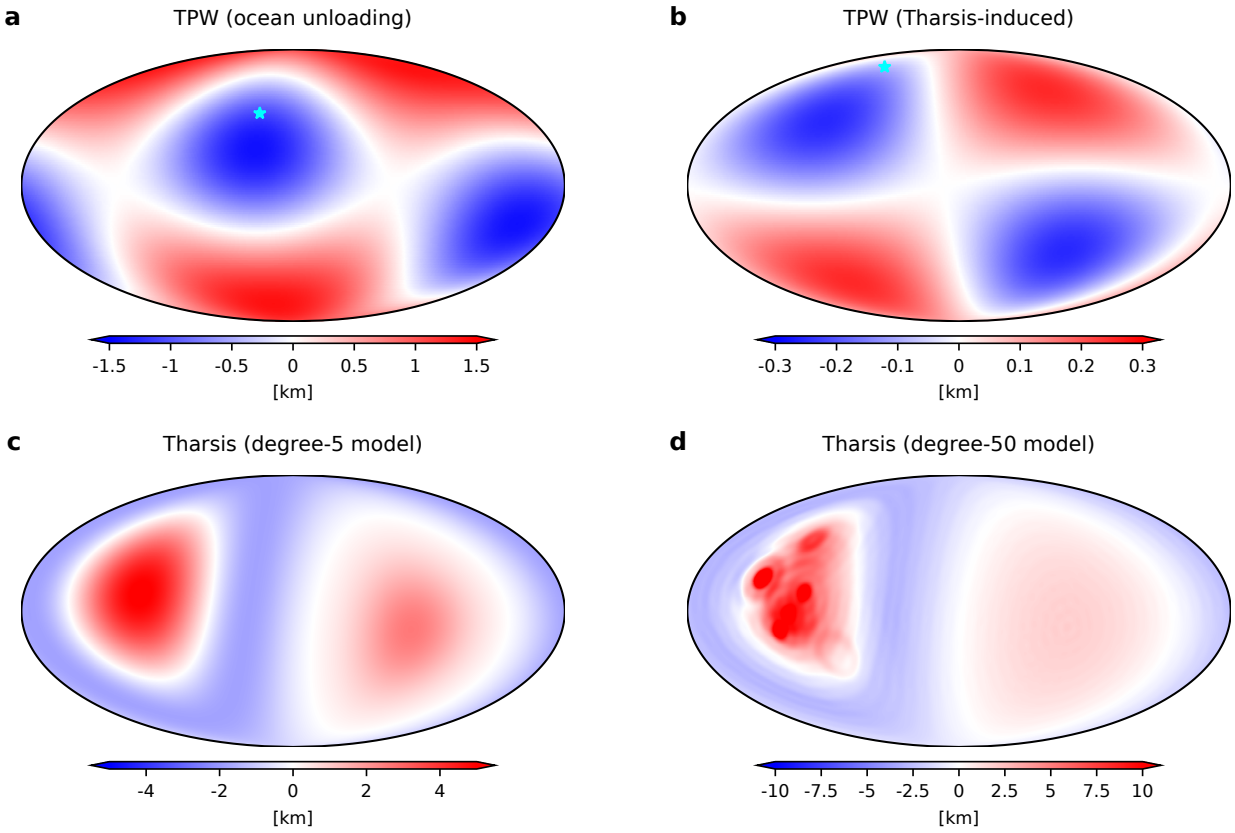

Figure 5.3: Deformation from TPW and Tharsis. (a) Deformation from TPW caused ocean unloading following Perron et al. (2007) using their best-fit paleopole for the Arabia shoreline (334° E, 40° N) with T_e=200km (50° of total TPW). (b) Deformation from Tharsis-driven TPW using the best-fit pre-tharsis paleopole (259.5° E, 71.1° N) from Matsuyama and Manga (2010) for T_e=58km (18.9° of total TPW). The paleopoles used for TPW calculations are marked as cyan stars. (c) Deformation from Tharsis and associated loading using the coefficients from Matsuyama and Manga (2010) (degree-5 in spherical harmonics). (d) Tharsis deformation computed using a preliminary model from J. Keane (computed up to degree-50 in spherical harmonics). The magnitude of Tharsis deformation is greater than that of TPW.

Both the degree-5 and degree-50 Tharsis models depend on the assumed T_e. Varying T_e within the expected range did not alter our conclusions (see Section).

It is important to note that the degree-5 model of Tharsis deformation is derived by directly fitting a model of Tharsis to the Mars gravity data (Matsuyama and Manga, 2010). Figure 5.4 follows the method of Matsuyama and Manga (2010) for removing Tharsis and the fossil bulge from the Mars geoid. Matsuyama and Manga (2010) removed a degree-5 model of Tharsis from the non-equilibrium Mars geoid, revealing a fossil bulge that constrained Tharsis-induced TPW to 20°. Removing the fossil bulge from the geoid reveals a residual

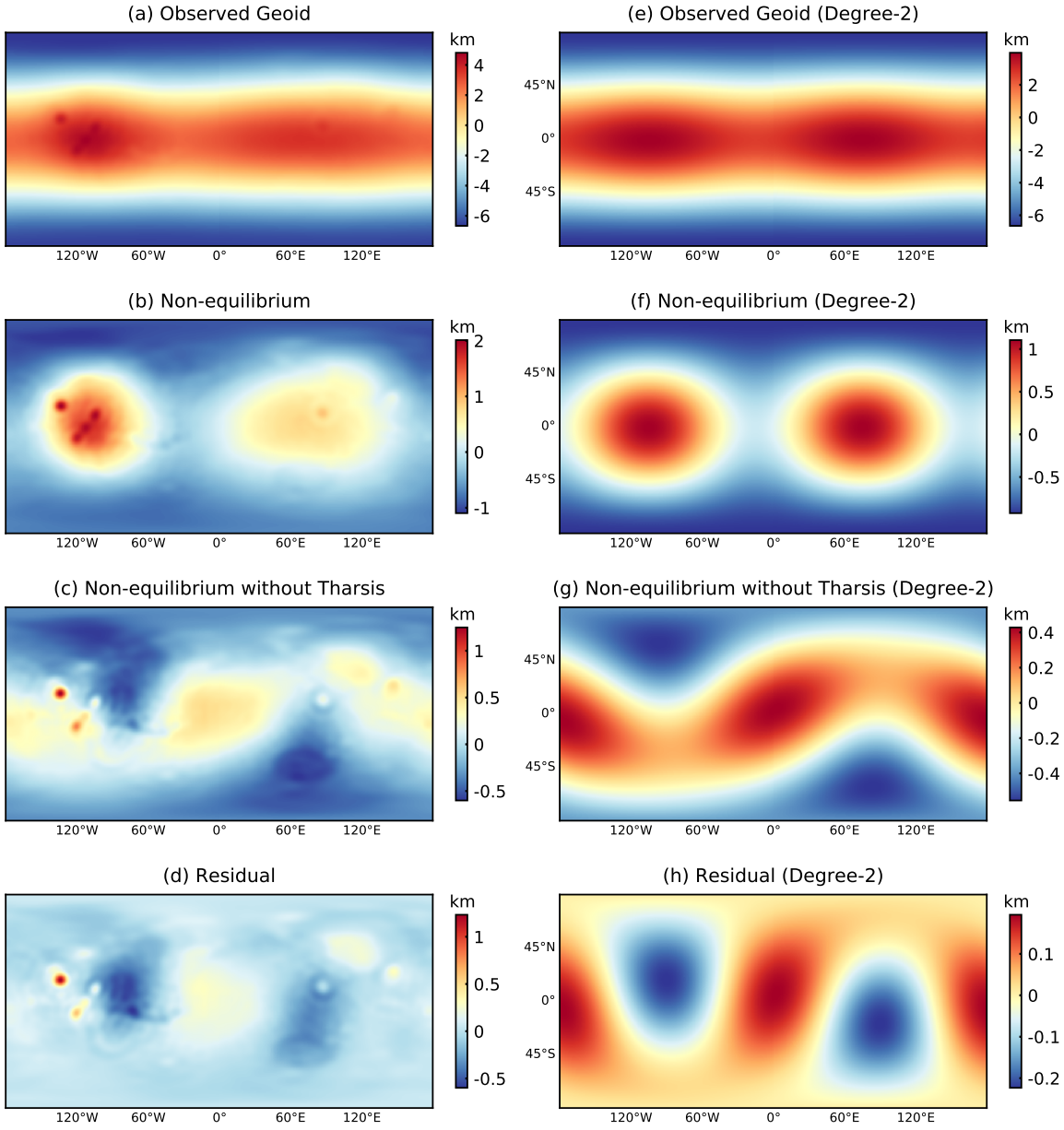

Figure 5.4: Mars geoid with and without Tharsis and the fossil bulge. (a) Observed geoid of Mars (up to degree-40. (b) Geoid without the equilibrium rotational figure. (c) Geoid without the equilibrium rotational figure and Tharsis. (d) Geoid without the equilibrium rotational figure, Tharsis, and the remnant rotational figure (fossil bulge). (e-h) As in (a-d) but only the degree-2 component. Figure is constructed following Matsuyama and Manga (2010) (compare with their Figure 6). Gravity field is from MRO95A (Zuber, 2008).

geoid. The residual geoid contains excess contributions to the geoid from other sources such as surface loads, but also contains artifacts from misfit in the model used to remove the Tharsis and fossil figure contributions. Additionally, short-wavelength Tharsis contributions are still present in the residual geoid because Tharsis is only modeled up to degree-5. While not perfect, the model of Matsuyama and Manga (2010) can remove most of the long-wavelength Tharsis contributions to the Mars geoid (and topography). The residual geoid, while generally small in magnitude, reveals the removal of Tharsis could require further improve. Additionally, the residual geoid shows that excess contributions such as surface loads may also contribute to shoreline deformation on more regional scales.

5.3.3 Deformation from surface loads

We also consider deformation from surface loads less global than Tharsis, but still significant enough to cause large amounts of regional deformation. The main loads we consider are loading of the Isidis basin, loading of the Utopia basin, and ocean loading (filling the plains up to shoreline levels with liquid water).

Ocean loading is not expected to significantly deform the shorelines (Perron et al., 2007), however, given the difference in our deformation models compared to those of Perron et al. (2007), we compute deformation from ocean loading to determine if flexure due to ocean loads could be a significant source of error in our shoreline deformation models.

Based on the extensive dip in the Arabia shoreline, VN termini, and Delta elevations in the Isidis region (Figure X), we expect that loading of the Isidis basin may contribute to shoreline deformation in the cirum-Isidis region. The Isidis basin displays a large positive free-air gravity, which combined with geological observations, suggests it may have been filled by a significant amount of sedimentary and volcanic deposits (Ritzer and Hauck, 2009). Using a model of loading induced plate flexure (described below), we can test if a reasonable amount of infill can explain the dip in shoreline elevations in the Isidis region.

The Utopia basin is another significant site of suggested loading induced flexure, which could have deformed shorelines in the circum-Utopia region (which includes the Isidis basin). The Utopia basin has a significant positive gravity anomaly (Sjogren, 1979; Zuber et al., 2000), indicating $\sim$ 18 km of excess fill (Searls et al., 2006). Such a load would have caused elastic plate flexure and a peripheral bulge, which could have tilted the Isidis basin (McGowan and McGill, 2006), potentially explaining why the Isidis shoreline has higher elevations on the NE rim than the SW rim. We therefore also model flexure caused by Utopia infill, and determine if it can explain some of the shoreline elevation anomalies in this region.

Infill of Isidis and Utopia is expected to be caused by both lava flows (from Syrtis into Isidis, and from Elysium into Utopia), and sediment. Sediment deposition could occur directly from a northern ocean, as a receding water/mud/ice ocean would be expected to deposit a large portion of sediment in Utopia, because it is the lowest elevation in the northern lowlands. If shorelines can be dated accurately, and the relative contribution of deformation from Isidis/Utopia loading quantified, then it may also be possible to constrain the rate of deposition and infill in Isidis and Utopia over time.

To compute the flexure associated with surface loading, we use the thin elastic shell approximation, as described in Evans et al. (2014) and based on Johnson et al. (2000) and Turcotte et al. (1981). Loads are described in spherical harmonics as a load thickness h, which results in a deflection w. The deflection is computed in spherical harmonics from the load thickness using:

$$w_{lm} = -\frac{\rho_L}{\Delta\rho}\alpha_l h_{lm} \tag{5.3}$$

where ρ_L is the load density and $\Delta\rho$ is the difference in density between the crust and mantle. The transfer function α_l is given by:

$$\alpha_l = \left[1 - \frac{3\rho_m}{(2l+1)\bar{\rho}}\right]\left[\frac{1}{\zeta_l} - \frac{3\rho_m}{(2l+1)\bar{\rho}}\right]^{-1} \tag{5.4}$$

where $\bar{\rho}$ is the mean bulk density of Mars, and ζ_l is given by:

$$\zeta_l = \frac{-[l(l+1) - (1-\nu)]}{\sigma[-l^3(l+1)^3 + 4l^2(l+1)^2 - 4l(l+1)] + \tau[-l(l+1)+2] + [-l(l+1) + (1-\nu)]} \tag{5.5}$$

where ν is the Poisson's ratio. The dimensionless parameters τ and σ are given by:

$$\tau = \frac{ET_e}{R^2 g \Delta\rho} \tag{5.6}$$

where E is the Young's modulus and R is the radius of the shell, computed as $R = R_{\text{Mars}} - T_e/2$, and

$$\sigma = \frac{D}{R^4 g \Delta\rho} \tag{5.7}$$

where D is the flexural rigidity $D = ET_e^3/12(1-\nu^2)$.

The change in topography due to surface loading is given by:

$$\Delta T_{\text{Load}} = h + w \tag{5.8}$$

which is computed in spherical harmonics based on the estimated surface load thickness h and computed displacement w. For a given shoreline and we can estimate the contribution of a surface load (either infill of Isidis or Utopia, or an ocean load) to shoreline deformation by computing the expected deformation from flexure caused by loading, ΔT_{Load} along each point of the shoreline. We use parameter values given in Table 5.2. The elastic lithosphere thickness T_e is varied depending on the timing of the expected loading (since T_e increases over time due to secular cooling of the planet), and the load density ρ_L is varied depending on the type of load (a water ocean or infill from sediments and lavas).

Table 5.2: Thin Shell Loading Model Parameters

Parameter	Symbol	Value
Crust density	ρ_c	3400 kg m^{-3}
Load density	ρ_L	1000 − 2900 kg m^{-3}
Mantle density	ρ_m	3400 kg m^{-3}
Mean bulk Mars density	$\bar{\rho}$	3940 kg m^{-3}
Poisson's ratio	ν	0.25
Elastic Lithosphere thickness	T_e	58 − 100 km
Young's Modulus	E	10^{11} N m^{-2}
Mean Mars radius	R_{Mars}	3389.5 km
Gravitational acceleration	g	3.73 m s^{-2}

5.4 Shoreline deformation profiles

Given the three main types of long-wavelength shoreline deformation, Tharsis, TPW, and loading, we compute a generalized shoreline deformation profile as:

$$\Delta T = C\Delta T_{\text{Tharsis}} + \Delta T_{\text{TPW}} + \Delta T_{\text{Load}} + Z \tag{5.9}$$

where $\Delta T_{\text{Tharsis}}$, ΔT_{TPW}, and ΔT_{Load} are the deformation from Tharsis, TPW, and surface loading, as defined previously, Z is a constant offset that represents sea-level at the time of shoreline formation, and C is a constant that represents the fraction of Tharsis deformation that occurred after the shoreline was emplaced. For example, if a shoreline formed prior to all of Tharsis growth and associated deformation then $C = 1$, whereas if a shoreline formed after Tharsis was 80% complete, then $C = 0.2$ because the shoreline would only be deformed by the remaining 20% of Tharsis' growth and associated deformation. The parameters C and Z can be adjusted to find the best-fit with the current shoreline topography data. If a shoreline deformation profile ΔT matches the long-wavelength present-day topography of a shoreline, then it is possible that the shoreline was emplaced as a paleo-equipotential, and obtained its present-day topography via deformation from the same processes invoked in constructing the shoreline deformation profile. We claim that matching shoreline topography to reasonable shoreline deformation profiles can be used as evidence the shorelines were emplaced along equipotentials Gyrs ago, supporting the hypothesis that they are shorelines formed by ancient oceans. We construct shoreline deformation profiles for the Arabia, Deuteronilus, and Isidis shorelines, to determine if their topographic deviations from present-day equipotential surfaces can be explained by deformation from Tharsis, TPW, and/or surface loads.

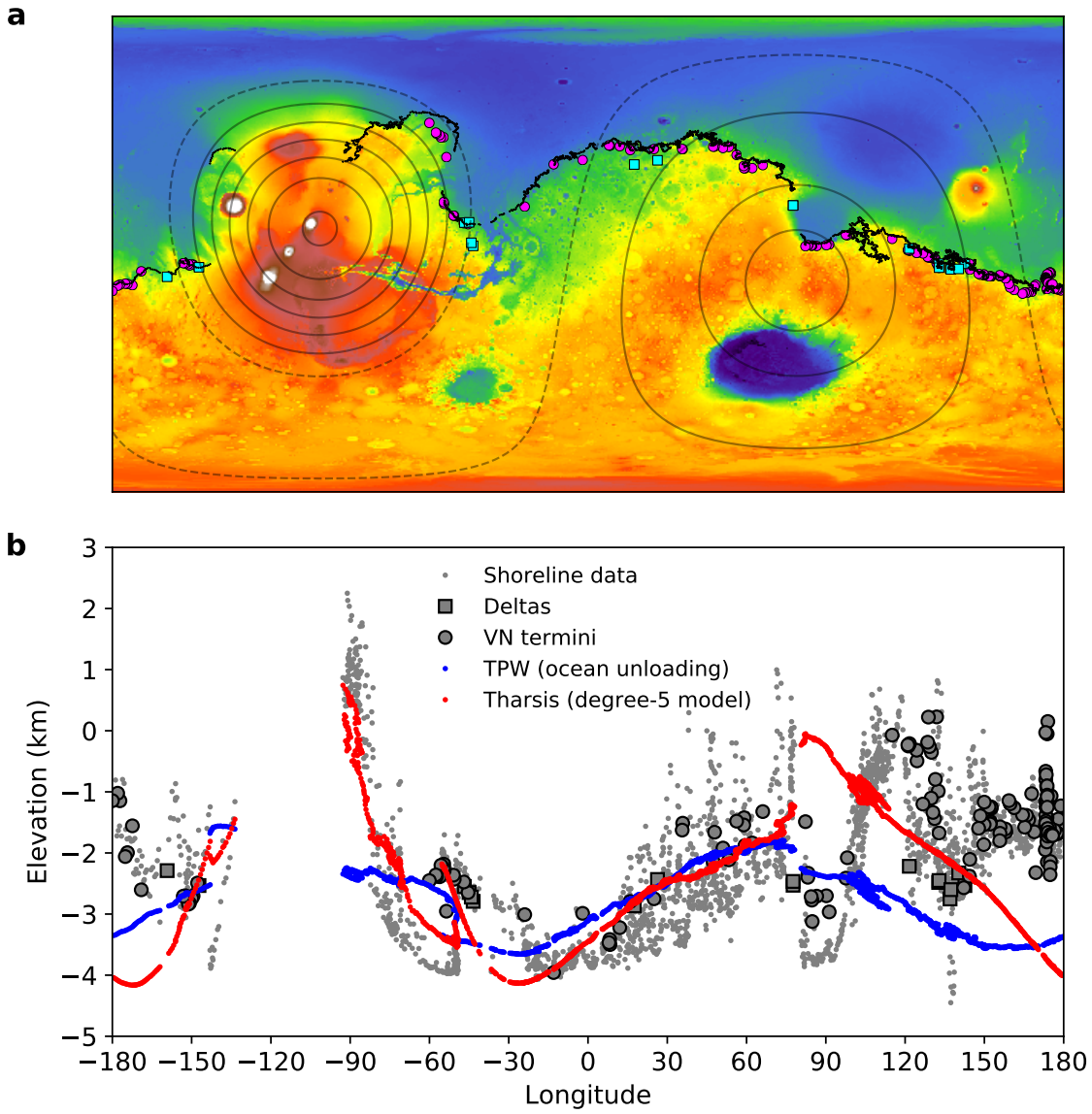

Figure 5.5: Comparison of Arabia shoreline topography to TPW and Tharsis deformation. (a) Mars topography, with the Arabia shoreline (black), VN termini (magenta circles), and deltas (cyan squares), as in Figure 5.1. The contribution of Tharsis to Mars' topography up to degree-5 (Matsuyama and Manga, 2010) is displayed as 1-km dark grey contours (dashed contours are negative). (b) Current topography of the Arabia shoreline (grey dots) from (Clifford and Parker, 2001), along with VN termini and deltas, compared to the Perron et al. (2007) model of deformation due to post-Tharsis TPW caused by ocean unloading (blue line) using T_e=200km, and our model of deformation due to Tharsis emplacement and associated loading (red line), $\Delta T_{\text{Tharsis}} - 2.3$km, based on the degree-5 Tharsis model.

5.5 Arabia shoreline

We show that the Arabia shoreline's deviations from an equipotential can be explained almost entirely by deformation due to Tharsis emplacement (Figure 5.5). The degree-5 Tharsis model ($\Delta T_{\text{Tharsis}} - 2.3$km) follows large portions of the shoreline data, particular in the Arabia Terra (-20°E to 80°E) and Tempe Terra (-90°E to -60°E) regions. We compare the deformation from Tharsis to that of TPW driven by ocean unloading (Perron et al., 2007). TPW driven by ocean unloading follows the shoreline data in the Arabia Terra region, but fails to follow the large changes in elevation flanking Tharsis. Deformation of Tharsis appears to better explain the bulk of the shoreline deformation, which the degree-2 TPW model cannot fully capture. However, the Tharsis deformation model still fails to follow the shoreline data in the circum-Tharsis trough (150 to 210°E and -60 to 0°E). This may represent a deficiency in the deformation model (a work in progress) or require an extension of the model to include other processes. There is also significant deviation in shoreline elevations from the Tharsis model in the Isidis region (80 - 100° E); this can be explained by loading of the Isidis basin and will be discussed later.

The model of the Tharsis deformation can be adjusted in several ways, and we compare several adjustments to our model of Tharsis deformation in Figure 5.6. First, we modify the percent contribution of Tharsis deformation to shoreline topography. In Figure 5.5 we use a shoreline deformation profile of $\Delta T_{\text{Tharsis}} - 2.3$km, which assumes that the Arabia shoreline was emplaced prior to Tharsis formation and deformed by the remaining 100% of Tharsis growth. However, it is possible that the Arabia shoreline was emplaced in the early stages of Tharsis formation and was deformed by whatever portion of Tharsis was emplaced after the shoreline formed. In Figure 5.6 we show a case where the Arabia shoreline was formed after Tharsis was 30% complete and was deformed by the remaining 70% of Tharsis growth, following a deformation profile $0.7 \cdot \Delta T_{\text{Tharsis}} - 2.3$km. The best-fit for the Arabia shoreline is actually $0.9 \cdot \Delta T_{\text{Tharsis}} - 2.03$km (shown in Section 5.8, Figure 5.11), indicating the Arabia shoreline formed after Tharsis was 10% complete. However, given the uncertainties in the deformation model and the large errors in the Arabia shoreline data, it is difficult to conclusively say if the Arabia shoreline formed prior to Tharsis or during the early stages of Tharsis' growth.

We also consider if the $\sim 20°$ of Tharsis-induced TPW could contribute to any major changes in shoreline topography, which could be the case if the Arabia shoreline formed before or during the early stages of Tharsis' growth, prior to any Tharis-induced TPW. In Figure 5.6, we consider a case where the shoreline is deformed by both Tharsis loading/flexure and Tharsis-induced TPW, $\Delta T_{\text{Tharsis}} + \Delta T_{\text{TPW}} - 2.3$km, where ΔT_{TPW} is based on the paleopole from Matsuyama and Manga (2010). We find that changing including Tharsis-induced TPW has a minimal effect. As seen in Figure 5.3b, Tharsis-induced TPW is small (< 0.25 km) due to the low magnitude of TPW and the low T_e at the time of Tharsis emplacement. The majority of the deformation appears to be a result of Tharsis loading and associated deformation, with minimal contributions from Tharsis-induced TPW.

We also examine if a different model of Tharsis deformation could improve the fit to the

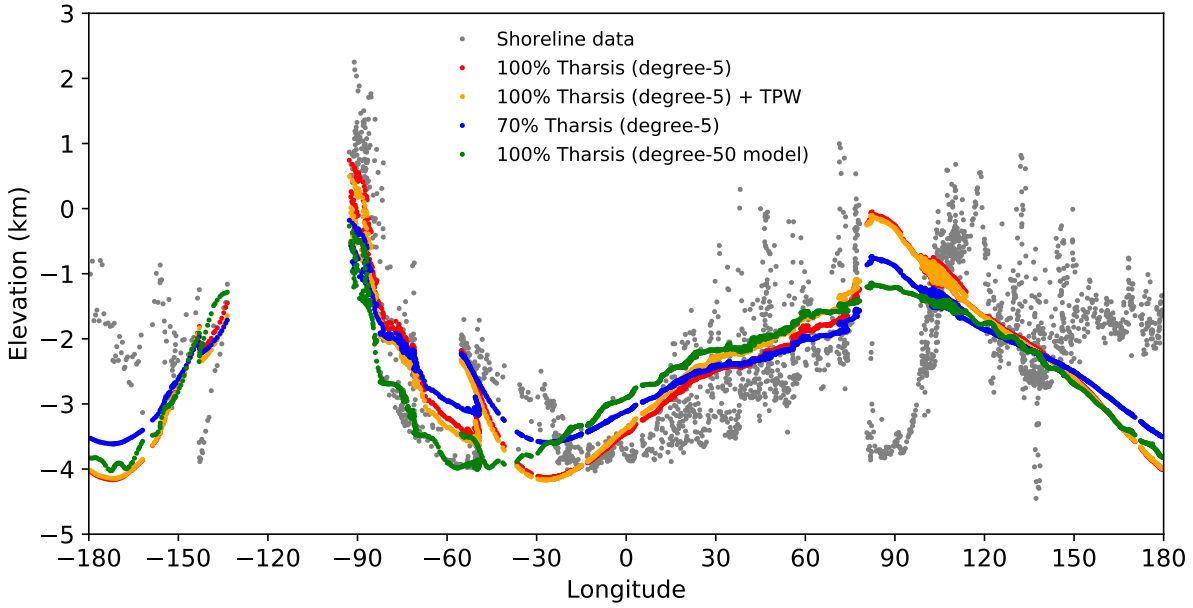

Figure 5.6: Comparison of Arabia shoreline topography to various Tharsis deformation models. Shoreline topography (grey dots) is compared to various types of Tharsis deformation. Deformation from 100% contribution from Tharsis, using the degree-5 model, is shown in red ($\Delta T_{\text{Tharsis}} - 2.3\text{km}$). Deformation from 100% contribution of Tharsis (degree-5) plus Tharsis-induced TPW is shown in orange ($\Delta T_{\text{Tharsis}} + \Delta T_{\text{TPW}} - 2.3\text{km}$). Deformation from 70% contribution of Tharsis (degree-5) is shown in blue ($0.7 \cdot \Delta T_{\text{Tharsis}} - 2.3\text{km}$). Deformation from 100% contribution of Tharsis (degree-50 model based on gravity fit from J. Keane) is shown in green ($\Delta T_{\text{Tharsis}} - 2.3\text{km}$).

shoreline data, particularly in the circum-Tharsis trough. We use a degree-50 model based on the gravity fit by J. Keane, and compare it to the degree-5 model. In Figure 5.6, we show the degree-50 fit based on a 100% contribution of Tharsis deformation ($0.7 \cdot \Delta T_{\text{Tharsis}} - 2.3\text{km}$). As seen in Figure 5.6, the degree-50 fit displays large misfit to the shoreline data in the same regions as the degree-5 fit. Use of a different T_e when constructing the Tharsis deformation model might improve the fit, but likely will only change the amplitude of the signal, and may not correct the misfit in the circum-Tharsis trough. It is possible that both degree-5 and degree-50 models may fail to approximate the deformation in the cirum-Tharsis trough due to some deficiency in the model assumptions, for example, modeling the entire Tharsis load as a surface load instead of a combination of internal and surface loads. Use of a globally uniform T_e is another simplification in the Tharsis deformation model, as the the lithosphere can have regional variations in thickness (*e.g.*, Grott and Breuer, 2010; Thiriet et al., 2018). However, it is also possible that the degree-50 model could produce a better fit once it is more refined. The model used in this work is preliminary, and the fit to the Tharsis data can be adjusted further, while accounting for the remnant rotational bulge, in

order to produce a better fit to the Tharsis data. While Tharsis deformation can explain most of the long-wavelength trend in the shoreline data, misfit in the circum-Tharsis trough remains an issue.

Apart from the circum-Tharsis trough, the other main region of misfit is the dip in shoreline, VN termini, and delta elevations in the circum-Isidis region. We examine if this can be explained by loading of the Isidis basin with sediments and lavas, as suggested by Ritzer and Hauck (2009). Using a thin elastic shell plate flexure model (as described in Section 5.3.3), we center loads of various mass on the Isidis basin and determine the deflection at the shoreline data locations. We use a load density of 3000 kg m^{-3} and T_e=60km, with other parameters as defined in Table 5.2. We find that deflection of the shoreline in the Isidis region can be explained by load 3km thick and 355km in radius, as shown in Figure 5.7. We do not fine tune the loading solution, since many combinations of load density, T_e, and cap size should produce a similar depression in the Isidis region that can fit the shoreline data. A load density >2900 kg m^{-3} is suggested by Ritzer and Hauck (2009). We use T_e close to 58km (the estimated T_e at the time of Tharsis formation from Matsuyama and Manga (2010)), which is slightly lower than the 100-180 km estimate at the time of Isidis loading from Ritzer and Hauck (2009). Overall our results seem consistent with those of Ritzer and Hauck (2009), and our load geometry is also similar to the cap geometry used by J. Keane to fit the Isidis gravity anomaly in his degree-50 fit to mascons in gravity field of Mars. Loading of the Isidis basin can explain the dip in shoreline, VN termini, and delta elevations in the cirum-Isidis region.

The Arabia shoreline is one of the oldest identified shorelines on Mars. The large changes in elevation (by up to several km) have been used as an argument against the interpretation of the geological contact as a shoreline. We have shown that the large changes in elevation along the Arabia shoreline can be explained almost entirely by deformation due to the emplacement of Tharsis, with an additional contribution from Isidis loading in the circum-Isidis region of the shoreline. While the degraded state of the shoreline makes its geological interpretation as a shoreline more difficult, the shoreline's coincidence with VN termini and delta deposits provides more supporting evidence for its interpretation as a shoreline. That all of these features (the shoreline, VN termini, and deltas) follow the same deformation profile due to Tharsis and Isidis loading supports the hypothesis that these features were emplaced prior to or during the early stages of Tharsis formation, along an equipotential. The emplacment of these features along an equipotential supports the hypothesis that these features were emplaced during the existence of an ancient martian ocean. Of course, there are still some regions where the model of Tharsis deformation fails to follow the shoreline elevations, particularly in the circum-Tharsis trough. Future work updating the degree-50 Tharsis model or considering other processes could potentially explain the deviations to the Tharsis fit in the circum-Tharsis trough.

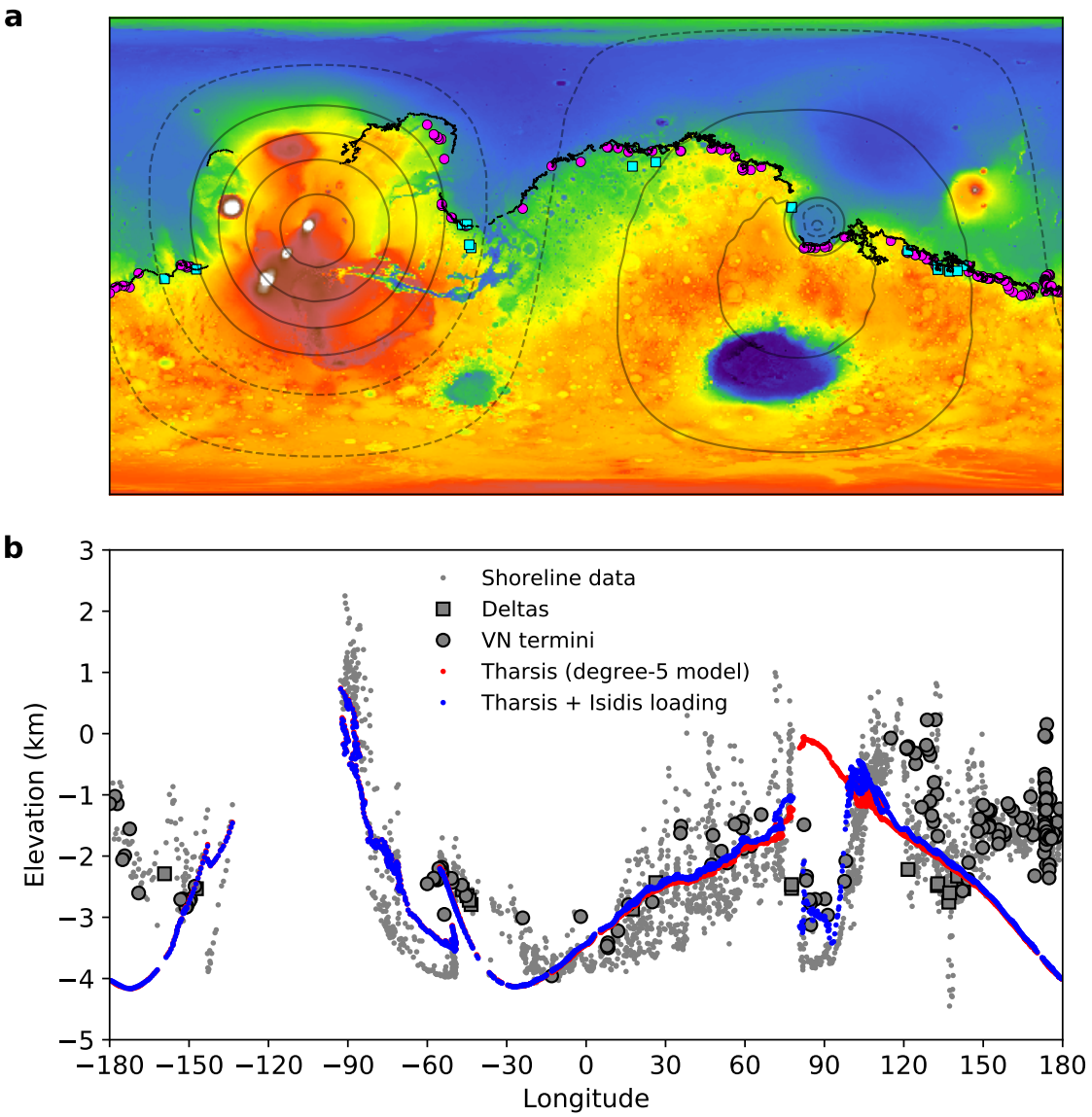

Figure 5.7: Comparison of Arabia shoreline topography to Tharsis deformation with Isidis loading. (a) Mars topography, with the Arabia shoreline (black), VN termini (magenta circles), and deltas (cyan squares), as in Figure 5.1. Contours display deformation from both Tharsis (degree-5) and Isidis loading (3km thick cap centered on Isidis, with a radius of 355km) (contours spaced 1-km, dashed contours are negative). Isidis loading causes a clear depression in the Isidis basin (compare with Figure 5.5a). (b) Current topography of the Arabia shoreline (grey dots), compared to deformation due to Tharsis emplacement and associated loading (red line, $\Delta T_{\text{Tharsis}} - 2.3\text{km}$), and Tharsis deformation plus Isidis loading (blue line, $\Delta T_{\text{Tharsis}} + \Delta T_{\text{Load}} - 2.3\text{km}$).

5.6 Deuteronilus shoreline

The Deuteronilus shoreline (Figure 5.8a) is younger and much better defined (geologically) than its older counterpart, the Arabia shoreline. Ivanov et al. (2017) recently remapped the shoreline, which represents the edge of the Vastitas Borealis Formation, and dated the shoreline to 3.6 Ga. The Deuteronilus shoreline also contains long-wavelength variations in its topography, but the magnitude of deviation from an equipotental are significantly less than for the Arabia shoreline (100s of m instead of several km).

Because of the younger age of the Deuteronilus shoreline (post-dating Tharsis formation by >100Myr), we assume the shoreline formed during the later stages of Tharsis formation, and after any Tharsis-induced TPW was complete. The topography of the Deuteronilus shoreline should therefore follow a deformation profile $C\Delta T_{\text{Tharsis}} + Z$, where C is a constant representing whatever portion of Tharsis deformation occurred after the shoreline's formation, and Z is a constant to represent sea-level at the time of shoreline emplacement. We vary C and Z to determine a best-fit to the shoreline data. Our best fit, $0.17\Delta T_{\text{Tharsis}} - 3.68$ km, yields $\sigma_{\text{rms}} = 0.110$ km. Figure 5.8b compares our best fit for Tharsis deformation to the shoreline data, and also displays the best fit using TPW driven by ocean unloading, following Perron et al. (2007) for T_e=200km. While both models capture much of the long-wavelength variations in shoreline elevation, our model of Tharsis deformation successfuly recovers the low elevation of the Phlegra contact, and also captures the decrease in elevation across Utopia and Elisium West.

Neither our model nor the Perron et al. (2007) model captures the high elevation of the Tantalus segment. However, the Tantalus segment is the closest shoreline segment to Alba Mons, one of the most recent volcanic centers of the vast Tharsis complex. The bulge from more recent activity at Alba Mons could have preferentially uplifted the Tantalus shoreline segment. Being one of the most recent Tharsis upwellings, Alba Mons could completely post-date shoreline formation, and Ivanov et al. (2017) note fractures generated by and radiating from Alba Mons intersect and are superimposed on the Deuteronilus shoreline. To test this hypothesis, we use the degree-50 Tharsis model based on the gravity fit by J. Keane. In the degree-50 model (Figure 5.9a), each center of Tharsis is fit by a series of distinct caps, allowing us to isolate the effect of the Alba Mons complex. We can therefore fit the shoreline to a deformation profile that accounts for some percentage of bulk Tharsis deformation, but tunes the deformation from the Alba Mons portion of Tharsis to 100%. The best-fit deformation profile for the shoreline to the degree-50 fit is found to be $0.14 \cdot \Delta T_{\text{Tharsis}} + 1.0 \cdot \Delta T_{\text{Alba}} - 3.6$ km, indicating the shoreline topography can be explained by the remaining 14% of Tharsis growth and 100% of deformation associated with the formation of Alba Mons. As shown in Figure 5.9b, including the 100% contribution from Alba Mons can partially recover the high elevation of the Tantalus segment. Because the degree-50 model of Tharsis deformation is preliminary, we expect that the model may be under-fitting deformation from Alba Mons, and refinement of the model may explain the full elevation increase of the Tantalus segment.

While the Deuteronilus shoreline displays less variation in topography than the Arabia shoreline, Deuteronilus clearly follows a deformation profile indicating it could have formed

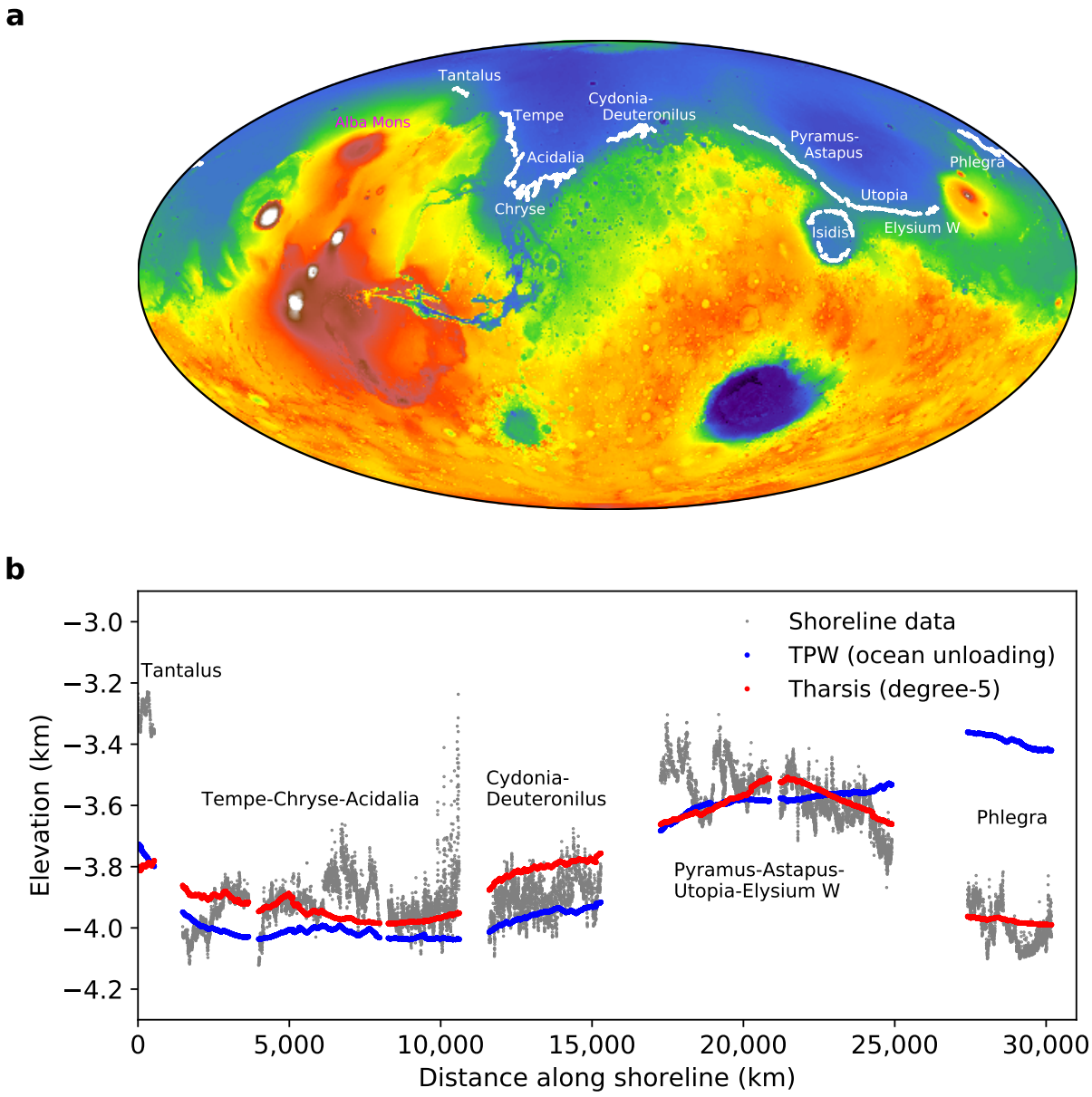

Figure 5.8: Comparison of Deuteronilus shoreline topography to shoreline deformation models. (a) Mars topography with the Deuteronilus shoreline shown in white (data and segment names from Ivanov et al. (2017)). (b) Current Deuteronilus shoreline topography (Ivanov et al., 2017) compared to the Perron et al. (2007) model (blue line) of TPW driven by ocean unloading (for T_e=200km) and our model (red line) of deformation due to partial Tharsis emplacement ($0.17\Delta T_{\text{Tharsis}} - 3.68$ km). The starting point for the shoreline is (96.40° W, 63.69° N).

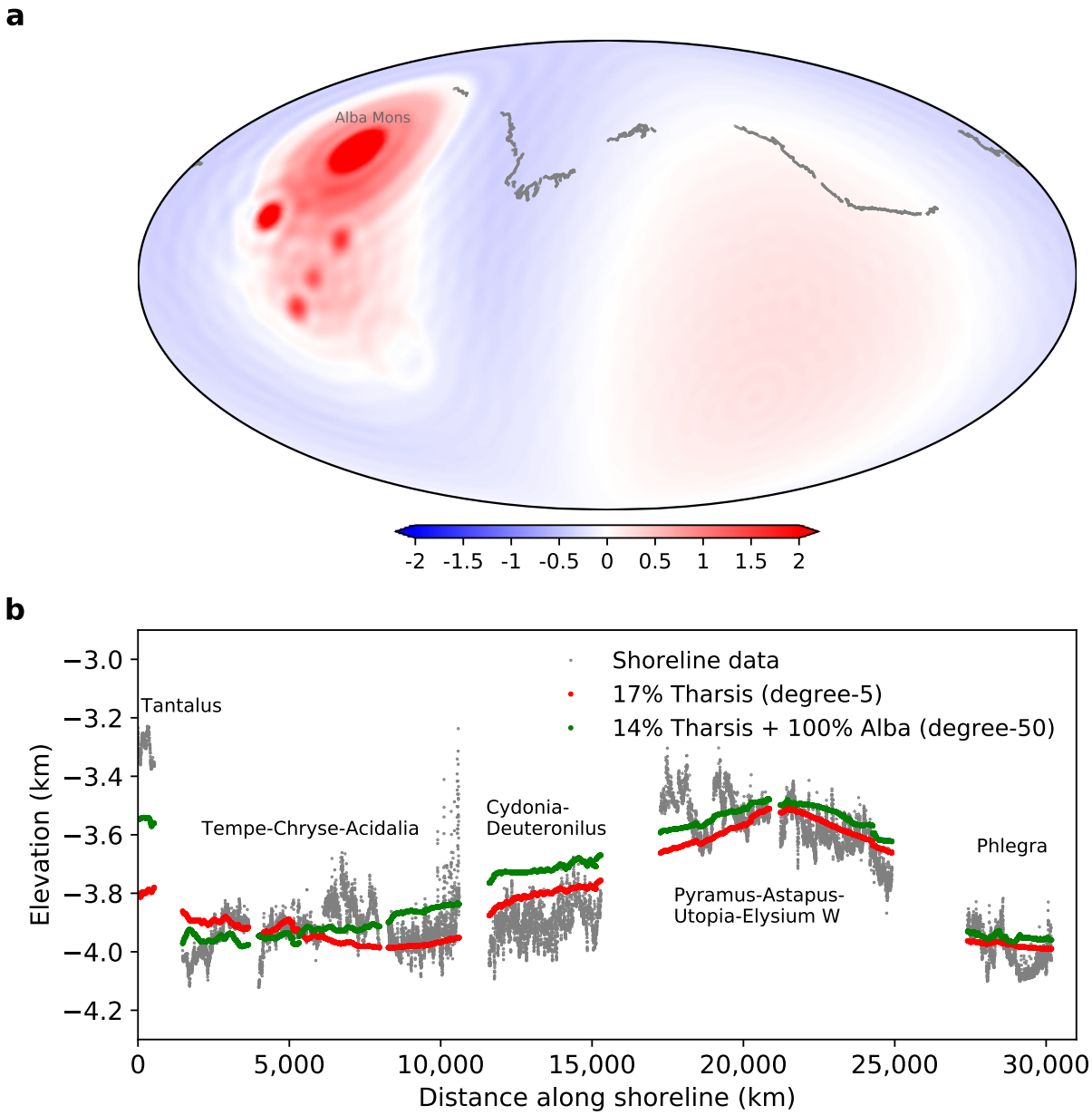

Figure 5.9: Degree-50 Tharsis deformation and Deuteronilus fit with full Alba Mons contribution. (a) Change in topography from 14% Tharsis deformation and 100% deformation from Alba Mons, using the degree-50 Tharsis model based on the gravity fit from J. Keane. The Deuteronilus shoreline is shown in grey. (b) Current Deuteronilus shoreline topography (Ivanov et al., 2017) compared to the degree-5 Tharsis fit (red line, $0.17 \cdot \Delta T_{\text{Tharsis}} - 3.68$ km) and the degree-50 Tharsis fit with 100% contribution from Alba Mons ($0.14 \cdot \Delta T_{\text{Tharsis}} + 1.0 \cdot \Delta T_{\text{Alba}} - 3.6$ km).

during the late stages of Tharsis growth. Furthermore, each segment of the Deuteronilus shoreline, which spans the interior of the entire lowland basin, displays similar morphologies, and the geological units just interior of the shoreline have similar ages (Ivanov et al., 2017). The simplest explanation for contacts of such similar morphology and age, and spanning such vast distances yet still following a late-Tharsis equipotential, is that the contact was formed by an ancient Martian ocean and represents an ancient shoreline.

5.7 Isidis shoreline

The Isidis shoreline displays morphologies very similar to that of the Deuteronilus shoreline, suggesting it formed by the same process, except that it is dated to 3.5 Gyr, 100 Myr younger than Deuteronilus (Ivanov et al., 2017). Because of its similar morphology and age to the Deuteronilus shoreline, we attempt to fit the Isidis shoreline to the same amount of Tharsis deformation (17%) as we used to fit the Deuteronilus shoreline. This represents the maximum Tharsis deformation expected for the Isidis shoreline. However, as shown in Figure 5.10c, the Isidis shoreline does not follow the expected topographic profile predicted by Tharsis deformation. The Isidis shoreline, like the entire Isidis basin, is tilted so that its northeast rim is higher in elevation than the southwest rim. This is opposite the tilting expected from Tharsis, which would have lifted the southwest rim more than the northeast rim (see also Figure 5.5). While this appears contradictory, the mismatch is possible if Isidis was tilted to its present orientation by loading of the Utopia basin, which is a proposed mechanism for explaining the present-day tilt of Isidis (McGowan and McGill, 2006). Loading of the Utopia basin is expected based on observations of sediment and lava deposits in the basin, and the large gravity anomaly indicating that it contains excess infill (Sjogren, 1979; Zuber et al., 2000). McGowan and McGill (2006) show that loading of Utopia could have tilted Isidis to an even greater extent than currently observed. Therefore, some amount of reverse tilting (as our model of Tharsis deformation predicts) is possible.

We test if loading of Utopia could explain the topography of the Isidis shoreline using the same plate flexure model employed for our analysis of Isidis loading (Section 5.3.3). We place a load of radius 950 km centered on Utopia (110.79°E, 42.29°N), and assume a T_e of 100km and load density of 2900 kg m^{-3}. The load is Gaussian in shape (to avoid the ringing in the spherical harmonics generated when using caps of constant thickness with sharp edges, as seen in Figure 5.3d), and has an average thickness of ∼3.5 km (less than the 18 km of excess fill estimated by Searls et al. (2006), and a total mass of $\sim 7.3 \times 10^{17}$ kg. This is more material than the $\sim 4.4 \times 10^{17}$ kg of material used to fit the Utopia gravity anomaly in the degree-50 fit by J. Keane, however, the fit from J. Keane used a T_e value of 50 km, which would allow a smaller load to produce a larger amount of flexure. The load distribution and resulting plate flexure are shown in Figure 5.10. The peripheral bulge caused by flexure from Utopia loading is greater in magnitude on the northeast rim of Isidis, tilting Isidis to the southwest. This tilting from Utopia loading can explain the topography of the Isidis shoreline, even when reverse tilting due to 17% Tharsis deformation is also considered (Figure 5.10c).

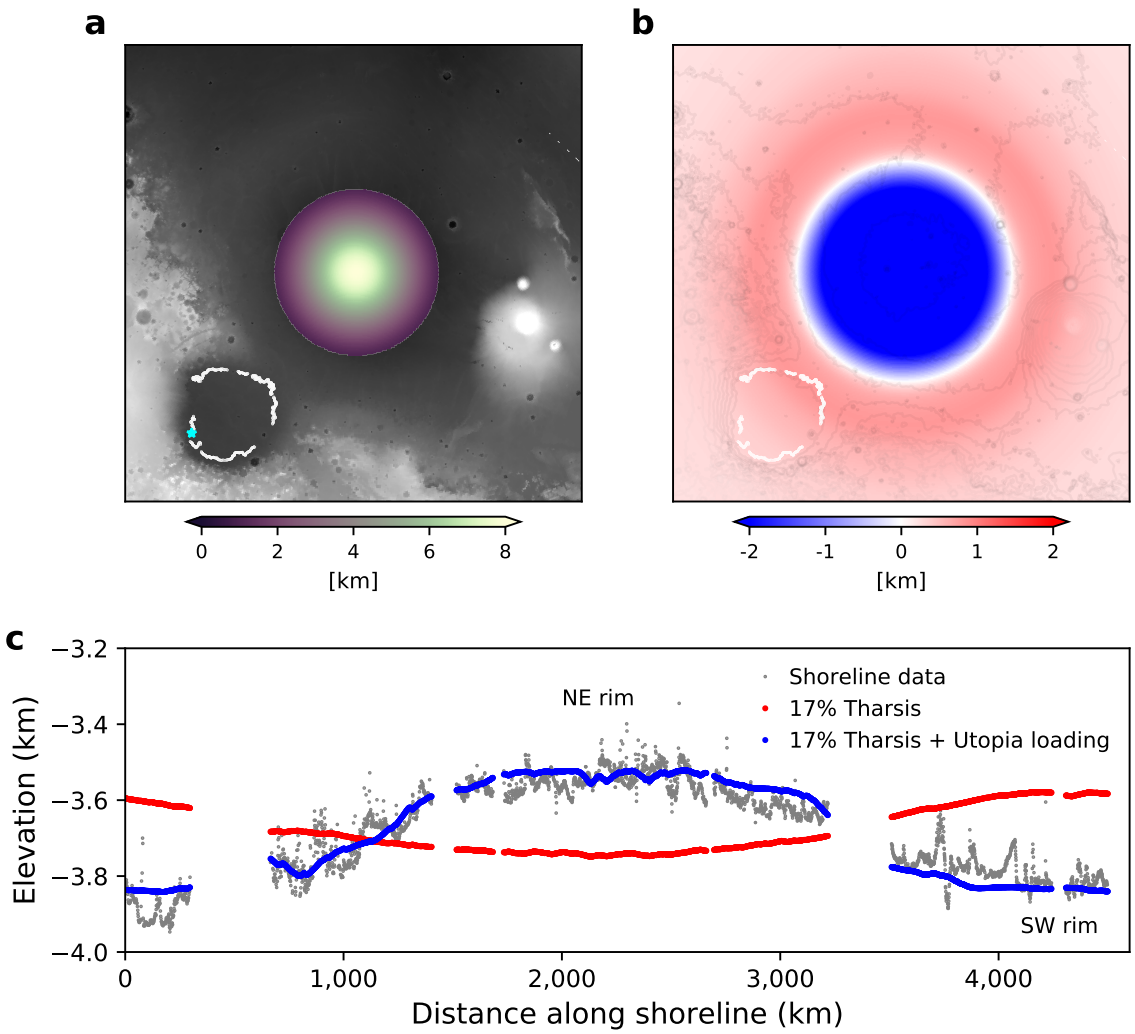

Figure 5.10: Isidis shoreline topography compared with deformation from Tharsis and Utopia loading. (a) Heat map of the load used in the Utopia loading model, which is a gaussian cap centered on the Utopia basin. Background greyscale is Mars topography, and the Isidis shoreline is plotted in white (data from Ivanov et al. (2017)). (b) Topographic response to flexure from the load in (a). A clear peripheral bulge is seen, overlapping the NE corner of the Isidis shoreline (plotted in white). Background contours show Mars topography. (c) Comparison of Isidis shoreline elevation data (grey dots, data from Ivanov et al. (2017) with deformation from late stage Tharsis deformation (red line, $0.17\Delta T_{\text{Tharsis}} - 3.95$ km) and deformation from both Tharsis and Utopia loading (blue line, $0.17\Delta T_{\text{Tharsis}} + \Delta T_{\text{Utopia}} - 4.55$ km). The distance along the Isidis shoreline is measured clockwise from the SW segment of the shoreline (marked as a cyan star in (a)).

Because flexure from Utopia loading causes significant uplift, the best-fit sea-level prior to Tharsis and Utopia deformation is -4.55 km, ∼1km less than the best-fit Deuteronilus sea-level. Perhaps the Isidis shoreline was formed at a lower level than Deuteronilus because it was geographically unconnected to the Deuteronilus ocean or because it is younger and sea-level decreased by the time of its emplacement. Alternatively subsequent loading of the Isidis basin could have displaced the shoreline downwards, similar to the displacement of the circum-Isidis segment of the Arabia shoreline, and accounting for this might recover an original sea-level closer to the Deuteronilus shoreline level.

The timing of Utopia loading relative to the subsequent Tharsis deformation is irrelevant provided that Utopia loading also occurred after the Isidis shoreline formed. Loading of Utopia likely occurred after the Isidis shoreline formed because a shrinking Martian ocean would evaporate from the Utopia basin last, depositing the non-volatile component of the ocean there. The deposits in the Utopia basin date to the early Amazonian (<3-3.46 Ga) (Werner and Tanaka, 2011; Tanaka et al., 2014), after the emplacement of the Isidis shoreline. The eastern portion of Utopia also contains volcanic deposits from Elysium that date to the Amazonian (Tanaka et al., 2014), which could also contribute to loading. Water loading/unloading of Utopia is insufficient to explain Isidis' tilt (McGowan and McGill, 2006). Therefore, deposition of material from a receding liquid, muddy, or frozen ocean, in addition to volcanic deposits, are a likely explanation for the tilt of the Isidis basin and its shoreline, even if some reverse tilting is caused by deformation due to Tharsis.

5.8 Effect of elastic lithosphere thickness

One source of uncertainty in our model is the assumed elastic lithosphere thickness; a thinner or thicker T_e would alter the deformation due to Tharsis (and TPW) because the Love numbers used to compute Mars' deformation would change. The gravity and shape coefficients we use to compute Tharsis topography are based on an assumed $T_e = 58$ km, the expected value at the time of Tharsis loading from Matsuyama and Manga (2010). However, the estimation of T_e by Matsuyama and Manga (2010) yields a 90% confidence interval with a minimum and maximum of 26 and 92 km, respectively. To estimate the effect of $T_e = 26$ or 92 km on deformation due to Tharsis, we recompute Tharsis' gravity and shape coefficients following the method in Matsuyama and Manga (2010). Using a fixed Tharsis center location (258.6° E, 9.8° N), Matsuyama and Manga (2010) compute the degree-2 gravity coefficients of Tharsis using a minimization technique with four unconstrained model parameters (T_e, non-dimensional Tharsis load Q, paleopole colatitude θ_R, and paleopole longitude ϕ_R), where the paleopole corresponds to the axis of rotation when the fossil (remnant) bulge was formed. This results in probability density functions for each unconstrained parameter, with the weighted averages (expected values) used to compute the gravity and shape coefficients. We redo this analysis, as described in Section 5 of Matsuyama and Manga (2010), but with T_e treated as a *constrained* parameter. This allows us to estimate the expected values of Q, θ_R, and ϕ_R for a given value of T_e. We find that for $T_e = 26$ km, $\bar{Q} = 3.95$, $\bar{\theta}_R = 17.9°$, and

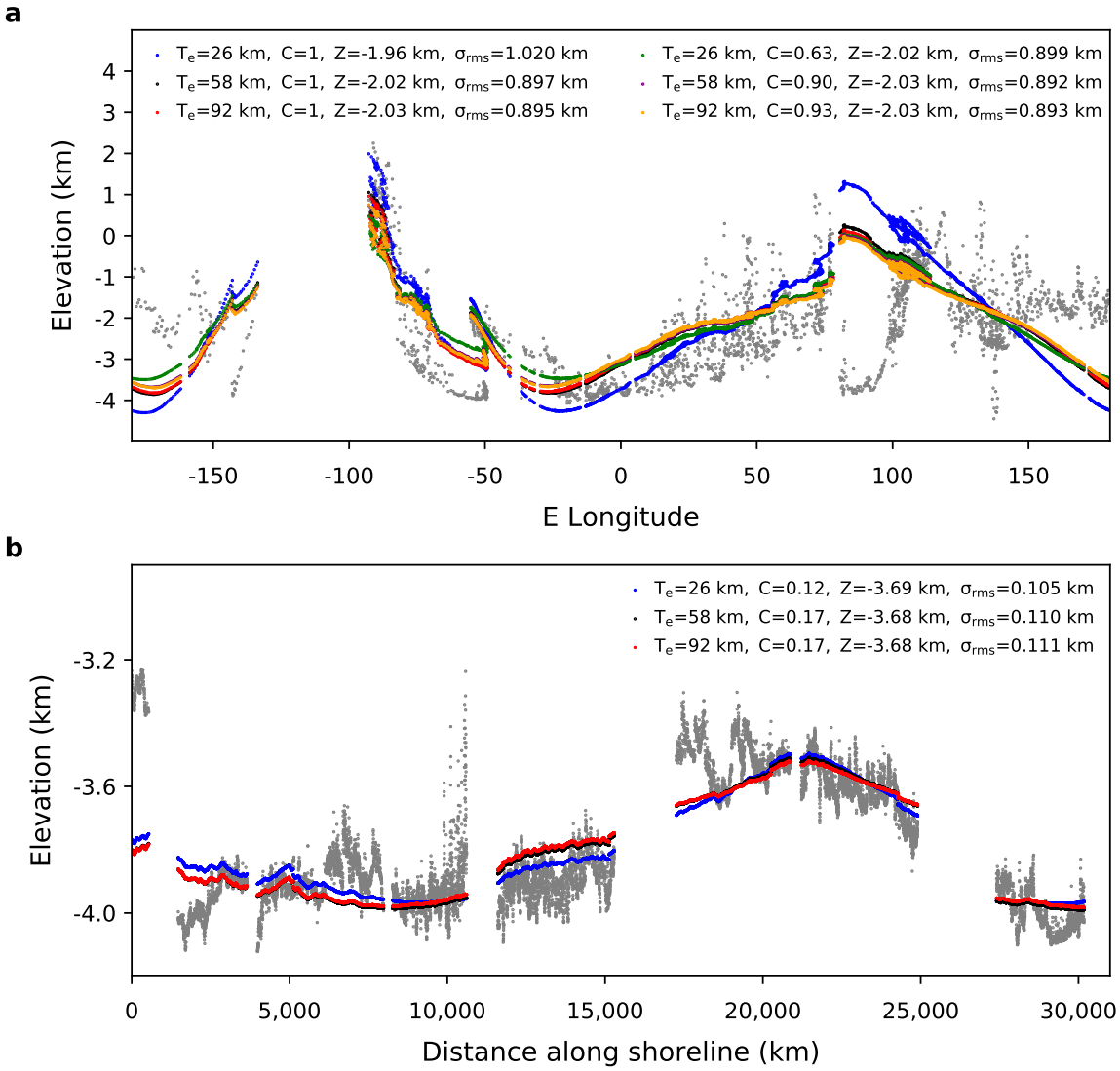

Figure 5.11: Effect of elastic lithosphere thickness on deformation due to Tharsis. (a) Current Arabia shoreline topography compared to displacement due to Tharsis deformation ($C \cdot \Delta T_{\text{Tharsis}} + Z$). Tharsis gravity and shape coefficients are computed separately for T_e = 26, 58, and 92 km, which each yield a corresponding best-fit offset Z and error σ_{rms}. For each T_e for the Arabia shoreline, we construct a fit both fixing C=1 (pre-Tharsis formation) and allowing C to vary (early-Tharsis formation). The circum-Isidis shoreline data was excluded when computing the fit and σ_{rms}, because the Isidis loading needed to explain the circum-Isidis shoreline deformation was not included in these deformation profiles. (b) Deuteronlius shoreline topography compared to the best-fit displacement due to Tharsis loading ($C \cdot \Delta T_{\text{Tharsis}} + Z$) for T_e = 26, 58, and 92 km.

$\bar{\phi}_R = 259.1°$. For $T_e = 92$ km, $\bar{Q} = 1.57$, $\bar{\theta}_R = 14.2°$, and $\bar{\phi}_R = 259.3°$. Tharsis' degree-2 gravity coefficients are recomputed using these values. The degree 3 to 5 gravity coefficients of Tharsis are computed from minimization against the observed degree 3 to 5 gravity coefficients, and are therefore not dependent on T_e. Shape coefficients for Tharsis are computed up to degree-5 following Section 7 of Matsuyama and Manga (2010). We compute the load Love numbers using the ALMA code (Spada, 2008), with a five-layer model as described in Matsuyama and Manga (2010).

We construct new best-fit deformation profiles for $T_e = 26$ and 92 km, using the same technique described in Section 5.3.2, but with the corresponding Tharsis gravity and shape coefficients that we computed for each T_e. The best fit profiles for $T_e = 26$ and 92 km are compared with the nominal $T_e = 58$ km profiles in Figure 5.11. Decreasing T_e changes the overall amplitude of the expected Tharsis deformation, however, if the amplitude becomes too high it compensated by lowering the percentage of Tharsis deformation used in the fit (*i.e.*, assuming the shoreline form further after the initiation of Tharsis' growth). As seen in Figure 5.11, all best-fit profiles are relatively similar, showing that changes in T_e do not have a significant effect on our conclusions.

All models we examine use a constant elastic lithopshere thickness. While this assumption yields topographic deformation profiles that fit most of the shoreline data, spatial variations in T_e are a possible cause of some of the deviations between the data and our model fits. Spatial variations in lithospheric thickness (*e.g.*, Grott and Breuer, 2010) would allow for non-uniform responses to phenomena such as Tharsis deformation, TPW, and plate flexure. Some of the largest variations in T_e could occur across the dichotomy boundary, due to the large change in crustal thickness (Thiriet et al., 2018), and potentially around Tharsis, where enhanced heat-flux from the Tharsis super-plume may have resulted in a thinner sub-Tharsis lithosphere during Tharsis' growth. Computing deformation with a non-uniform T_e is out of the scope of this work and is poorly constrained, but could be considered in future studies.

5.9 Effect of ocean loading

Another potential source of error in our model is the effect of ocean loading on the shoreline elevations. Although Perron et al. (2007) found that plate flexure due to loading of the ocean basin should not significantly affect shoreline elevations, their analysis was for T_e=200km, whereas we use T_e=58km. The ocean basin resulting from our analysis also has less volume and a different shape, because we subtract Tharsis topography, which has a negative component in much of the Borealis basin. To compute plate flexure due to ocean loading, we expand the surface density of the ocean load in spherical harmonics and compute the associated displacement using the method described in Section 5.3.3 with a load density of 1000 kg m^{-3} and T_e=100km. For the Arabia ocean, the ocean load is computed by subtracting the pre-Tharsis topography of Mars from the best fit Arabia ocean elevation ($Z = -2.3$km). The pre-Tharsis Martian topography is computed by subtracting the deformation due to Tharsis and TPW (Equations 5.2 and 5.1) from Mars' current topography (1/4 degree per

pixel gridded MOLA data from Smith et al. (2003)). For the ocean level corresponding to the Deuteronilus and Isidis shorelines, only 17% of deformation due to Tharsis was subtracted from Mars' current topography, and the ocean elevation Z was set to -3.68 km and -3.95 km, respectively. The loaded shoreline topography is compared to the unloaded topography in Figure 5.12. The mean magnitude of deflection is 151 m for the Arabia shoreline, 55m for the Deuteronilus shoreline, and 24m for the Isidis shoreline. Deformation of the shorelines due to unloading of the ocean basin does not appear to have a significant effect on shoreline topography (Figure 5.12). This is likely because the oceans are shallow and have gradual slopes near most shoreline segments. Because the shorelines are by definition positioned at the edge of the ocean load, they experience little deflection from subsidence (which is larger towards the center of the ocean basins) or the peripheral flexural bulge (which is larger further away from the edge of the ocean load).

5.10 Ocean volume estimates

We estimate the volume of water that filled the northern plains to the Arabia and Deuteronilus shorelines by subtracting the relevant Tharsis contribution to Mars' topography to estimate the topography at the time of shoreline emplacement, and filling the lowlands to shoreline elevation (Figure 5.13). For the Arabia ocean, we subtract 100% of Tharsis' contribution to Mars' topography, and use a sea-level of -2.3km (Section 5.5). For the Deuteronilus shoreline, we subtract 17% of Tharsis deformation and use a sea-level of -3.68km (Section 5.6). For present-day Mars topogrpahy we use the 1/4 degree per pixel gridded MOLA data (Smith et al., 2003). For a pre-Tharsis Arabia ocean we estimate a volume of $\sim 4 \times 10^7$ km^3. For the late-Tharsis Deuteronilus ocean we estimate a volume of $\sim 1.2 \times 10^7$ km^3. These are lower limits because we do not remove excess terrain, such as Elysium, polar deposits, lava/sediment basin deposits, and short-wavelength Tharsis topography. Deflection of the sea floor by the ocean load could also allow a larger volume of water to fill the basin to shoreline level. We compute the extra water volume allowed due to deflection of the sea floor by ocean loading, and find that the Arabia ocean could contain an additional $\sim 4.5 \times 10^6$ km^3 and the Deuteronilus ocean could contain an additional $\sim 1.9 \times 10^6$ km^3 (using the thin plate flexure model described in Section 5.3.3 with T_e=100km, as in Section 5.9). The computed Arabia ocean volume negligibly increases if instead of pre-Tharsis formation we assume an early-Tharsis Arabia ocean, corresponding to shoreline emplacement after 10% of Tharsis deformation was complete (see Section 5.8 and Figure 5.11). See Table 5.10 for a comparison of ocean volume estimates.

The Arabia and Deuteronilus ocean volumes correspond to a Global Equivalent Layer (GEL – thickness of water layer if the ocean volume was spread uniformly over the Martian surface) of 273m and 83m, respectively (304m and 96m if the additional ocean depth due to deflection by the ocean load is included). The ocean volumes we compute are somewhat less than prior estimates. For example, Ruiz et al. (2006) computed a GEL of 610-850m for the Arabia ocean and a GEL of 140-190m for the Deuteronilus ocean (assuming present-

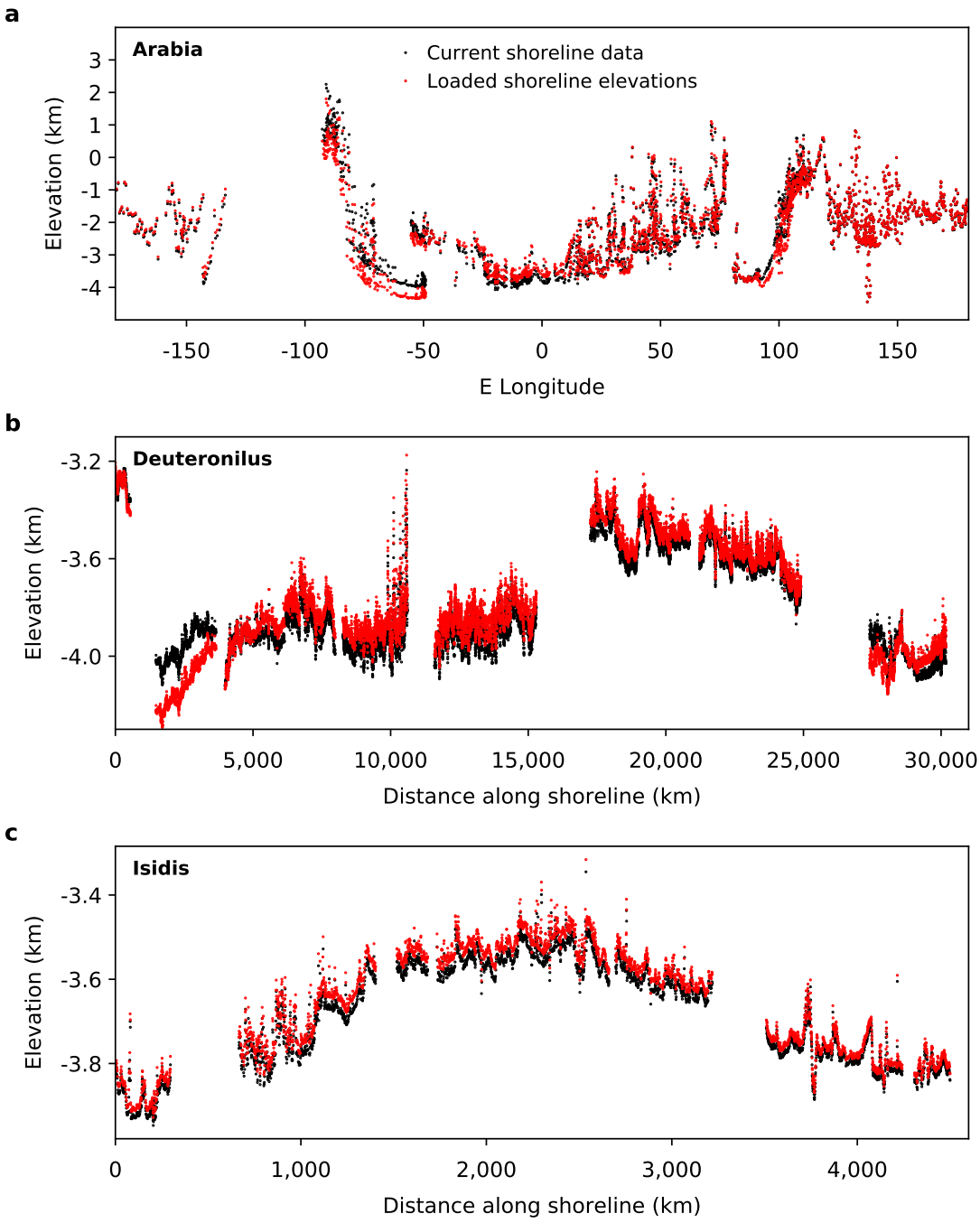

Figure 5.12: Effect of plate flexure due to ocean loading on shoreline topography. Current shoreline elevations are plotted against displaced elevations for (a) Arabia shoreline, (b) Deuteronilus shoreline, and (c) Isidis shoreline.

day topography for the lower limits and water-loaded topography for the upper limits). Di Achille and Hynek (2010) propose an Arabia ocean sea-level of -2.54km, based on the mean present-day elevations of open deltas, resulting in an Arabia ocean GEL of 445m (assuming present-day topography). We compute lower ocean volumes because the Tharsis deformation we subtract to compute the topography at the time of shoreline emplacement is negative in much of the area enclosed by the northern ocean basins (Figures 5.3 and 5.5), resulting in shallower oceans for pre- or mid-Tharsis Mars topography.

Lower ancient Martian ocean volumes are significant because the large ocean volumes estimated by prior studies have been used as an argument against the existence of ancient Martian oceans, because of the claim that it would be difficult to explain the loss of such a large volume of water from the martian surface (*e.g.*, Carr and Head, 2015). Recent observations suggest only about a 23m GEL of water could have been lost to space via atmospheric escape since the Noachian (Jakosky et al., 2018), although this amount might increase if more efficient mechanisms of Mars atmospheric water loss are considered (*e.g.*, Shaposhnikov et al., 2019). However, Weiss and Head (2017) suggest that 200m GEL of water could be trapped in present-day cryosphere. Additionally, (Chassefière et al., 2013) estimate that serpentinization could have removed 330-1030m GEL of water during the Noachian. This is supported by Wade et al. (2017), which find that a significant amount of water could have been sequestered into the Martian crust, which can hold more water per unit volume compared to Earth's crust. While the amount of water lost to space and sequestered in the crust and cryosphere is uncertain, more accurate estimates of ocean volumes at various times in Martian history can better constrain the necessary rate of water loss. Although the largest ocean volume we compute (304m GEL for the Arabia ocean with ocean loading) is a lower limit (we don't remove excess topography), it is within conservative estimates of water loss (23m GEL to space, <200m GEL in the cryosphere, and <330m GEL into the crust).

Table 5.3: Ocean volume estimates

	Arabia (pre-Tharsis)	Arabia (early-Tharsis)	Deuteronilus (late-Tharsis)
Percent Tharsis emplaced prior to shoreline*	0%	10%	83%
Ocean volume† (10^7 km^3)	4-4.4	4-4.5	1.2-1.4
GEL† (m)	273-304	280-310	83-96
Mean ocean depth (km)	0.96	1.0	0.55
Maximum ocean depth (km)	5.1	4.7	3.2

* Early- and late-Tharsis topography is based on the best-fit deformation profiles for T_e=58km, see Figure 5.12.

† Lower limit: mid-Tharsis topography; Upper limit: mid-Tharsis topography plus sea floor subsidence from ocean loading.

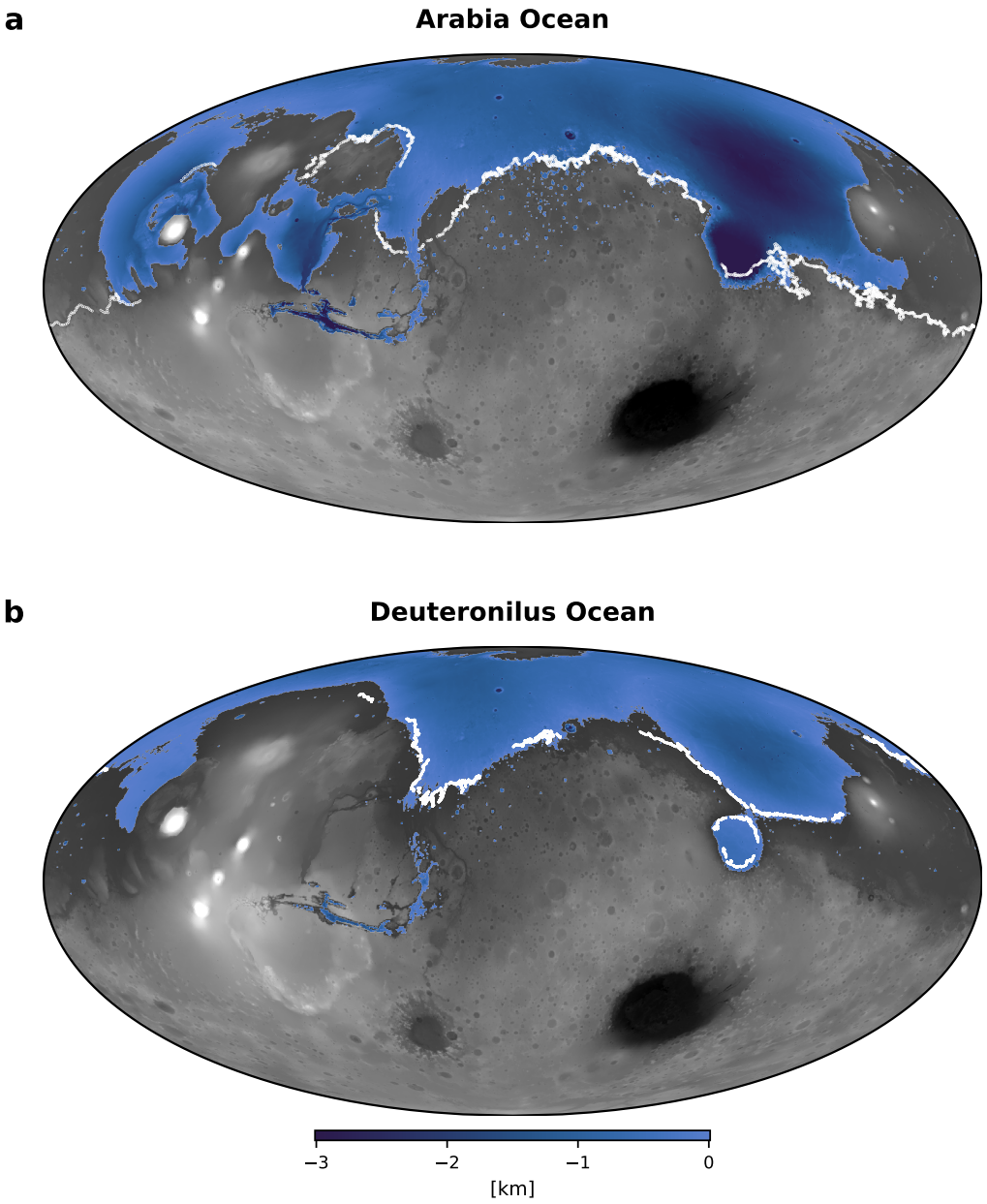

Figure 5.13: Extent of proposed Arabia and Deuteronilus oceans. (a) Arabia ocean depth is overplotted on pre-Tharsis Mars topography (MOLA topography minus Tharsis deformation), up to the best fit Arabia shoreline sea-level of -2.3 km. (B) Deuteronilus ocean depth is overplotted on late-Tharsis Mars topography (MOLA topography minus 17% Tharsis deformation), up to the best fit Deuteronilus shoreline sea-level of -3.68 km. The shorelines are plotted in white. Short-wavelength Tharsis topography remains in (a) because the subtracted Tharsis topography is only modeled up to degree-5.

5.11 Discussion

5.11.1 Model limitations

Deficiencies in the Tharsis model were discussed in Section 5.5. The model of Tharsis deformation can be improved, including removing short wavelength Tharsis topography and considering varying elastic lithosphere thickness. Loading due to infill of Isidis and Utopia may also cause shoreline deflection, as could loading from Elysium. Models of flexure due to such loads requires further refinement and is a work in progress. Other volcanic deposits and infill of other basins could also cause local shoreline deflection, but likely of less magnitude than Isidis, Utopia, and Elysium.

In addition to Tharsis and other surface loads, several other short and long wavelength processes could have deformed the shorelines in the >3.5 Gyr since their emplacement, including dynamic topography from mantle plumes (*e.g.*, Roberts and Zhong, 2004), lithospheric deformation (Ruiz et al., 2004, 2006), glacial erosion (Davila et al., 2013), and plate flexure from other loads not yet considered (such as the polar deposits). Loads like the polar deposits could also have induced a small amount (<2°) of post-Tharsis TPW (Kite et al., 2009). Plate flexure associated with impact basin formation could also deform shorelines. While basins >1000 km in diameter pre-date the Deuteronilus shoreline, some basins may have been coincident with or post-date the Arabia shoreline.

Short wavelength misfit may also be a consequence of the difficulty in identifying the shorelines themselves (Ivanov et al., 2017).

5.11.2 Shoreline identification

Whether or not the features we have assumed are shorelines are in fact shorelines is the subject of much debate. The original Arabia contact was mapped in Viking Orbiter images (Parker et al., 1989, 1993). More recent analysis using high resolution imagery from more recent missions has cast doubt on the identification of these proposed geological contacts as shorelines (Sholes et al., 2019; Rivera-Hernández and Palucis, 2019). However, a portion of the Arabia contact in southern Isidis has been recently reexamined and found to contain several possible coastal features (Erkeling et al., 2012). Overall, paleoshorelines are difficult to identify in orbital imagery (Clifford and Parker, 2001), and it is unclear what a shoreline emplaced 3.5−3.9 Ga should look like at present, after >3.5 Gyr of erosional processes. Shorelines could be eroded by and confounded with tsunami deposits (*e.g.*, Costard et al., 2017; Rodriguez et al., 2016) and subsequent glaciation (*e.g.*, Davila et al., 2013). The proposed Arabia shoreline in particular is highly degraded and has not been recently remapped.

Some characteristic segments of the original mapping of the Arabia shoreline are shown in Figure 5.14. Features along the proposed coastline include cliffs, degraded downslope crater rims, and differences in thermal inertia that might indicate a change in the underlying geological unit. The original shoreline mapping displays some offset from these features due

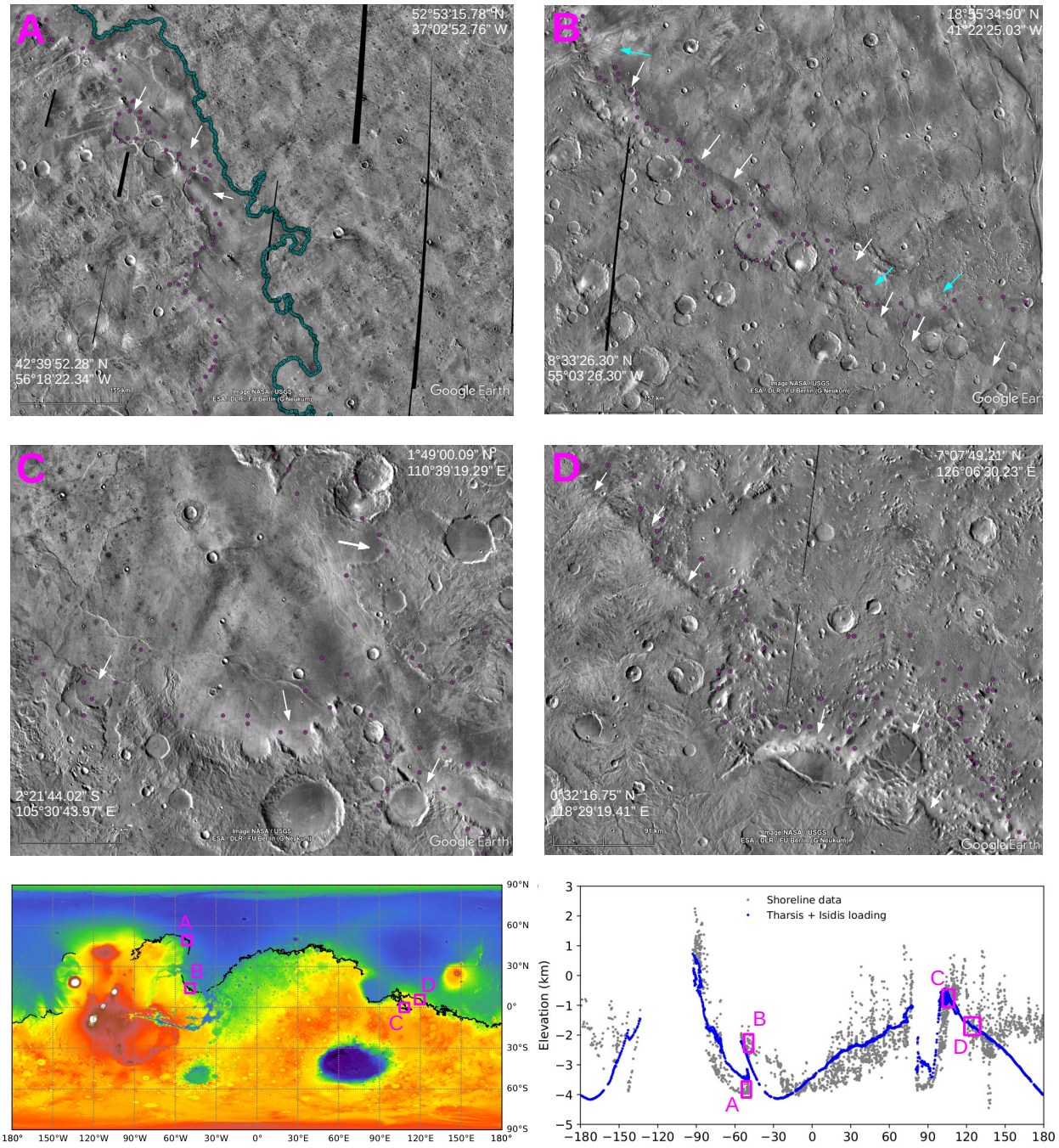

Figure 5.14: Arabia shoreline segments in THEMIS Daytime IR. Locations of insets A, B, C, and D are shown in the topography map and shoreline elevation and deformation profile (as in Figure 5.7). Caption continued on following page.

Figure 5.14: The Arabia shoreline as mapped by Clifford and Parker (2001) is plotted as magenta points. Because the Arabia shoreline mapping of Clifford and Parker (2001) was conducted on very early orbital imagery, it does not always exactly follow the topography visible in the more recent THEMIS data, however, it does roughly coincide with some potential features such as changes in thermal inertia (deposits?), cliffs, and degraded downslope crater rims. White arrows point upslope to possible contacts (changes in thermal inertia) and craters with eroded downslope rims and infill. (A) The Arabia segment in NE Tempe Terra. The Deuteronilus shoreline (Ivanov et al., 2017) is also plotted in cyan dots. The region to the east of the Deuteronilus shoreline is the VBF, displaying a distinct change in THEMIS daytime IR. (B) SE Chryse segment. The cyan arrows point to a Maja Valles outflow channel in the upper left and the Sabrina fan and the Hypanis Valles delta in the lower right (Fawdon et al., 2018). The shoreline mapped between these features follows thermal inertia differences, possible cliffs, and craters with degraded downslope rims. Maja Valles likely post-dates the shoreline, however. (C) Segment of the Arabia shoreline mapped in Amenthes Planum extending SE from the Isidis. (D) Arabia segment mapped in Nepenthes Mensae, with white arrows showing proposed cliffs. Images are constructed using Google Earth Pro with THEMIS daytime IR data. The latitude and longitude of of the lower left and upper right of each image are labeled on the corresponding corners.

to the updated imaging techniques, but loosely follows these types of features. While in isolation these features do not provide support for a coastal formation mechanism (craters with degraded downslope rims are seen flanking mare filled basins on the Moon, for example), what is intriguing is the global nature of these features along the northern lowland basin, and the coincidence of potential coastal features with deltas and valley network termini (Chan et al., 2018). Figure 5.14b shows several deltas coincident with the proposed Arabia shoreline, including the Hypans Valles delta (Fawdon et al., 2018). Additionally, we argue that the coincidence of theses features with paleo-equipotential surfaces supports the hypothesis that they are coastal in origin.

Still, it is unclear if all of the Arabia shoreline segments originally mapped constitute the same shoreline. For example, the Arabia shoreline was originally mapped around Amenthes Planum (extending SE from Isidis), but more recent examination of this region suggests a Hesperian-Amazonian age for this unit (Erkeling et al., 2011). Additionally, the section of the Arabia shoreline extending from Gale crater to Tharsis has a large misfit to the Tharsis deformation model. It is possible the contact in this region may have been mismapped and represents either a different ocean level or a different formation mechanism. More accurate dating of proposed Arabia shoreline segments could determine if they were emplaced over a similar time period. Accurate dating of the Arabia shoreline is also necessary to determine whether the shoreline formed prior to or during the early stages of Tharsis' growth. Formation of the Arabia shoreline after some limited early Tharsis growth is suggested by Arabia segments that border Acheron Fossae and Tempe Terra (Clifford and Parker, 2001), two of the oldest Tharsis units, which are located well north of the expected pre-

Tharsis dichotomy boundary. However, it is possible that the Archeron Fossae and Tempe Terra contacts were misidentified as belonging to the Arabia shoreline, or that the Arabia shoreline initially followed the pre-Tharsis dichtomy boundary, and formed the Tempe Terra and Archaeon Fossae contacts only after early Tharsis uplift and deposition.

In contrast to the Arabia shoreline, the Deuteronilus shoreline was recently remapped with high-accuracy, as discussed in Section 5.2.2. It displays a range of similar geomorphologies, and distinct thermal signature (as seen in Figure 5.14a), across the full extent of the shoreline interior of the dichotomy boundary, and distinct segments are shown to have similar ages (Ivanov et al., 2017). Similar remapping and dating of other shoreline segments may help reconstruct the history of shoreline formation and modification. Several potential shorelines identified by Clifford and Parker (2001), such as the Ismenius, Acidalia, Elysium, Aeolis, and Meridiani contacts, have been relatively unexamined due to their high degree of discontinuity (Carr and Head, 2003b). A re-evaluation of shorelines with full consideration of the various deformation processes may enable the development of a chronology of oceans on Mars. In particular, the Meridiani shoreline (Edgett and Parker, 1997; Clifford and Parker, 2001) may pre-date the Arabia shoreline and have contained a larger volume of water (Ruiz et al., 2006).

5.11.3 The Mars ocean hypothesis revisited

As discussed in Section 5.2.1, the main arguments against an ocean are primarily based on geology, geochemistry, atmospheric modeling, and water volume estimates. While the geological evidence for shorelines is still controversial, our result that paleoshorelines correspond to paleo-equipotential surfaces supports the hypothesis that the proposed contacts represent the boundaries of ancient oceans. The timing of these equipotentials before and coincident with Tharsis formation might resolve several other arguments against oceans.

From the climate perspective, atmospheric models struggle to explain how early Mars could have been sufficiently warm for oceans to remain stable (*e.g.*, Wordsworth, 2016), however, the effect of Tharsis on ocean stability has been under-explored. The decline in ocean volume from the pre- or early-Tharsis Arabia shoreline to the late-Tharsis Deuteronilus shoreline suggests that Tharsis volcanism played a critical role in the evolution of a Martian ocean. Outgassing from Tharsis could have contributed to either heating (Halevy and Head, 2014) or cooling (Tian et al., 2010) the planet. If the Arabia and Deuteronilus shorelines represent different highstands of the same ocean, then it is possible a large ocean was in place before Tharsis volcanism initiated, and shrank as Tharsis volcanism cooled the planet, or that an ocean arose as a result of heating caused by Tharsis outgassing and decreased in volume as Tharsis volcanism declined. Given the difficulty in maintaining warm climates on early Mars, it is perhaps more likely the Arabia and Deuteronilus shorelines represent different oceans that were stable during transient periods of warming due to intense Tharsis activity. In this scenario, the Arabia ocean would coincide with early Tharsis activity and the formation of the valley networks (Bouley et al., 2016), and the Deuteronilus ocean would coincide with late Tharsis activity and the many outflow channels bordering the northern

plains, as suggested by each shoreline's respective equipotential surface. Other proposed shorelines may represent distinct briefly stable oceans during periods of heightened Tharsis outgassing. After Tharsis was mostly emplaced $\sim$ 3.6 Ga, only short-lived lakes may have been stable (Kite et al., 2017), although a Late Hesperian/Early Amazonian ocean has also been suggested based on evidence of tsunamis (Rodriguez et al., 2016; Costard et al., 2017).

From a geochemical perspective the evidence for a northern ocean is ambiguous, and there is a notable lack of carbonate deposits in the northern plains that has been used as evidence against martian oceans (Pan et al., 2017). However, oceans supported by the degassing of sulfur from Tharsis could explain the lack of carbonate deposits observed in the northern plains, because volcanically degassed sulfur can inhibit carbonate formation (Halevy et al., 2007; Halevy and Schrag, 2009). Finally, the water budget issue was discussed in Section 5.10; given recent estimates of water loss to space and sequestration into the crust and cryosphere, combined with the shallower ocean volumes we compute (due to pre-Tharsis topography), there does not seem to be a large disagreement between constraints on water loss and ocean volume estimates.

Still, much work remains to be done in resolving the Mars ocean hypothesis. Further geological investigations are necessary to resolve the classification of the contacts as shorelines, and it is possible the identification of the contacts as coastal features will be disproven. The stability of oceans must also be resolved with atmospheric models that still predict a cold early Mars, and with a lack of geochemical evidence for ocean deposits.

5.12 Conclusions

The evolution of water on Mars is critical to understanding the past climate and habitability of the planet. While shorelines on Mars have provided compelling evidence for a Martian ocean, explaining their deviations from an equipotential has been a challenge. We show that the topography of Martian shorelines can be quantitatively explained by deformation due to the emplacement of Tharsis and resulting TPW (in the case of the Arabia shoreline) or by the latter stages of Tharsis emplacement (in the case of the Deuteronilus shoreline). Formation of the Arabia shoreline prior to (or during the early stages of) Tharsis emplacement suggests that the Arabia ocean was concurrent with valley network incision (Bouley et al., 2016), which likely occurred as part of a globally active hydrosphere capable of supporting such an ocean (Di Achille and Hynek, 2010). The consistency between the topography of the Martian shorelines, their age, and the chronology of topographic changes due to Tharsis emplacement and associated TPW, suggests that the Arabia and Deuteronilus contacts are evidence that Martian oceans existed, and were present earlier than previously thought.

5.13 Acknowledgements

We thank G. DiAchille for providing the data for the Arabia shoreline (originally from Clifford and Parker (2001)), and M.A. Ivanov for providing the data for the Deuteronilus and Isidis shorelines. We thank J. Keane for providing the new degree-50 gravity fit for Tharsis. We thank I. Matsuyama for discussions regarding this research. We thank M. Zuber and S. Bouley for constructive reviews of the published component of this work. R.C. and M.M. are supported by NASA grant 80NSSC19K0545.

Chapter 6

Outlook

In this dissertation, we examined several aspects of early Mars geodynamics, including superplumes, giant impacts, and planetary-scale deformation. Two of the most prominent geophysical features of early Mars are the crustal dichotomy and the formation of Tharsis, which both had a profound effect on Mars' subsequent evolution. In Chapters 2, 3, and 4 we examined the effects of a giant impact on the crust and subsequent evolution of the martian mantle. Giant impacts and mantle convection are often examined in isolation, and we have shown that a giant impact can strongly influence the subsequent geodynamic evolution of a terrestrial planet. In particular, we showed that a giant impact in one hemisphere can, somewhat counter-intuitively, result in superplume formation in the opposite hemisphere, due to the hemispheric difference in the distribution of heat-producing elements in the post-impact crust. This result highlights that the distribution and composition of crust can have a first-order effect on mantle evolution. We also explored the evolution of an early Mars superplume and its relation to subsequent crust production and the formation of Tharsis. Not all of our original hypotheses were shown to be feasible. We were not able to show that migration of a superplume could explain the formation of Tharsis or the magnetic lineations. Our simulations of an early Mars giant impact could not reproduce the shape and structure of the dichotomy boundary, highlighting the need for improved impact modeling potentially coupled to post-impact modification. Thus, while we have examined some early Mars geodynamic processes with a new perspective, many open questions remain. This is especially true of early martian oceans, which we examined in Chapter 5. Although we showed that proposed paleoshorelines can follow paleo-equipotentials deformed by Tharsis, the interpretation of geologic contacts as shorelines is still a matter of much debate. The Mars ocean hypothesis must also be reconciled with geochemistry and climate models. Still, we hope to have emphasized that the Mars topography observed today is not necessarily the topography of the Noachian or Hesperian. Large-scale processes have contributed to reshaping the planet, and greater understanding of those processes and the expected deformation can inform our interpretation of early martian geology and climate.

We will continue to update our models of early Mars geodynamics. Much work remains to be done regarding superplume evolution on early Mars and the origin of Tharsis. We will

also continue to improve our modeling of a giant impact on early Mars and the formation of the crustal dichotomy. We also plan to continue to update models of shoreline deformation by improving the estimated deformation from Tharsis and the examination of other surface loads.

While many open questions related to early Mars geodynamics remain, the wealth of data and ongoing missions make it an exciting period to study the planet. Current and future missions will provide groundtruth measurements and observations that can motivate, test, and constrain geodynamic models. In particular the Insight mission, the first dedicated geophysics mission to Mars, may constrain properties of the Mars crust, mantle, and core that can be used to better formulate models of Mars mantle convection. The upcoming Mars 2020 mission will land at Jezero crater and explore Noachian terrains, providing new information on Mars' ancient crust. Mars 2020 even plans to cache samples for eventual return to Earth, a prospect that could greatly improve our understanding of the planet's early evolution. JAXA's MMX mission will explore and return samples from Mars' largest moon Phobos, and determine if Mars' moons could have formed during an early giant impact. And while the Curiosity rover continues to explore the Hesperian paleolake environment of Gale crater, the upcoming Exomars mission will land at Oxia Planum, near the Arabia shoreline and a possible subaqueous delta.

Planetary science is an interdisciplinary endeavor, and geodynamic models are just one piece of the puzzle. We hope our geodynamic models can inform and be informed by other sub-disciplines of planetary science, such as geology, geochemistry, climatology, and hydrology. At the interfaces between these disciplines we may begin to better construct an understanding of the processes that shaped the early evolution of the planet Mars.

Bibliography

Acuna, M. H., Connerney, J. E. P., Ness, N. F., Lin, R. P., Mitchell, D., Carlson, C. W., McFadden, J., Anderson, K. A., Reme, H., Mazelle, C., Vignes, D., Wasilewski, P., Cloutier, P., 1999. Global Distribution of Crustal Magnetization Discovered by the Mars Global Surveyor MAG/ER Experiment. Science 284 (5415), 790–793.

Amit, H., Christensen, U. R., Langlais, B., 2011. The influence of degree-1 mantle heterogeneity on the past dynamo of Mars. Physics of the Earth and Planetary Interiors 189 (1-2), 63–79.

Anderson, R. C., Dohm, J. M., Golombek, M. P., Haldemann, A. F. C., Franklin, B. J., Tanaka, K. L., Lias, J., Peer, B., 2001. Primary centers and secondary concentrations of tectonic activity through time in the western hemisphere of Mars. Journal of Geophysical Research: Planets 106 (E9), 20563–20585.

Andrews-Hanna, J. C., Zuber, M. T., Banerdt, W. B., 2008. The Borealis basin and the origin of the martian crustal dichotomy. Nature 453 (7199), 1212–1215.

Baker, V. R., Strom, R. G., Gulick, V. C., Kargel, J. S., Komatsu, G., Kale, V. S., 1991. Ancient oceans, ice sheets and the hydrological cycle on Mars. Nature 352 (6336), 589–594.

Baratoux, D., Samuel, H., Michaut, C., Toplis, M. J., Monnereau, M., Wieczorek, M., Garcia, R., Kurita, K., 2014. Petrological constraints on the density of the Martian crust. Journal of Geophysical Research: Planets 119 (7), 1707–1727.

Basaltic Volcanism Study Project, 1981. Basaltic volcanism on the terrestrial planets. Pergamon Press, New York.

Bottke, W. F., Andrews-Hanna, J. C., 2017. A post-accretionary lull in large impacts on early Mars. Nature Geoscience 10 (5), 344–348.

Bouley, S., Baratoux, D., Matsuyama, I., Forget, F., Séjourné, A., Turbet, M., Costard, F., 2016. Late Tharsis formation and implications for early Mars. Nature 531 (7594), 344–347.

Bouley, S., Baratoux, D., Paulien, N., Missenard, Y., Saint-Bézar, B., 2018. The revised tectonic history of tharsis. Earth and Planetary Science Letters 488, 126–133.

Brasser, R., Mojzsis, S. J., 2017. A colossal impact enriched Mars' mantle with noble metals. Geophysical Research Letters 44 (12), 5978–5985.

Breuer, D., Plesa, A.-C., Tosi, N., Grott, M., 2016. Water in the Martian interior-The geodynamical perspective. Meteoritics & Planetary Science 51 (11), 1959–1992.

Canup, R., Salmon, J., 2018. Origin of Phobos and Deimos by the impact of a Vesta-to-Ceres sized body with Mars. Science Advances 4 (4).

Canup, R. M., Barr, A. C., Crawford, D. A., 2013. Lunar-forming impacts: High-resolution SPH and AMR-CTH simulations. Icarus 222 (1), 200–219.

Carr, M., Head, J., 2015. Martian surface/near-surface water inventory: Sources, sinks, and changes with time. Geophysical Research Letters 42 (3), 726–732.

Carr, M. H., Head, J. W., 2003a. Basal melting of snow on early Mars: A possible origin of some valley networks. Geophysical Research Letters 30 (24).

Carr, M. H., Head, J. W., 2003b. Oceans on Mars: An assessment of the observational evidence and possible fate. Journal of Geophysical Research 108 (E5), 5042.

Carslaw, H. S. S., J. C. Jaeger, Jaeger, J. C., 1959. Conduction of heat in solids, 2nd Edition. Clarendon Press, Oxford.

Chan, N.-H., Mitrovica, J. X., Daradich, A., Creveling, J. R., Matsuyama, I., Stanley, S., 2014. Time-dependent rotational stability of dynamic planets with elastic lithospheres. Journal of Geophysical Research: Planets 119 (1), 169–188.

Chan, N.-H., Perron, J. T., Mitrovica, J. X., Gomez, N. A., 2018. New evidence of an ancient martian ocean from the global distribution of valley networks. Journal of Geophysical Research: Planets 123 (8), 2138–2150.

Chassefière, E., Langlais, B., Quesnel, Y., Leblanc, F., 2013. The fate of early Mars' lost water: the role of serpentinization. Journal of Geophysical Research: Planets 118 (5), 1123–1134.

Cheung, K. K., King, S. D., 2014. Geophysical evidence supports migration of Tharsis volcanism on Mars. Journal of Geophysical Research: Planets 119 (5), 1078–1085.

Christensen, U., 1984. Convection with pressure-and temperature-dependent non-newtonian rheology. Geophysical Journal International 77 (2), 343–384.

Citron, R. I., Genda, H., Ida, S., 2015. Formation of Phobos and Deimos via a giant impact. Icarus 252, 334–338.

Citron, R. I., Zhong, S., 2012. Constraints on the formation of the Martian crustal dichotomy from remnant crustal magnetism. Physics of the Earth and Planetary Interiors 212-213, 55–63.

Clauser, C., Huenges, E., 1995. Thermal Conductivity of Rocks and Minerals. In: T. J. Ahrens (Ed.), Rock Physics and Phase Relations: A handbook of Physical Constants, AGU Ref. Shelf, vol. 3. AGU, Washington D.C., pp. 105–126.

Clifford, S. M., Parker, T. J., 2001. The Evolution of the Martian Hydrosphere: Implications for the Fate of a Primordial Ocean and the Current State of the Northern Plains. Icarus 154 (1), 40–79.

Collins, G. S., Elbeshausen, D., Davison, T. M., Robbins, S. J., Hynek, B. M., 2011. The size-frequency distribution of elliptical impact craters. Earth and Planetary Science Letters 310 (1-2), 1–8.

Collins, G. S., Melosh, H. J., Ivanov, B. a., 2004. Modeling damage and deformation in impact simulations. Meteoritics and Planetary Science 39 (2), 217–231.

Connerney, J. E., Acuna, M., Wasilewski, P. J., Ness, N. F., Reme, H., Mazelle, C., Vignes, D., Lin, R. P., Mitchell, D. L., Cloutier, P. A., 1999. Magnetic Lineations in the Ancient Crust of Mars. Science 284 (1999), 794–798.

Connerney, J. E. P., Acuña, M. H., Ness, N. F., Kletetschka, G., Mitchell, D. L., Lin, R. P., Reme, H., 2005. Tectonic implications of Mars crustal magnetism. Proceedings of the National Academy of Sciences of the United States of America 102, 14970–14975.

Costard, F., Séjourné, A., Kelfoun, K., Clifford, S., Lavigne, F., Di Pietro, I., Bouley, S., 2017. Modeling tsunami propagation and the emplacement of thumbprint terrain in an early Mars ocean. Journal of Geophysical Research: Planets 122 (3), 633–649.

Craddock, R. a., 2011. Are Phobos and Deimos the result of a giant impact? Icarus 211 (2), 1150–1161.

Crawford, D., 1999. Adaptive mesh refinement in CTH. Tech. rep., Sandia National Laboratories (SNL), Albuquerque, NM, and Livermore, CA.

Dannberg, J., Heister, T., 2016. Compressible magma/mantle dynamics: 3-D, adaptive simulations in ASPECT. Geophysical Journal International 207 (3), 1343–1366.

Daradich, A., Mitrovica, J. X., Matsuyama, I., Perron, J. T., Manga, M., Richards, M. A., 2008. Equilibrium rotational stability and figure of Mars. Icarus 194 (2), 463–475.

Davila, A. F., Fairén, A. G., Stokes, C. R., Platz, T., Rodriguez, A. P., Lacelle, D., Dohm, J., Pollard, W., 2013. Evidence for Hesperian glaciation along the Martian dichotomy boundary. Geology 41 (7), 755–758.

Davison, T. M., Collins, G. S., Elbeshausen, D., Wünnemann, K., Kearsley, A., 2011. Numerical modeling of oblique hypervelocity impacts on strong ductile targets. Meteoritics and Planetary Science 46 (10), 1510–1524.

Deschamps, F., Yao, C., Tackley, P. J., Sanchez-Valle, C., 2012. High Rayleigh number thermal convection in volumetrically heated spherical shells. Journal of Geophysical Research E: Planets 117 (9), 1–12.

Di Achille, G., Hynek, B. M., 2010. Ancient ocean on Mars supported by global distribution of deltas and valleys. Nature Geoscience 3 (7), 459–463.

Dietrich, W., Wicht, J., Hori, K., 2015. Effect of width, amplitude, and position of a core mantle boundary hot spot on core convection and dynamo action. Progress in Earth and Planetary Science 2 (1), 35.

Dohm, J. M., Baker, V. R., Boynton, W. V., Fairén, A. G., Ferris, J. C., Finch, M., Furfaro, R., Hare, T. M., Janes, D. M., Kargel, J. S., Karunatillake, S., Keller, J., Kerry, K., Kim, K. J., Komatsu, G., Mahaney, W. C., Schulze-Makuch, D., Marinangeli, L., Ori, G. G., Ruiz, J., Wheelock, S. J., 2009. GRS evidence and the possibility of paleooceans on Mars. Planetary and Space Science 57 (5-6), 664–684.

Dohm, J. M., Baker, V. R., Maruyama, S., Anderson, R. C., 2007. Traits and evolution of the Tharsis superplume, Mars. In: Superplumes: Beyond Plate Tectonics. Springer, Ch. 17, pp. 523–536.

Dreibus, G., Wanke, H., 1985. Mars, a volatile-rich planet. Meteorititcs 20, 367–381.

Edgett, K. S., Parker, T. J., 1997. Water on early Mars: Possible subaqueous sedimentary deposits covering ancient cratered terrain in western Arabia and Sinus Meridiani. Geophysical Research Letters 24 (22), 2897.

Elbeshausen, D., Melosh, J., 2018. A nonlinear and time-dependent visco-elasto-plastic rheology model for studying shock-physics phenomena. arXiv preprint arXiv:1805.06453.

Elbeshausen, D., Wünnemann, K., Collins, G. S., 2013. The transition from circular to elliptical impact craters. Journal of Geophysical Research E: Planets 118 (11), 2295–2309.

Elkins-Tanton, L. T., Parmentier, E. M., Hess, P. C., 2003. Magma ocean fractional crystallization and cumulate overturn in terrestrial planets: Implications for Mars. Meteoritics & Planetary Science 38 (12), 1753–1771.

Elkins-Tanton, L. T., Zaranek, S. E., Parmentier, E. M., Hess, P. C., 2005. Early magnetic field and magmatic activity on Mars from magma ocean cumulate overturn. Earth and Planetary Science Letters 236 (1-2), 1–12.

Emsenhuber, A., Jutzi, M., Benz, W., 2018. SPH calculations of Mars-scale collisions: The role of the equation of state, material rheologies, and numerical effects. Icarus 301, 247–257.

Erkeling, G., Hiesinger, H., Reiss, D., Hielscher, F., Ivanov, M., 2011. The stratigraphy of the Amenthes region, Mars: Time limits for the formation of fluvial, volcanic and tectonic landforms. Icarus 215 (1), 128–152.

Erkeling, G., Reiss, D., Hiesinger, H., Poulet, F., Carter, J., Ivanov, M., Hauber, E., Jaumann, R., 2012. Valleys, paleolakes and possible shorelines at the Libya Montes/Isidis boundary: Implications for the hydrologic evolution of Mars. Icarus 219 (1), 393–413.

Evans, A. J., Andrews-Hanna, J. C., Zuber, M. T., 2010. Geophysical limitations on the erosion history within Arabia Terra. Journal of Geophysical Research E: Planets 115 (5), 1–13.

Evans, A. J., Zuber, M. T., Weiss, B. P., Tikoo, S. M., 2014. A wet, heterogeneous lunar interior: Lower mantle and core dynamo evolution. Journal of Geophysical Research E: Planets 119 (5), 1061–1077.

Fairén, A. G., Dohm, J. M., Baker, V. R., de Pablo, M. A., Ruiz, J., Ferris, J. C., Anderson, R. C., 2003. Episodic flood inundations of the northern plains of Mars. Icarus 165 (1), 53–67.

Fairén, A. G., Ruiz, J., Anguita, F., 2002. An origin for the linear magnetic anomalies on mars through accretion of terranes: Implications for dynamo timing. Icarus 160 (1), 220–223.

Fawdon, P., Gupta, S., Davis, J. M., Warner, N. H., Adler, J. B., Balme, M. R., Bell, J. F., Grindrod, P. M., Sefton-Nash, E., 2018. The Hypanis Valles delta: The last highstand of a sea on early Mars? Earth and Planetary Science Letters 500, 225–241.

Fraeman, A. A., Korenaga, J., 2010. The influence of mantle melting on the evolution of Mars. Icarus 210 (1), 43–57.

Freed, A. M., Johnson, B. C., Blair, D. M., Melosh, H. J., Neumann, G. A., Phillips, R. J., Solomon, S. C., Wieczorek, M. A., Zuber, M. T., 2014. The formation of lunar mascon basins from impact to contemporary form. Journal of Geophysical Research: Planets 119 (11), 2378–2397.

Frey, H. V., 2006a. Impact constraints on, and a chronology for, major events in early Mars history. Journal of Geophysical Research E: Planets 111 (8), 1–11.

Frey, H. V., 2006b. Impact constraints on the age and origin of the lowlands of Mars. Geophysical Research Letters 33 (8), 2004–2007.

Genova, A., Goossens, S., Lemoine, F. G., Mazarico, E., Neumann, G. A., Smith, D. E., Zuber, M. T., 2016. Seasonal and static gravity field of mars from mgs, mars odyssey and mro radio science. Icarus 272, 228–245.

Ghods, A., Arkani-Hamed, J., 2011. Effects of the Borealis impact on the mantle dynamics of Mars. Physics of the Earth and Planetary Interiors 188 (1), 37–46.

Golabek, G. J., Emsenhuber, A., Jutzi, M., Asphaug, E. I., Gerya, T. V., 2018. Coupling SPH and thermochemical models of planets: Methodology and example of a Mars-sized body. Icarus 301, 235–246.

Golabek, G. J., Keller, T., Gerya, T. V., Zhu, G., Tackley, P. J., Connolly, J. a. D., 2011. Origin of the martian dichotomy and Tharsis from a giant impact causing massive magmatism. Icarus 215 (1), 346–357.

Goossens, S., Sabaka, T. J., Genova, A., Mazarico, E., Nicholas, J. B., Neumann, G. A., 2017. Evidence for a low bulk crustal density for Mars from gravity and topography. Geophysical Research Letters 44 (15), 7686–7694.

Grott, M., Baratoux, D., Hauber, E., Sautter, V., Mustard, J., Gasnault, O., Ruff, S. W., Karato, S. I., Debaille, V., Knapmeyer, M., Sohl, F., van Hoolst, T., Breuer, D., Morschhauser, A., Toplis, M. J., 2013. Long-term evolution of the martian crust-mantle system. Space Science Reviews 174, 49–111.

Grott, M., Breuer, D., 2009. Implications of large elastic thicknesses for the composition and current thermal state of Mars. Icarus 201 (2), 540–548.

Grott, M., Breuer, D., 2010. On the spatial variability of the Martian elastic lithosphere thickness: Evidence for mantle plumes? Journal of Geophysical Research 115 (E3), E03005.

Grott, M., Morschhauser, A., Breuer, D., Hauber, E., 2011. Volcanic outgassing of CO2 and H2O on Mars. Earth and Planetary Science Letters 308 (3-4), 391–400.

Gurnis, M., 1988. Large-scale mantle convection and the aggregation and dispersal of supercontinents. Nature 332 (6166), 695–699.

Halevy, I., Head, J. W., 2014. Episodic warming of early Mars by punctuated volcanism. Nature Geoscience 7 (12), 865–868.

Halevy, I., Schrag, D. P., 2009. Sulfur dioxide inhibits calcium carbonate precipitation: Implications for early Mars and Earth. Geophys. Res. Lett 36.

Halevy, I., Zuber, M. T., Schrag, D. P., 2007. A Sulfur Dioxide Climate Feedback on Early Mars. Science 318 (5858), 1903–1907.

Harada, Y., 2012. Long-term polar motion on a quasi-fluid planetary body with an elastic lithosphere: Semi-analytic solutions of the time-dependent equation. Icarus 220 (2), 449–465.

Harder, H., 2000. Mantle convection and the dynamic geoid of Mars. Geophysical Research Letters 27 (3), 301–304.

Harland, W. B., Armstrong, R. L., Cox, A. V., Craig, L. E., Smith, A. G., Smith, D. G., 1990. A geologic time scale 1989. Cambridge University Press.

Hartmann, W. K., 2005. Martian cratering 8: Isochron refinement and the chronology of Mars. Icarus 174 (2), 294–320.

Hartmann, W. K., Neukum, G., 2001. Cratering chronology and the evolution of Mars. In: Chronology and evolution of Mars. Springer, pp. 165–194.

Hauck, S. A., Phillips, R. J., 2002. Thermal and crustal evolution of Mars. Journal of Geophysical Research 107 (E7).

Head, J. W., Hiesinger, H., Ivanov, M. a., Kreslavsky, M. a., Pratt, S., Thomson, B. J., 1999. Possible ancient oceans on Mars: evidence from Mars Orbiter Laser Altimeter data. Science 286 (5447), 2134–2137.

Hofmeister, A. M., 1999. Mantle Values of Thermal Conductivity and the Geotherm from Phonon Lifetimes. Science 283, 1699–1706.

Hu, H., van der Wal, W., Vermeersen, L., 2017. A full-Maxwell approach for large angle polar wander of viscoelastic bodies. Journal of Geophysical Research: Planets accepted.

Hynek, B. M., Robbins, S. J., Šrámek, O., Zhong, S. J., 2011. Geological evidence for a migrating Tharsis plume on early Mars. Earth and Planetary Science Letters 310, 327–333.

Hyodo, R., Genda, H., Charnoz, S., Rosenblatt, P., 2017. On the Impact Origin of Phobos and Deimos I: Thermodynamic and Physical Aspects. The Astrophysical Journal 845.

Ivanov, B., Melosh, H., Pierazzo, E., 2010. Basin-forming impacts: Reconnaissance modeling. Special Paper of the Geological Society of America 465, 29–49.

Ivanov, M. A., Erkeling, G., Hiesinger, H., Bernhardt, H., Reiss, D., 2017. Topography of the Deuteronilus contact on Mars: Evidence for an ancient water/mud ocean and long-wavelength topographic readjustments. Planetary and Space Science 144, 49–70.

Jakosky, B., Brain, D., Chaffin, M., Curry, S., Deighan, J., Grebowsky, J., Halekas, J., Leblanc, F., Lillis, R., Luhmann, J., Andersson, L., Andre, N., Andrews, D., Baird, D., Baker, D., Bell, J., Benna, M., Bhattacharyya, D., Bougher, S., Bowers, C., Chamberlin,

P., Chaufray, J.-Y., Clarke, J., Collinson, G., Combi, M., Connerney, J., Connour, K., Correira, J., Crabb, K., Crary, F., Cravens, T., Crismani, M., Delory, G., Dewey, R., DiBraccio, G., Dong, C., Dong, Y., Dunn, P., Egan, H., Elrod, M., England, S., Eparvier, F., Ergun, R., Eriksson, A., Esman, T., Espley, J., Evans, S., Fallows, K., Fang, X., Fillingim, M., Flynn, C., Fogle, A., Fowler, C., Fox, J., Fujimoto, M., Garnier, P., Girazian, Z., Groeller, H., Gruesbeck, J., Hamil, O., Hanley, K., Hara, T., Harada, Y., Hermann, J., Holmberg, M., Holsclaw, G., Houston, S., Inui, S., Jain, S., Jolitz, R., Kotova, A., Kuroda, T., Larson, D., Lee, Y., Lee, C., Lefevre, F., Lentz, C., Lo, D., Lugo, R., Ma, Y.-J., Mahaffy, P., Marquette, M., Matsumoto, Y., Mayyasi, M., Mazelle, C., McClintock, W., McFadden, J., Medvedev, A., Mendillo, M., Meziane, K., Milby, Z., Mitchell, D., Modolo, R., Montmessin, F., Nagy, A., Nakagawa, H., Narvaez, C., Olsen, K., Pawlowski, D., Peterson, W., Rahmati, A., Roeten, K., Romanelli, N., Ruhunusiri, S., Russell, C., Sakai, S., Schneider, N., Seki, K., Sharrar, R., Shaver, S., Siskind, D., Slipski, M., Soobiah, Y., Steckiewicz, M., Stevens, M., Stewart, I., Stiepen, A., Stone, S., Tenishev, V., Terada, N., Terada, K., Thiemann, E., Tolson, R., Toth, G., Trovato, J., Vogt, M., Weber, T., Withers, P., Xu, S., Yelle, R., Yiğit, E., Zurek, R., 2018. Loss of the Martian atmosphere to space: Present-day loss rates determined from MAVEN observations and integrated loss through time. Icarus 315, 146–157.

Johnson, B. C., Blair, D. M., Collins, G. S., Melosh, H. J., Freed, A. M., Taylor, G. J., Head, J. W., Wieczorek, M. A., Andrews-Hanna, J. C., Nimmo, F., Keane, J. T., Miljković, K., Soderblom, J. M., Zuber, M. T., 2016. Formation of the Orientale lunar multiring basin. Science 354 (6311), 441–444.

Johnson, C. L., Solomon, S. C., Head III, J. W., Phillips, R. J., Smith, D. E., Zuber, M. T., 2000. Lithospheric loading by the northern polar cap on Mars. Icarus 144 (2), 313–328.

Karato, S., Wu, P., 1993. Rheology of the upper mantle: a synthesis. Science 260 (5109), 771–778.

Karato, S.-I., Jung, H., 2003. Effects of pressure on high-temperature dislocation creep in olivine. Philosophical Magazine 83 (3), 401–414.

Karimi, S., Dombard, A. J., Buczkowski, D. L., Robbins, S. J., Williams, R. M., 2016. Using the viscoelastic relaxation of large impact craters to study the thermal history of Mars. Icarus 272, 102–113.

Karunatillake, S., Squyres, S. W., Taylor, G. J., Keller, J. M., Gasnault, O., Evans, L. G., Reedy, R. C., Starr, R. D., Boynton, W. V., Janes, D. M., Kerry, K. E., Dohm, J. M., Sprague, A. L., Hahn, B. C., Hamara, D., 2007. Composition of northern low-albedo regions of Mars: Insights from the Mars Odyssey Gamma Ray Spectrometer. Journal of Geophysical Research E: Planets 112 (3), 1–16.

Katz, R. F., Spiegelman, M., Langmuir, C. H., 2003. A new parameterization of hydrous mantle melting. Geochemistry, Geophysics, Geosystems 4 (9), 1–19.

Ke, Y., Solomatov, V. S., 2006. Early transient superplumes and the origin of the Martian crustal dichotomy. Journal of Geophysical Research E: Planets 111 (10), 1–12.

Keane, J. T., Matsuyama, I., 2014. Evidence for lunar true polar wander and a past low-eccentricity, synchronous lunar orbit. Geophysical Research Letters 41 (19), 6610–6619.

Keller, T., Tackley, P. J., 2009. Towards self-consistent modeling of the martian dichotomy: The influence of one-ridge convection on crustal thickness distribution. Icarus 202 (2), 429–443.

Kiefer, W. S., 2005. Buried mass anomalies along the hemispheric dichotomy in eastern Mars: Implications for the origin and evolution of the dichotomy. Geophysical Research Letters 32 (22), 1–4.

Kiefer, W. S., Filiberto, J., Sandu, C., Li, Q., 2015. The effects of mantle composition on the peridotite solidus: Implications for the magmatic history of Mars. Geochimica et Cosmochimica Acta 162, 247–258.

Kiefer, W. S., Li, Q., 2009. Mantle convection controls the observed lateral variations in lithospheric thickness on present-day Mars. Geophysical Research Letters 36 (18), L18203.

King, S. D., Redmond, H. L., 2005. The Crustal Dichotomy and Edge Driven Convection: A Mechanism for Tharsis Rise Volcanism? Lunar and Planetary Institute Science Conference Abstracts 36 (1), 1–2.

Kite, E. S., 2019. Geologic constraints on early Mars climate. Space Science Reviews 215 (1), 10.

Kite, E. S., Gao, P., Goldblatt, C., Mischna, M. A., Mayer, D. P., Yung, Y. L., 2017. Methane bursts as a trigger for intermittent lake-forming climates on post-Noachian Mars. Nature Geoscience 10 (10), 737–740.

Kite, E. S., Matsuyama, I., Manga, M., Perron, J. T., Mitrovica, J. X., 2009. True Polar Wander driven by late-stage volcanism and the distribution of paleopolar deposits on Mars. Earth and Planetary Science Letters 280 (1-4), 254–267.

Kite, E. S., Mayer, D. P., Wilson, S. A., Davis, J. M., Lucas, A. S., de Quay, G. S., 2019. Persistence of intense, climate-driven runoff late in mars history. Science advances 5 (3), eaav7710.

Kobayashi, D., Sprenke, K. F., 2010. Lithospheric drift on early Mars: evidence in the magnetic field. Icarus 210 (1), 37–42.

Leinhardt, Z. M., Stewart, S. T., 2009. Full numerical simulations of catastrophic small body collisions. Icarus 199 (2), 542–559.

Lenardic, A., Moresi, L. N., Jellinek, M. A., Manga, M., 2005. Continental insulation, mantle cooling, and the surface area of oceans and continents. Earth and Planetary Science Letters 234 (3-4), 317–333.

Lenardic, A., Richards, M. A., Busse, F. H., 2006. Depth-dependent rheology and the horizontal length scale of mantle convection. Journal of Geophysical Research 111 (B7), B07404.

Li, M., Black, B., Zhong, S., Manga, M., Rudolph, M. L., Olson, P., 2016. Quantifying melt production and degassing rate at mid-ocean ridges from global mantle convection models with plate motion history. Geochemistry, Geophysics, Geosystems 17 (7), 2884–2904.

Lillis, R. J., Robbins, S., Manga, M., Halekas, J. S., Frey, H. V., 2013a. Time history of the Martian dynamo from crater magnetic field analysis. Journal of Geophysical Research E: Planets 118 (7), 1488–1511.

Lillis, R. J., Stewart, S. T., Manga, M., 2013b. Demagnetization by basin-forming impacts on early Mars: Contributions from shock, heat, and excavation. Journal of Geophysical Research E: Planets 118 (5), 1045–1062.

Lodders, K., Fegley, B., 1997. An Oxygen Isotope Model for the Composition of Mars. Icarus 126, 373–394.

Lowman, J. P., Jarvis, G. T., 1995. Mantle convection models of continental collision and breakup incorporating finite thickness plates. Physics of the Earth and Planetary Interiors 88 (1), 53–68.

Malin, M. C., Edgett, K. S., 1999. Oceans or seas in the Martian northern lowlands: High resolution imaging tests of proposed coastlines. Geophysical Research Letters 26 (19), 3049–3052.

Marinova, M. M., Aharonson, O., Asphaug, E., 2008. Mega-impact formation of the Mars hemispheric dichotomy. Nature 453 (7199), 1216–1219.

Marinova, M. M., Aharonson, O., Asphaug, E., 2011. Geophysical consequences of planetary-scale impacts into a Mars-like planet. Icarus 211 (2), 960–985.

Matsuyama, I., Manga, M., 2010. Mars without the equilibrium rotational figure, Tharsis, and the remnant rotational figure. Journal of Geophysical Research E: Planets 115 (12), 1–14.

McDonough, W. F., Sun, S.-s., 1995. The composition of the Earth. Chemical Geology 120, 223–253.

McGlaun, J. M., Thompson, S. L., Elrick, M. G., 1990. CTH: A three-dimensional shock wave physics code. International Journal of Impact Engineering 10 (1-4), 351–360.

McGowan, E. M., McGill, G. E., 2006. Anomalous tilt of Isidis Planitia, Mars. Geophysical Research Letters 33 (8).

Mei, S., Kohlstedt, D., 2000. Influence of water on plastic deformation of olivine aggregates: 1. diffusion creep regime. Journal of Geophysical Research: Solid Earth 105 (B9), 21457–21469.

Melosh, H. J., 2007. A hydrocode equation of state for SiO2. Meteoritics & Planetary Science 42 (12), 2079–2098.

Mohit, P. S., Phillips, R. J., 2007. Viscous relaxation on early Mars: A study of ancient impact basins. Geophysical Research Letters 34 (21), L21204.

Monteux, J., Amit, H., Choblet, G., Langlais, B., Tobie, G., 2015. Giant impacts, heterogeneous mantle heating and a past hemispheric dynamo on Mars. Physics of the Earth and Planetary Interiors 240, 114–124.

Moore, K. M., Chan, N. H., Daradich, A., Mitrovica, J. X., 2017. Time-dependent rotational stability of dynamic planets with viscoelastic lithospheres. Icarus 289, 34–41.

Morschhauser, a., Grott, M., Breuer, D., 2011. Crustal recycling, mantle dehydration, and the thermal evolution of Mars. Icarus 212 (2), 541–558.

Moser, D. E., Arcuri, G., Reinhard, D., White, L. F., Darling, J., Barker, I. R., Larson, D., Irving, A., McCubbin, F., Tait, K., et al., 2019. Decline of giant impacts on mars by 4.48 billion years ago and an early opportunity for habitability. Nature Geoscience.

Mustard, J. F., 2019. Sequestration of Volatiles in the Martian Crust Through Hydrated Minerals: A Significant Planetary Reservoir of Water. Volatiles in the Martian Crust, 247–263.

Neumann, G. A., Zuber, M. T., Wieczorek, M. A., McGovern, P. J., Lemoine, F. G., Smith, D. E., 2004. Crustal structure of Mars from gravity and topography. Journal of Geophysical Research E: Planets 109 (8), 1–18.

Nimmo, F., 2000. Dike intrusion as a possible cause of linear martian magnetic anomalies. Geology 28 (5), 391–394.

Nimmo, F., 2005. Tectonic consequences of Martian dichotomy modification by lower-crustal flow and erosion. Geology 33, 533–536.

Nimmo, F., Hart, S. D., Korycansky, D. G., Agnor, C. B., 2008. Implications of an impact origin for the martian hemispheric dichotomy. Nature 453 (7199), 1220–1223.

Pan, L., Ehlmann, B. L., Carter, J., Ernst, C. M., 2017. The stratigraphy and history of Mars' northern lowlands through mineralogy of impact craters: A comprehensive survey. Journal of Geophysical Research: Planets 122 (9), 1824–1854.

Parker, T. J., Gorsline, D. S., Saunders, R. S., Pieri, D. C., Schneeberger, D. M., 1993. Coastal geomorphology of the Martian northern plains. Journal of Geophysical Research 98 (93), 11061.

Parker, T. J., Stephen Saunders, R., Schneeberger, D. M., 1989. Transitional morphology in West Deuteronilus Mensae, Mars: Implications for modification of the lowland/upland boundary. Icarus 82 (1), 111–145.

Perron, J. T., Mitrovica, J. X., Manga, M., Matsuyama, I., Richards, M. A., 2007. Evidence for an ancient martian ocean in the topography of deformed shorelines. Nature 447 (7146), 840–843.

Phillips, R. J., Zuber, M. T., Smrekar, S. E., Mellon, M. T., Head, J. W., Tanaka, K. L., Putzig, N. E., Milkovich, S. M., Campbell, B. A., Plaut, J. J., et al., 2008. Mars north polar deposits: Stratigraphy, age, and geodynamical response. Science 320 (5880), 1182–1185.

Phillips, R. J., Zuber, M. T., Solomon, S. C., Golombek, M. P., Jakosky, B. M., Banerdt, W. B., Smith, D. E., Williams, R. M., Hynek, B. M., Aharonson, O., Hauck, S. A., 2001. Ancient geodynamics and global-scale hydrology on Mars. Science 291 (5513), 2587–2591.

Pierazzo, E., Artemieva, N., Ivanov, B., 2005. Starting conditions for hydrothermal systems underneath Martian craters: Hydrocode modeling. In: Special Paper 384: Large Meteorite Impacts III. pp. 443–457.

Platz, T., Michael, G., 2011. Eruption history of the Elysium volcanic province, Mars. Earth and Planetary Science Letters 312 (1-2), 140–151.

Plesa, A. C., Breuer, D., 2014. Partial melting in one-plate planets: Implications for thermochemical and atmospheric evolution. Planetary and Space Science 98, 55–65.

Plesa, A.-C., Grott, M., Tosi, N., Breuer, D., Spohn, T., Wieczorek, M. A., 2016. How large are present-day heat flux variations across the surface of Mars? Journal of Geophysical Research: Planets 121 (12), 2386–2403.

Plesa, A.-C., Padovan, S., Tosi, N., Breuer, D., Grott, M., Wieczorek, M., Spohn, T., Smrekar, S., Banerdt, W., 2018. The thermal state and interior structure of Mars. Geophysical Research Letters 45 (22), 12–198.

Ramirez, R. M., Craddock, R. A., 2018. The geological and climatological case for a warmer and wetter early Mars. Nature Geoscience 11 (4), 230.

Raterron, P., Holyoke, C., Tokle, L., Hilairet, N., Merkel, S., Hirth, G., Weidner, D., 2017. Effect of Iron Content on Olivine Viscosity and Implications for the Martian Mantle. In: Lunar and Planetary Science XLVIII. p. 1553.

Redmond, H. L., King, S. D., 2004. A numerical study of a mantle plume beneath the Tharsis Rise: Reconciling dynamic uplift and lithospheric support models. Journal of Geophysical Research 109 (E9), E09008.

Reese, C. C., Orth, C. P., Solomatov, V. S., 2010. Impact origin for the Martian crustal dichotomy: Half emptied or half filled? Journal of Geophysical Research E: Planets 115 (5), E05004.

Reese, C. C., Orth, C. P., Solomatov, V. S., 2011. Impact megadomes and the origin of the martian crustal dichotomy. Icarus 213 (2), 433–442.

Ritzer, J. A., Hauck, S. A., 2009. Lithospheric structure and tectonics at Isidis Planitia, Mars. Icarus 201, 528–539.

Rivera-Hernández, F., Palucis, M. C., 2019. Do deltas along the crustal dichotomy boundary of Mars in the Gale crater region record a northern ocean? Geophysical Research Letters, 2019GL083046.

Robbins, S. J., Hynek, B. M., Lillis, R. J., Bottke, W. F., 2013. Large impact crater histories of Mars: The effect of different model crater age techniques. Icarus 225 (1), 173–184.

Roberts, J., Arkani-Hamed, J., 2017. Effects of basin-forming impacts on the thermal evolution and magnetic field of Mars. Earth and Planetary Science Letters 478, 192–202.

Roberts, J. H., Arkani-Hamed, J., 2012. Impact-induced mantle dynamics on Mars. Icarus 218 (1), 278–289.

Roberts, J. H., Lillis, R. J., Manga, M., 2009. Giant impacts on early mars and the cessation of the martian dynamo. Journal of Geophysical Research E: Planets 114 (4), E04009.

Roberts, J. H., Zhong, S., 2004. Plume-induced topography and geoid anomalies and their implications for the Tharsis rise on Mars. Journal of Geophysical Research 109 (E3), E03009.

Roberts, J. H., Zhong, S., 2006. Degree-1 convection in the Martian mantle and the origin of the hemispheric dichotomy. Journal of Geophysical Research E: Planets 111 (6).

Roberts, J. H., Zhong, S., 2007. The cause for the north-south orientation of the crustal dichotomy and the equatorial location of Tharsis on Mars. Icarus 190 (1), 24–31.

Rodriguez, J. A. P., Fairén, A. G., Tanaka, K. L., Zarroca, M., Linares, R., Platz, T., Komatsu, G., Miyamoto, H., Kargel, J. S., Yan, J., Gulick, V., Higuchi, K., Baker, V. R., Glines, N., 2016. Tsunami waves extensively resurfaced the shorelines of an early Martian ocean. Scientific Reports 6 (1), 25106.

Rosenblatt, P., Charnoz, S., Dunseath, K. M., Terao-Dunseath, M., Trinh, A., Hyodo, R., Genda, H., Toupin, S., 2016. Accretion of Phobos and Deimos in an extended debris disc stirred by transient moons. Nature Geoscience 9 (August), 4–8.

Rouby, H., Greff-Lefftz, M., Besse, J., 2008. Rotational bulge and one plume convection pattern: Influence on Martian true polar wander. Earth and Planetary Science Letters 272 (1-2), 212–220.

Rudnick, R. L., 1995. Making continental crust. Nature 378 (6557), 571–578.

Ruedas, T., Breuer, D., 2017. On the relative importance of thermal and chemical buoyancy in regular and impact-induced melting in a Mars-like planet. Journal of Geophysical Research: Planets 122 (7), 1554–1579.

Ruedas, T., Tackley, P. J., Solomon, S. C., 2013a. Thermal and compositional evolution of the martian mantle: Effects of phase transitions and melting. Physics of the Earth and Planetary Interiors 216, 32–58.

Ruedas, T., Tackley, P. J., Solomon, S. C., 2013b. Thermal and compositional evolution of the martian mantle: Effects of water. Physics of the Earth and Planetary Interiors 220, 50–72.

Ruiz, J., Fairén, A. G., Dohm, J. M., Tejero, R., 2004. Thermal isostasy and deformation of possible paleoshorelines on Mars. Planetary and Space Science 52 (14), 1297–1301.

Ruiz, J., Tejero, R., Gómez-Ortiz, D., 2006. Paleoshorelines and the Evolution of the Lithosphere of Mars. In: Maravell, N. S. (Ed.), Space Science: New Research. Nova Science Publishers, Ch. 5, pp. 141–164.

Samuel, H., Lognonné, P., Panning, M., Lainey, V., 2019. The rheology and thermal history of mars revealed by the orbital evolution of phobos. Nature 569 (7757), 523.

Sandu, C., Kiefer, W. S., 2012. Degassing history of Mars and the lifespan of its magnetic dynamo. Geophysical Research Letters 39 (3), L03201.

Scheinberg, A., Elkins-Tanton, L. T., Zhong, S. J., 2014. Timescale and morphology of Martian mantle overturn immediately following magma ocean solidification. Journal of Geophysical Research: Planets 119 (3), 454–467.

Schmitt, R., Brundage, A., Crawford, D., Harstad, E., Ruggirello, K., Schumacher, S., Simmons, J., 2015. CTH user's manual and input instructions (version 11.1). Sandia National Laboratories.

Schools, J. W., Montési, L. G., 2018. The Generation of Barriers to Melt Ascent in the Martian Lithosphere. Journal of Geophysical Research: Planets 123, 47–66.

Schultz, P. H., Crawford, D. A., 2016. Origin and implications of non-radial Imbrium Sculpture on the Moon. Nature 535 (7612), 391–394.

Searls, M. L., Banerdt, W. B., Phillips, R. J., 2006. Utopia and Hellas basins, Mars: Twins separated at birth. Journal of Geophysical Research E: Planets 111 (8), E08005.

Sekhar, P., King, S. D., 2014. 3D spherical models of Martian mantle convection constrained by melting history. Earth and Planetary Science Letters 388, 27–37.

Senft, L. E., Stewart, S. T., 2007. Modeling impact cratering in layered surfaces. Journal of Geophysical Research E: Planets 112, 1–18.

Senft, L. E., Stewart, S. T., 2008. Impact crater formation in icy layered terrains on Mars. Meteoritics & Planetary Science 43 (12), 1993–2013.

Shaposhnikov, D. S., Medvedev, A. S., Rodin, A. V., Hartogh, P., 2019. Seasonal water "pump" in the atmosphere of mars: Vertical transport to the thermosphere. Geophysical Research Letters 46 (8), 4161–4169.

Sholes, S. F., Montgomery, D. R., Catling, D. C., 2019. Quantitative high-resolution reexamination of a hypothesized ocean shoreline in cydonia mensae on mars. Journal of Geophysical Research: Planets 124 (2), 316–336.

Sjogren, W. L., 1979. Mars gravity: high-resolution results from viking orbiter 2. Science 203 (4384), 1006–1010.

Smith, D., Zuber, M., Neumann, G., Guinness, E., Slaveny, S., 2003. Mars Global Surveyor Laser Altimeter Mission Experiment Gridded Data Record, MGS-M-MOLA-5-MEGDR-L3-V1.0, NASA Planetary Data System.

Smith, D. E., Zuber, M. T., Solomon, S. C., Phillips, R. J., Head, J. W., Garvin, J. B., Banerdt, W. B., Muhleman, D. O., Pettengill, G. H., Neumann, G. a., Lemoine, F. G., Abshire, J. B., Aharonson, O., Brown, C. D., Hauck, S. a., Ivanov, a. B., McGovern, P. J., Zwally, H. J., Duxbury, T. C., 1999. The global topography of Mars and implications for surface evolution. Science 284, 1495–1503.

Solomon, S. C., Aharonson, O., Aurnou, J. M., Banerdt, W. B., Carr, M. H., Dombard, A. J., Frey, H. V., Golombek, M. P., Hauck, S. a., Head, J. W., Jakosky, B. M., Johnson, C. L., McGovern, P. J., Neumann, G. a., Phillips, R. J., Smith, D. E., Zuber, M. T., 2005. New perspectives on ancient Mars. Science 307, 1214–1220.

Spada, G., 2008. ALMA, a Fortran program for computing the viscoelastic Love numbers of a spherically symmetric planet. Computers and Geosciences 34 (6), 667–687.

Sprenke, K. F., Baker, L. L., 2000. Magnetization, paleomagnetic poles, and polar wander on Mars. Icarus 147 (1), 26–34.

Šrámek, O., Zhong, S., 2010. Long-wavelength stagnant lid convection with hemispheric variation in lithospheric thickness: Link between Martian crustal dichotomy and Tharsis? Journal of Geophysical Research E: Planets 115, 1–20.

Šrámek, O., Zhong, S., 2012. Martian crustal dichotomy and Tharsis formation by partial melting coupled to early plume migration. Journal of Geophysical Research E: Planets 117 (1), 1–14.

Stanley, S., Elkins-Tanton, L., Zuber, M. T., Parmentier, E. M., 2008. Mars' Paleomagnetic Field as the Result of a Single-Hemisphere Dynamo. Science 321 (5897).

Tan, E., Choi, E., Thoutireddy, P., Gurnis, M., Aivazis, M., 2006. GeoFramework: Coupling multiple models of mantle convection within a computational framework. Geochemistry, Geophysics, Geosystems 7 (6).

Tanaka, K. L., Robbins, S. J., Fortezzo, C. M., Skinner, J. A., Hare, T. M., 2014. The digital global geologic map of Mars: Chronostratigraphic ages, topographic and crater morphologic characteristics, and updated resurfacing history. Planetary and Space Science 95, 11–24.

Taylor, G. J., Boynton, W. V., Brückner, J., Wänke, H., Dreibus, G., Kerry, K. E., Keller, J. M., Reedy, R. C., Evans, L. G., Starr, R. D., Squyres, S. W., Karunatillake, S., Gasnault, O., Maurice, S., D'Uston, C., Englert, P., Dohm, J. M., Baker, V., Hamara, D., Janes, D. M., Sprague, A. L., Kim, K. J., Drake, D., 2006. Bulk composition and early differentiation of Mars. Journal of Geophysical Research E: Planets 112 (3), E03S10.

Thiriet, M., Michaut, C., Breuer, D., Plesa, A.-C., 2018. Hemispheric dichotomy in lithosphere thickness on Mars caused by differences in crustal structure and composition. Journal of Geophysical Research: Planets 123 (4), 823–848.

Thompson, S. L., Lauson, H. S., 1972. Improvements in the CHART D radiation-hydrodynamic code III: revised analytic equations of state. Sandia National Laboratory Report SC-RR-71 0, 113p.

Tian, F., Claire, M. W., Haqq-Misra, J. D., Smith, M., Crisp, D. C., Catling, D., Zahnle, K., Kasting, J. F., 2010. Photochemical and climate consequences of sulfur outgassing on early Mars. Earth and Planetary Science Letters 295 (3-4), 412–418.

Turcotte, D., Willemann, R., Haxby, W., Norberry, J., 1981. Role of membrane stresses in the support of planetary topography. Journal of Geophysical Research: Solid Earth 86 (B5), 3951–3959.

van Thienen, P., Rivoldini, A., van Hoolst, T., Lognonné, P., 2006. A top-down origin for martian mantle plumes. Icarus 185 (1), 197–210.

Wade, J., Dyck, B., Palin, R. M., Moore, J. D. P., Smye, A. J., 2017. The divergent fates of primitive hydrospheric water on Earth and Mars. Nature 552 (7685), 391–394.

Wanke, H., Dreibus, G., 1994. Chemistry and Accretion History of Mars. Philosophical Transactions of the Royal Society of London. Series A: Physical and Engineering Sciences 349 (1690), 285–293.

Watters, T. R., McGovern, P. J., Irwin III, R. P., 2007. Hemispheres Apart: The Crustal Dichotomy on Mars. Annual Review of Earth and Planetary Sciences 35 (1), 621–652.

Weiss, D. K., Head, J. W., 2017. Evidence for stabilization of the ice-cemented cryosphere in earlier martian history: Implications for the current abundance of groundwater at depth on Mars. Icarus 288, 120–147.

Weller, M. B., Lenardic, A., Moore, W. B., 2016. Scaling relationships and physics for mixed heating convection in planetary interiors: Isoviscous spherical shells. Journal of Geophysical Research: Solid Earth 121 (10), 7598–7617.

Wenzel, M. J., Manga, M., Jellinek, A. M., 2004. Tharsis as a consequence of Mars' dichotomy and layered mantle. Geophysical Research Letters 31 (4), L04702.

Werner, S. C., 2009. The global martian volcanic evolutionary history. Icarus 201 (1), 44–68.

Werner, S. C., Tanaka, K. L., 2011. Redefinition of the crater-density and absolute-age boundaries for the chronostratigraphic system of Mars. Icarus 215 (2), 603–607.

Whaler, K., Purucker, M., 2005. A spatially continuous magnetization model for mars. Journal of Geophysical Research: Planets 110 (E9).

Wieczorek, M. A., 2015. Gravity and Topography of the Terrestrial Planets. In: Treatise on Geophysics. Vol. 10. pp. 153–193.

Wieczorek, M. A., Zuber, M. T., 2004. Thickness of the Martian crust: Improved constraints from geoid-to-topography ratios. Journal of Geophysical Research 109 (E1), E01009.

Wilhelms, D., Squyres, S., 1984. The martion hemispheric dichotomy may be due to a giant impact. Nature 309, 138–140.

Willemann, R. J., 1984. Reorientation of planets with elastic lithospheres. Icarus 60 (3), 701–709.

Wordsworth, R., 2016. The Climate of Early Mars. Annual Review of Earth and Planetary Sciences 44, 381–408.

Wordsworth, R., Ehlmann, B., Forget, F., Haberle, R., Head, J., Kerber, L., 2018. Healthy debate on early mars. Nature Geoscience 11 (12), 888.

Wordsworth, R., Kalugina, Y., Lokshtanov, S., Vigasin, A., Ehlmann, B., Head, J., Sanders, C., Wang, H., 2017. Transient reducing greenhouse warming on early Mars. Geophysical Research Letters 44 (2), 665–671.

Zhao, Y. H., Zimmerman, M. E., Kohlstedt, D. L., 2009. Effect of iron content on the creep behavior of olivine: 1. Anhydrous conditions. Earth and Planetary Science Letters 287 (1-2), 229–240.

Zhong, S., 2009. Migration of Tharsis volcanism on Mars caused by differential rotation of the lithosphere. Nature Geoscience 2 (1), 19–23.

Zhong, S., Zuber, M. T., 2001. Degree-1 mantle convection and the crustal dichotomy on Mars. Earth and Planetary Science Letters 189, 75–84.

Zhong, S., Zuber, M. T., Moresi, L., Gurnis, M., 2000. Role of temperature-dependent viscosity and surface plates in spherical shell models of mantle convection. Journal of Geophysical Research: Solid Earth 105 (B5), 11063–11082.

Zuber, M., 2008. Mars reconnaissance orbiter derived gravity data: Nasa planetary data system. Tech. rep., MRO-M-RSS-5-SDP-V1. 0.

Zuber, M. T., 2001. The crust and mantle of Mars. Nature 412 (6843), 220–227.

Zuber, M. T., Solomon, S. C., Phillips, R. J., Smith, D. E., Tyler, G. L., Aharonson, O., Balmino, G., Banerdt, W. B., Head, J. W., Johnson, C. L., Lemoine, F. G., McGovern, P. J., Neumann, G. A., Rowlands, D. D., Zhong, S., 2000. Internal Structure and Early Thermal Evolution of Mars from Mars Global Surveyor Topography and Gravity. Science 287 (5459), 1788–1793.